Contents

List of Figures

List of Tables

Chapter 1

Introduction

High energy physics can be described by the study of the fundamental particles and the nature of interactions among them. The Standard Model is the currently best understanding of laws dealing with goals of high energy physics. In the Standard Model, the matter is made of six types of quarks and six leptons, and the fundamental interaction forces, the strong, the electromagnetic, and the weak can be explained by exchange of gauage bosons.

Although there are increasingly more experimental results on hadronic decays of charmed baryons, very little is known experimentally about their semileptonic decays. The semileptonic decays should proceed via a spectator process therefore semileptonic rates of different charmed baryons comparable with those of charmed mesons. The inclusive semileptonic partial widths of the D^0 and D^+ were observed to be the same. It would be interesting to study whether this is true for the charmed baryons. This would not be true if interference effects are important for one charmed baryon and not for another. The semileptonic branching ratios for the shorter lived charmed baryons should be smaller because the hadronic decay rates are enhanced by the large W-exchange processes as evidenced by their short lifetimes.

Compared to hadronic decays, the reconstruction of semileptonic decays is complicated by the fact that the neutrino is not observed so that a fully reconstructed mass plot can not be made. This means that a through understanding of the background is vital in any analysis of semileptonic decays. The D^+ has the advantage that it has a relatively long lifetime and in particular the mode $D^+ \longrightarrow K^{*0}l^+\nu$ proceeds via a resonance which can help to reduce background. The D^0 can be tagged by the $D^{*+} \longrightarrow D^0\pi^+$ decay. The reconstruction of semileptonic decay modes of charmed baryons is much harder not only the production rate is smaller than for charmed mesons but also their short lifetimes.

In the Fermilab E687 experiment, charmed particles are produced by high energy photon-nucleon collisions via the photon-gluon fusion process which can be described by the perturbative QCD to the next-to-leading order in α_s.

This dissertation has been performed as a part of E687 collaboration using data taken by the Fermilab photoproduction experiment E687, which used the highest photon beam energy in the world. This study reports on the analysis to try to reconstruct both the electron and muon modes of the Ξ_c^0 semileptonic decays.

In chapter 2, the basic features of charmed hadrons with the emphasis on the charmed baryons will be discussed. In Chapter 3, we will explain how we generated the photon beam and the experimental apparatus used in the E687 experiment, and also data acquisition used in the run. The methods of data reconstruction and the Monte Carlo simulation will be described in Chapter 5. The branching ratio measurements of the Ξ_c^0 semileptonic decays will be described in Chapter 6. In chapter 7, we will discuss possible systematic biases in the branching ratio measurement. The results and conclusion remarks will follow in Chapter 8.

Chapter 2

Charmed Hadrons

2.1 Overviews

It is accepted that the matter is built from two types of fundamental fermions, leptons and quarks. Leptons carry integral electric charges, 0 or ± 1, and they are grouped into three families based on the conserved quantum number. Neutral leptons are called neutrinos and have very small mass or zero rest mass. Quarks carry the fractional electric charges of $\frac{1}{3}$ or $\frac{2}{3}$ of the electric charge, and they are also grouped into three generations. Leptons exist as free particles whereas quarks only exist as constituents of hadrons.

The first existence of three quark flavors(u, d, and s) was proposed in 1964 by Gell-Mann [1] and Zweig [2], independently. The existence of a fourth (charm) quark was first suggested by Bjorken and Glashow [3] in 1964 to make the situation between quarks and leptons symmetrical. The strangeness-changing neutral weak currents(Z^0) incorporating the c(charm) quark was explained with the GIM(Glashow, Illiopoulos and Maiani) model [4] in 1970. In 1974, Gaillard, Lee and Rosner [5] developed the SU(4) spectroscopy and decay properties of hadrons containing the charm quark.

Table 2.1: Quark and Lepton Properties.

Quarks		Leptons	
Flavor	Charge	Flavor	Charge
u c t	+2/3	ν_e ν_μ ν_τ	0
d s b	-1/3	e^- μ^- τ^-	-1

The existence of the charm quark was provided by the discovery [6, 7] in November 1974 of the J/ψ as a narrow resonance of 3.1 GeV/c^2. The J/ψ was interpreted as a bound state of the charm and anti-charm($c\bar{c}$) pair. Subsequently to the discovery of the J/ψ, the open charm particles, such as D^0, D^+, and Λ_c^+ were experimentally found and the existence of charm quark was confirmed.

The discovery in 1977 [8] of the Υ as a $b\bar{b}$ bound state was the first indication of the existence of a fifth quark, the b(beauty or bottom) quark with a mass $m_b \approx$ 5 GeV/c^2. Recently the discovery of a sixth quark, the t(top) quark with a mass $m_t \approx 180$ GeV/c^2 was reported by both CDF and D0 collaborations at Fermilab [9, 10].

The total of all six flavor quarks are discovered. Only two types of quark combinations, meson and baryon are made in the quark model. A meson consists of a quark and an anti-quark and a baryon of three quarks.

The properties of leptons and quarks are summarized in Table 2.1.

2.2 Photoproduction of Charmed Hadrons

The charm quark can be produced by several types of interactions, high energy e^+e^-, photon-hadron, lepton-hadron, or hadron-hadron. The e^+e^- interaction have proven to be a reliable and clean way of producing charmed particles, but the absolute production rates are a few orders of magnitude smaller compare to photoproduction due to much lower luminosity. The photoproduced charm cross section is roughly 1% of the total photon hadronic cross section, which is about 5 times higher than in charm hadroproduction. Thereafter we choose a photon beam rather than a hadron beam mainly to suppress background.

The main drawback of a photon beam is the larger e^+e^- production rate relative to the hadronic interaction rate. For a beryllium target the e^+e^- rate is 500 times larger than the total hadronic cross section. This means that the experiment must resort to low Z target material. Although this may appear to be a large background, those unwanted events can be rejected by using a dedicated trigger. Another disadvantage of a photon beam experiment is the beam flux limitation and the difficulty in collimating the beam.

The possibility of the charm photoproduction was first suggested by Carlson [11] and further developed by Gaillard[5] based on the vector meson dominance model [12] and the naive quark model. In the late 1970's, the perturbative QCD approach to charm photoproduction was made. The charm photoproduction is well described by the Photon-Gluon Fusion(PGF) [13] process. The PGF model is based on the perturbative QCD process in the lowest order. Theoretical calculations are available for leading order and the next-leading-order process, along with contributions where the photon dissociates into hadronic components before interacting. The two lowest order diagrams are shown in Figure 2.1. In this model, a $c\bar{c}$ pair is produced from the interaction of a photon with a gluon from the target nucleon.

The PGF model predicts a total charm cross section which is gradually rising at high energies. The cross section measurements from various fixed target experiments are shown in Figure 2.2, along with the sensitivities to choice of the charm quark mass, m_c.

Virtually all of the photon energy is transferred to the $c\bar{c}$ quark pair, the charmed particles are boosted forward by a large Lorentz factor, thereby reducing the aperture of spectrometer needed to detect the decay fragments of the charmed particles. The large Lorentz factor allows the observation of the charmed particle lifetimes and

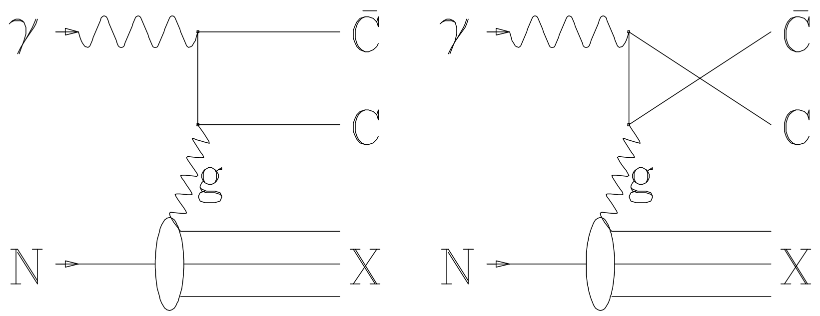

Figure 2.1: The lowest order photon-gluon fusion diagrams.

discrimination of the charm signals from backgrounds by using the significance of separation between charm production and decay vertices.

2.3 Charmed Baryons

The ground-state charmed baryons are classified as usual as members of the SU(4) 20-plets as depicted in Figure 2.3. The $J^P = \frac{1}{2}^+$ ground state baryons comprise the SU(3) 20-plets and $J^P = \frac{3}{2}^+$ ground state baryons comprise the SU(3) 20-plet. All the particles in a given SU(4) multiplet have the same spin and parity. It needs hardly be said that the flavor symmetries in a SU(4) are very badly broken, the diagrams in Figure 2.3 are the simplest way to see what charmed baryons should exist. The only charmed baryons which have been experimentally observed are those which contain one charm quark and thus belong to the second level of SU(4) multiplet. The experimental values [14] of the observed charmed baryons are listed in Table 2.2. In the table, $[ab]$ and $\{ab\}$ denote antisymmetric and symmetric flavor index combinations, respectively. The $J^P = \frac{3}{2}^+$ charmed baryons are predicted to be massive enough to decay to $J^P = \frac{1}{2}^+$ charmed baryons with emitting a pion. A very limited experimental information [19, 20] on the $J^P = \frac{3}{2}^+$ charmed baryons are currently available.

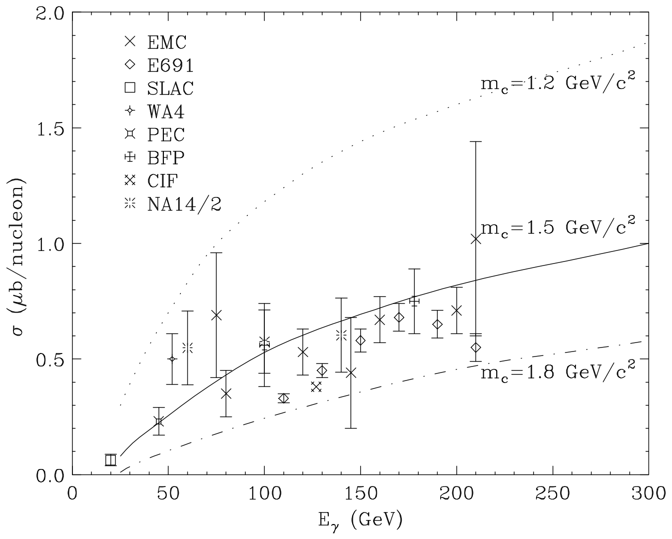

Figure 2.2: Total charm photoproduction cross-section measurements vs. photon energies.

Table 2.2: Properties of the experimentally observed charm baryons.

Notation	Quark content	Mass(MeV/c^2)
Λ_c^+	$c[ud]$	2284.9$\pm$0.6
Ξ_c^+	$c[su]$	2465.6$\pm$1.4
Ξ_c^0	$c[sd]$	2470.3$\pm$1.8
Σ_c^{++}	cuu	2452.9$\pm$0.6
Σ_c^+	$c\{ud\}$	2453.5$\pm$0.9
Σ_c^0	cdd	2452.1$\pm$0.7
Ω_c^0	css	2704.0$\pm$4.0

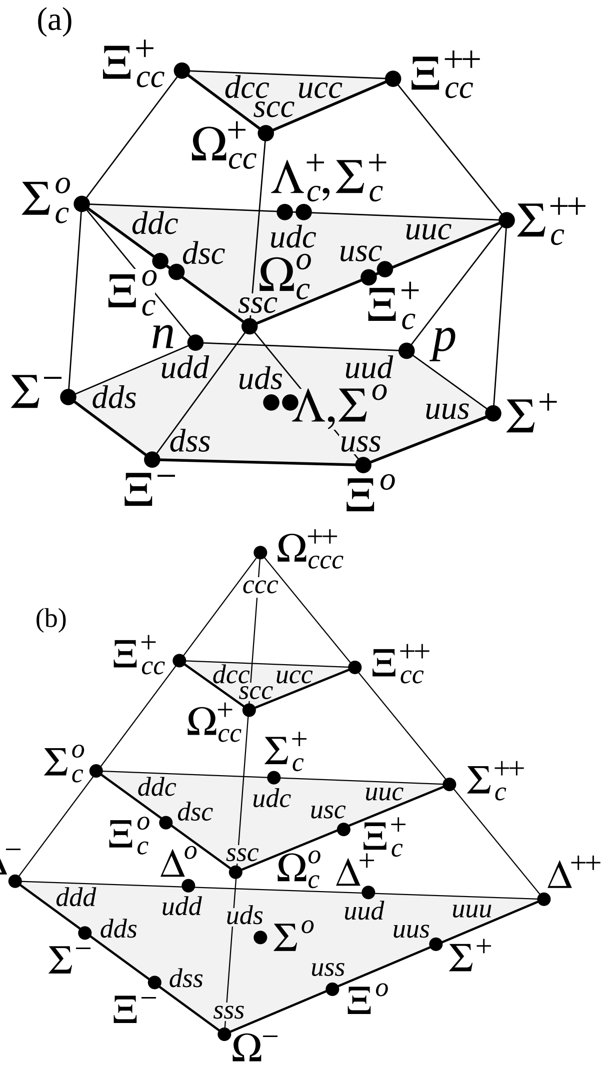

Figure 2.3: SU(4) multiplets of baryons made of u, d, s, and c quarks: (a) $J^P = \frac{1}{2}^+$ 20-plet with an SU(3) octet on the lowest level; (b) $J^P = \frac{3}{2}^+$ 20-plet with an SU(3) decuplet on the lowest level.

The remaining mass entries are taken from theoretical calculations [15, 16] based on a central two-body potential supplemented by the spin-spin interaction

$$H_{ss} = \sum_{i<j} \frac{16\pi\alpha_s}{9m_i m_j} s_i s_j \delta^3(r_{ij}) \tag{2.1}$$

where one has just added two-body potentials between quarks $i(j)$ with masses $m_i(m_j)$ and spins $s_i(s_j)$ separated by the distance r_{ij}. The spin-spin interaction term results from the Breit-Fermi reduction of the one-gluon exchange interaction. Many authors have emphasized the fact that the hyperfine splitting resulting from Equation 2.1 is crucial to the understanding of the mass-breaking pattern of both charmed and charmless hadrons [17, 18]. As long as the spin-spin interaction term is taken account for, a variety of models with differing degrees of sophistication will basically reproduce the pattern of charm baryon masses. None of the doubly and triply charmed baryons have been observed, however, all of them are expected to decay via weak interaction.

2.3.1 Weak Decay of Charmed Hadrons

Singly charmed particles decay via weak interaction. The strong or electromagnetic decay of charmed particles can only occur to ground-state charmed hadrons based on the conservation of charm quantum number. The decay processes of the charmed hadrons are spectator model, W-exchange, and W-annihilation as shown in Figure 2.4.

The spectator diagram is believed to play a dominant role in most charmed particle decays. In this model, a charm quark decays to a lighter quark with emitting a W^+ boson and the remaining constituent quarks of the hadron are assumed to be spectators and do not affect the process.

From the spectator model and the universality of the weak interaction, we can naively estimate the charm quark lifetime from the muon lifetime:

$$\tau_c \;\simeq\; \frac{1}{5}\,\tau_\mu\,(\frac{m_\mu}{m_c})^5$$

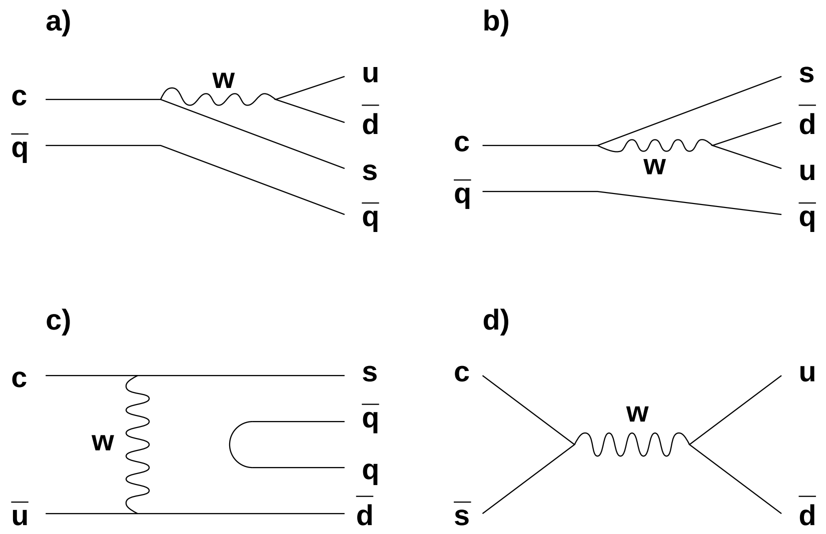

Figure 2.4: Quark level diagrams for hadronic charmed meson decays: a) external W-emmision b) internal W-emmision c) W-exchange d) W-annihilation.

where τ_μ and m_μ are the lifetime and mass of the muon, m_c is the charm quark mass. The factor of 1/5 accounts for the two leptons(electron and muon) and three quark colors which the charm quark can decay into. This model roughly estimates charm hadron lifetimes on the order of 10^{-12} seconds. Since the color degree of freedom of the coupling quarks in the internal spectator diagram must match, the internal W-emission decay rate is suppressed in the decay of charmed mesons.

Although the spectator model provides a rough estimation of the charmed hadron lifetime, there are difference among measurements of various charmed hadrons. We need the W-exchange and W-annihilation processes to explain the difference. The two processes contribute about 20% to the total decay width. In the case of charmed mesons, the decay rate for both W-exchange and W-annihilation are helicity-suppressed.

In the case of charmed baryons, the W-exchange process is neither helicity nor color suppressed by the presence of the additional light quark. The W-exchange and

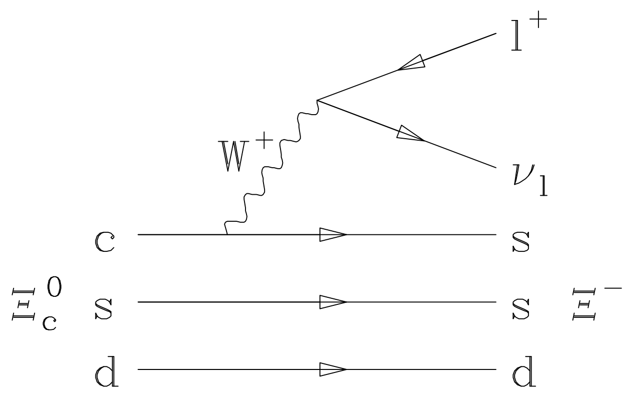

Figure 2.5: The spectator diagram for the decay of $\Xi_c^0 \longrightarrow \Xi^- l^+ \nu$.

the internal spectator mechanisms may contribute significantly to the total charmed baryon decay rate. We can also expect the contribution of the constructive(or destructive) interference between the $s(d)$ quark from the charm decay and the spectator $s(d)$ quark in the charmed baryon. A dramatic interference contribution is predicted in the Ξ_c^0 and Ω_c^0 decays [21] and could be confirmed experimentally.

2.3.2 Semileptonic Decay of Ξ_c^0

The semileptonic decay provides the valuable information of the weak decays and the Cabibbo-Kobayash-Maskawa(CKM) mixing matrix. The leading order diagram which contributes to the semileptonic decay of the charmed baryon is the spectator diagram. The spectator diagram of $\Xi_c^0 \longrightarrow \Xi^- l^+ \nu$ decay is shown in Figure 2.5.

In the spectator model, the *charm* quark decays weakly into the *strange* quark with emitting of a W^+ boson. The W boson materializes into a lepton-neutrino pair and the spectator quarks(s and d) do not interact.

Although the spectator model provides a reasonable description of many semileptonic decays, the discrepancies between experiment and theory as well as among experiments are still large.

For the process of $\Xi_c^0 \longrightarrow \Xi^- l^+ \nu$, the decay rate is given by

$$d\Gamma(\Xi_c^0 \longrightarrow \Xi^- l^+ \nu) = \frac{1}{2M} \mid A(\Xi_c^0 \longrightarrow \Xi^- l^+ \nu) \mid^2 d\Pi_3, \tag{2.2}$$

where

$$d\Pi_3 = (2\pi)^4 \delta^{(4)}(P - k - p - p^{'}) \prod_f \frac{d^3 k_f}{(2\pi)^3 2E_f}, \tag{2.3}$$

and

$$A(\Xi_c^0 \longrightarrow \Xi^- l^+ \nu) = \frac{G_F}{\sqrt{2}} V_{cs} L^\mu H_\mu^{(s^{'} s)} \tag{2.4}$$

with V_{cs} being the CKM matrix element approximate to the $c \rightarrow s$ transition and where the product is over all final-state momenta. The $s^{'}$ and s are spin components and the parent has four momenta P, the daughter k, the lepton and neutrino have p and $p^{'}$ respectively. The virtual W^+ carries four-momentum $q = p + p^{'}$. The spin-quantization axes for the parent and daughter baryons are not necessarily the same.

The lepton and hadronic currents are given by

$$L^\mu = \overline{u}_l \gamma^\mu (1 - \gamma_5) v_\nu,$$

$$H^{(s^{'} s)\mu} = < k, s^{'} \mid J_{had}^\mu(0) \mid P, s > .$$

The hadronic current can be constructed from Lorentz invariant form factors and the four-vectors of the problem. Writing $J_{had}^\mu = V^\mu - A^\mu$, we define

$$
\begin{aligned}
< k \mid V^{\mu}(0) \mid P > \;&=\; \overline{u}_m[g(q^2)\gamma^{\mu} + g_{+}(q^2)(P+K)^{\mu} \\
&\quad + g_{-}(q^2)(P-k)^{\mu}]u_M, \\
< k \mid A^{\mu}(0) \mid P > \;&=\; \overline{u}_m[a(q^2)\gamma^{\mu} q\gamma_5 + a_{+}(q^2)(P+K)^{\mu}\gamma_5 \\
&\quad + a_{-}(q^2)(P-k)^{\mu}\gamma_5]u_M,
\end{aligned} \tag{2.5}
$$

where $q^2 = (P-k)^2$ and $u_M(u_m)$ is the spinor associated with the parent(daughter) baryon and spin labels have been suppressed.

2.4 The Experimental Status

The previous measurements on semileptonic decays of the Ξ_c^0 come from the ARGUS [22] and CLEO [23] experiments. ARGUS published the inclusive semileptonic decays, $\frac{\Gamma(\Xi_c^0 \longrightarrow \Xi^- l^+ X)}{\Gamma(\Xi_c^0 \longrightarrow \Xi^- \pi^+)} = 0.96 \pm 0.43 \pm 0.18$ with 18.1 ± 5.9 events (12.6 ± 4.9 events for the electron mode, 5.5 ± 3.3 events for the muon mode). CLEO published the exclusive decay, $\frac{\Gamma(\Xi_c^0 \longrightarrow \Xi^- e^+ \nu)}{\Gamma(\Xi_c^0 \longrightarrow \Xi^- \pi^+)} = 3.1 \pm 1.0^{+0.3}_{-0.5}$ with 54 ± 10 events. Although the errors are large there is still more than 1.8 σ discrepancy between the two measurements.

Chapter 3

The E687 Apparatus

The E687 experiment at Fermilab is designed to study the production and decay of particles containing a charm quark using the high energy photon beam. The charmed particles are produced during the interactions of high energy photons with matter.

Since the charm production cross section is relatively large fraction of the total hadronic cross section at high photon energies and this method creates a relatively clean charmed particles. The high energy photon beams are good sources of investigating charmed particles.

The experimental apparatus consists of the beamline, which produces the high energy photons projected to the experimental target and the spectrometer designed to detect interacted particles at the production target.

In this chapter, we shall first describe the beamline in which an intense high energy photon beam is created, from the creation process using the Fermilab Tevatron proton beam to the interaction of the photons to the E687 experimental target. A brief physical description of each individual detector component of E687 spectrometer is described in this chapter with more detailed discussions devoted to the spectrometer components particularly crucial to this analysis. A detailed description of the E687 spectrometer can be found in reference [27]. The E687 data acquisition system is described in the later part of this chapter.

3.1 Beam Line

The E687 high intensity and high energy photon beam is produced by a complicated process. The Fermilab wide band photon beam is delivered from the 800 GeV protons using Fermilab Proton East(PE) beamline.

3.1.1 The Proton Beam

The proton of Fermilab is derived from hydrogen ions. Ionized hydrogen is accelerated to 750 KeV at Cockcroft-Walton voltage multiplier. Hydrogen ions pass through a carbon foil and the electron is stripped from the ions, leaving the protons to be sent into linear accelerator where they are boosted to 400 MeV.

The proton are then sent to booster ring, a rapid cycling synchrotron of 150 m in diameter which accelerates them up to 8 GeV. The protons are fed into the Fermilab main ring, a larger proton synchrotron which uses conventional cooper coiled magnets. At this stage, the proton beam is raised to an energy of 150 GeV. These protons are injected into the superconducting synchrotron (called as Tevatron) which consists of a thousand superconducting magnets, and accelerated to its final energy of 800 GeV. The intensity of the proton beam is about 2×10^{13} protons per 23 sec spill.

The Tevatron proton beam is extracted by a deflecting magnet and it is used to produce three different secondary beams of particles, protons, mesons, and neutrinos. The experiment of E687 is located at the end of proton beamline as shown in Figure 3.1. The proton beam must be converted to the photon beam to utilize it at the Wide Band(WB) photon laboratory.

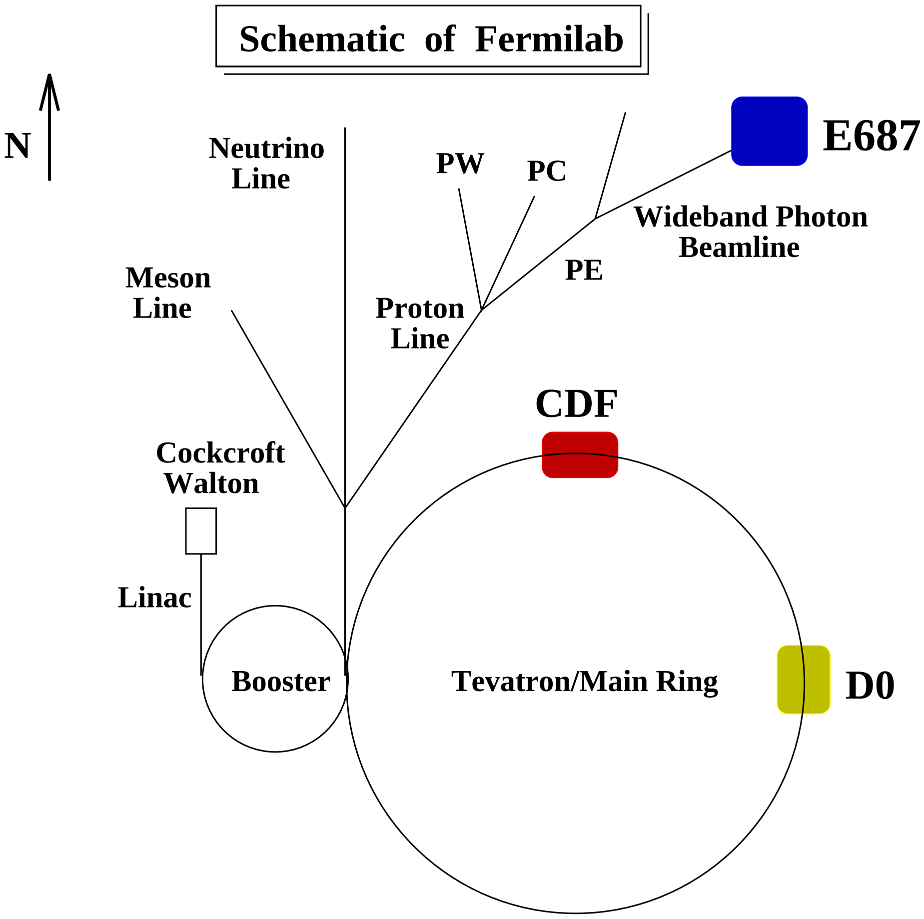

Figure 3.1: Schematic drawing of Fermilab.

3.1.2 The Photon Beam

The photon beam is produced by impinging 800 GeV proton beam on a 3.4 m long liquid deuterium target (primary production) which is corresponding to one proton interaction length. As the protons interact in the target, electrically charged and neutral pions (among with other neutral particles) are created and neutral pions immediately decay into two photons. The charged particles are swept away from the beam direction by sweeping magnets located immediately downstream of the target. The neutral beams pass through a small hole in the dump and impact on a lead converter, which has a thickness of 0.6 radiation length, where they produce electron-positron pairs.

The electrons are bent away from the beam direction and then captured by a conventional beam transport consisting of dipole magnets and quadruples. The positrons are also bent away and sent to a beam dump. The remaining neutral hadrons, neutrons and K_L^0's, along with unconverted photons, travel straight ahead at zero degrees and are absorbed in a neutral dump.

The beam transport optics are designed to select electrons with nominal momentum of 350 GeV/c . In order to obtain a high flux, electrons in a momentum range $\pm 13\%$ around the nominal setup are collected in the transport. At this point, the electron momentum is tagged with a system of magnets and silicon microstrip detector. This tagging procedure will be described in the following section. The electron, composed of $\sim 10^8$ electrons/spill is realigned with the original direction.

The electron beam is transported around the dump and is eventually passed through a thin lead foil, a radiator of 0.27 radiation length to produce photons by bremsstrahlung. The electron is then deflected off to the side by dipole magnets, electron sweepers, and into an electron dump while the photon passes straight ahead to the experimental target. The steps required to produce a photon beam is shown in Figure 3.2.

The final photon beam has very little hadron contamination, about 1 hadron every 10^5 photons. Taking into account the interaction cross section, the number of events produced by hadronic interaction in the experimental target is $\sim 1\%$ of the photoproduced events. The beam properties are summarized in Table 3.1.

3.1.3 Beam Tagging

A beam tagging system is installed in the E687 beamline whose purpose is not only to determine the energy of photon on an event–by–event basis, but also to

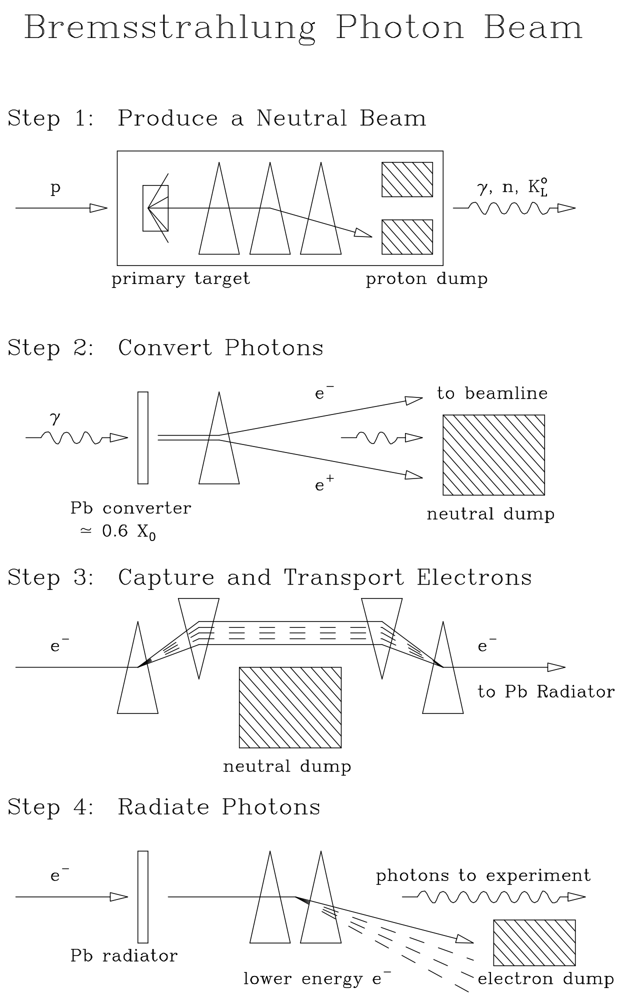

Figure 3.2: Schematic drawing of the steps used to produce the E687 photon beam from the Tevatron proton beam.

Table 3.1: Wide band beam properties

Property	Value
Horizontal spot size at production target	$\delta x = \pm 1$ mm
Vertical spot size at production target	$\delta y = \pm 1$ mm
Geometric horizontal angle accepted	$\delta\theta_x = \pm 1.0$ mrad
Geometric vertical angle accepted	$\delta\theta_y = \pm 0.75$ mrad
Geometric solid angle accepted	$\Delta\Omega = 6.0$ μsr
Maximum momentum bite	Δp/p $\approx \pm 15\%$
Effective acceptance	$\Delta\Omega \times \Delta$p/p ≈ 96 μsr%
Horizontal spot at experimental target	$\delta x = \pm 1.25$ cm
Vertical spot at experimental target	$\delta y = \pm 0.75$ cm
Horizontal divergence at experimental target	$\delta\theta_x = \pm 0.6$ mrad
Vertical divergence at experimental target	$\delta\theta_y = \pm 0.5$ mrad

require a minimum acceptable photon energy in the second–level trigger. The energy of interacting photon is determined by measuring the electron momentum before and after the radiator, and measuring the energy of any non-interacting photons which are created by multiple bremsstrahlung. The tagging system consists of three independent detectors: the silicon microstrip tagging system, the Recoil Electron Shower Hodoscope detector (RESH), and the Beam Gamma Monitor (BGM) [29].

The silicon microstrip tagging system consists of five large area silicon microstrip planes installed around the final two dipole magnets of the electron beam transport system. Two planes are located upstream of the dipole magnets, one plane is between the magnets, and two planes are downstream. Each 7.7 cm $\times$ 5.7 cm silicon microstrip plane is composed of 256 silicon strips of 300 μm pitch for a total of 1,280 channels. The microstrip system accurately measures the deflection angle of the electron as it traverses the dipole magnets and provides a 2.2% momentum resolution.

The RESH is located downstream of the final lead radiator and measures the electron momentum after it has emitted bremsstrahlung photons. The RESH consists of 10 hodoscope counters, which are either lead–lucite or lead–acrylic scintillator shower counters of about 24 radiation length in depth, arranged perpendicular to the photon beam direction. A phototube is used to collect the Čerenkov light created in the lucite when an electron develops an electromagnetic shower. The struck counter determines the bend angle of the electron and thus the momentum. The BGM is a segmented lead–lucite calorimeter, located between the inner electromagnetic calorimeter and the hadron calorimeter. The BGM has 24 radiation lengths in depth and is designed to measure the electromagnetic shower energies resulting from multiple bremsstrahlung photons created in the upstream lead radiator. During the second run period in 1991, the BGM has replaced by the beam calorimeter (BCAL) which is provided by the downstream experiment E683.

With the energies recorded in each detector, the energy of interacting photon can be calculated from

$$E_\gamma = E_{e^-}^{\text{inc}} - E_{e^-}^{\text{RESH}} - \sum E_\gamma^{\text{BGM}}$$

where

- $E_{e^-}^{\text{inc}}$ is the incident electron energy measured by the silicon microstrip tagging system,
- $E_{e^-}^{\text{RESH}}$ is the recoil electron energy after emitting a bremsstrahlung photon in the radiator, which is determined by the RESH,
- $\sum E_\gamma^{\text{BGM}}$ is the total energy deposited in the BGM by non-interacting photons.

Figure 3.3 shows the energy spectra measured in each detector, respectively. The mean tagged photon energy was about 210 GeV and approximately 60% of the photon triggers has an acceptable energy tag due to the limited acceptance of the RESH counter.

3.1.4 Target

The target is composed of beryllium segments, each 2.54 cm × 2.54 cm in size and 0.4 cm in thickness. Two slightly different target configurations were used during the run. Approximately 37% of the data was taken with a nine–segment target of beryllium and the remaining portion using an eleven–segment target. The square segments are aligned with the high resolution region of the silicon microstrip detector. The nine–segment target has an over all radiation length of 10% and a proton interaction length of 8.8% whereas the eleven–segment target has 12.5% radiation length and 10.8% interaction length. Details of the target configuration are summarized in Table 3.2.

Several factors were taken into considerations in the choice of beryllium as a target material. The hadronic cross section is approximately proportional to the atomic

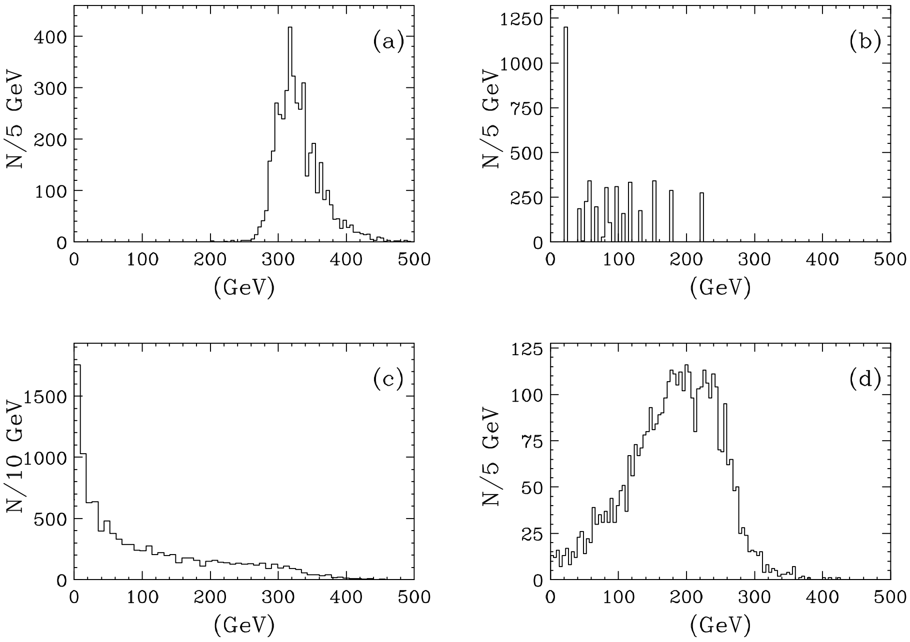

Figure 3.3: Typical energy spectra: (a) the incident electron energy distribution, (b) the energy distribution of recoil electron, (c) the energy spectrum of bremsstrahlung photons, and (d) the energy spectrum of interacting photon.

weight, A, whereas the e^+e^- pair production rate is proportional to the square of the atomic number, Z^2. To maximize the hadronic/electromagnetic production ratio one chooses a material with a large $A/Z^2 \sim 2/Z$ ratio. Another consideration is to have a target of appropriate dimensions to allow for a sufficient hadronic interaction (and hence the charm production rate) while being compact enough to reduce the interaction of charmed hadrons and their decay products with the target material. Beryllium was consequently chosen as the target material since it satisfies the above requirements.

Table 3.2: Target configurations for the 1990 and 1991 runs.

	Configuration–I	Configuration–II
No. of segments	9	10
Total length (cm)	3.6	4.4
Interaction length (%)	8.8	10.8
Radiation length (%)	10	12.5

3.2 The E687 Spectrometer

The E687 spectrometer is a large aperture and multi–purpose detector system in the Wide Band experimental hall at Fermilab [27]. A silicon microstrip detector installed in the region closed to the interaction point provides an excellent vertex resolution. A multiwire proportional chamber system and two analysis magnets provide charged particle tracking and momentum information. Three multi–cell threshold Čerenkov detectors, two electromagnetic calorimeters, and two muon systems identify charged particles. Neutral particles are detected by two electromagnetic calorimeters and two hadron calorimeters. Figure 3.4 shows a schematic drawing of the E687 spectrometer characterizing the relative size and location of individual detector components.

3.2.1 Silicon Microstrip Detector

The Silicon Miscristrip Detector (SSD) is designed to perform high resolution tracking of charged particles in the region immediately downstream of the production point. The geometrical layout of the detector is shown in Figure 3.5 and is described in Table 3.3.

The SSD consist of twelve microstrip planes grouped in four stations of three detectors measuring i, j and k coordinates respectively. The strips of one plane

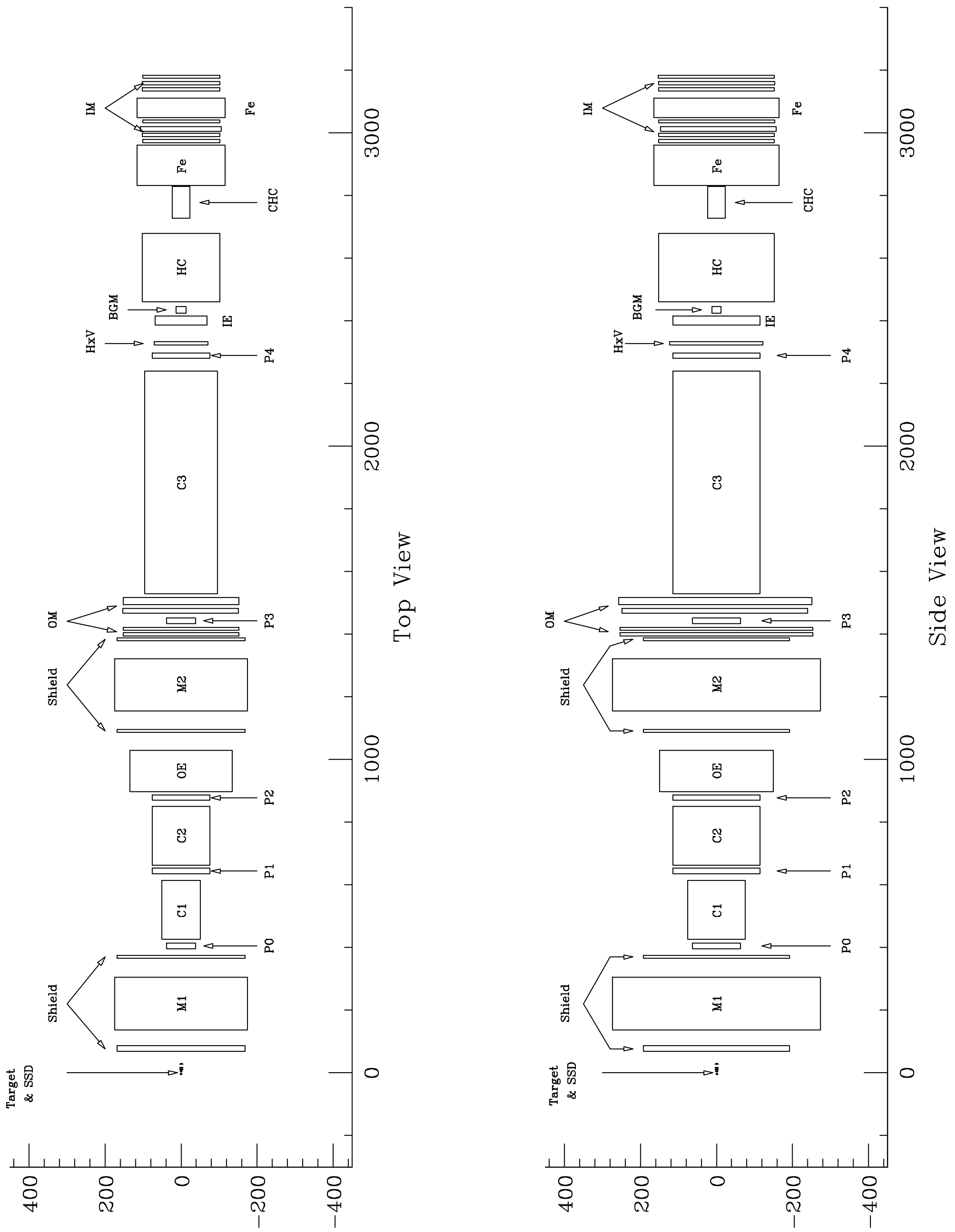

Figure 3.4: Schematic drawing of the E687 spectrometer. Both the horizontal and vertical scales are in centimeters.

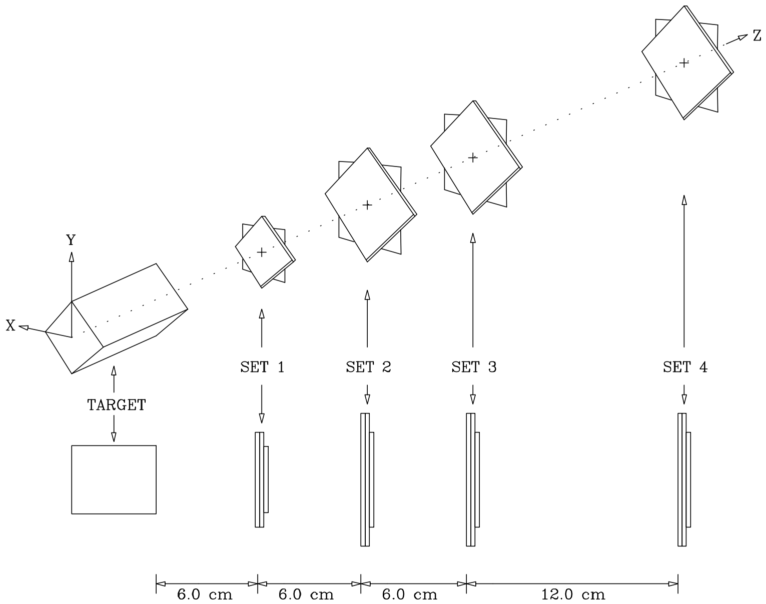

Figure 3.5: Schematic drawing of the SSD layout.

Table 3.3: Microstrip detector properties.

Property	Station I	Station II	Station III	Station IV
Z position (cm)	0.0	6.0	12.0	24.0
Active area (cm^2)	2.5×3.5	5.0×5.0	5.0×5.0	5.0×5.0
High resolution area (cm^2)	1.0×3.5	2.0×5.0	2.0×5.0	2.0×5.0
Pitch (High/Low Res.) (μm)	25/50	50/100	50/100	50/100
No. of channels	3×688	3×688	3×688	3×688

in each station are oriented vertically, while the strips of the other two planes are situated at $\pm 45^0$ with respect to the horizontal axis (X-axis) of the spectrometer. In order to maximize the spatial resolution while limiting the number of electronic channels, the pitch of the silicon strips in the central region of each plane was chosen to be half size of the pitch in the outer region. This is because the central region is typically crossed by the most energetic tracks which are closer to one another and less deflected by Coulomb scattering. In addition, the pitch on the three planes of the triplet which is closest to the target was chosen to be half of the other triplets because the station nearest the target is the most important for the determination of the decay vertex.

The analog pulse height is read out for each strip. The pulse height provides a simple estimate for the number of charged tracks involved in a serious of adjacent hits.

The high resolution tracking performed by the miscrostrip detector allow us to determine the point of origin of the track in the target region with a precision of about $\sim$ 500 μm in the beam direction and $\sim$ 10 μm in the transverse direction. The overall detection effiency of each plane is measured to be better than 99% including non-functioning strips and broken electronics channels.

3.2.2 Analysis Magnets

The momentum of a charged particle is determined by measuring the deflection of the particle by two large magnetic fields. The first analysis magnet (M1), located about 225 cm downstream of the target, is operated at a current of 1,020 A to give a transverse momentum kick of 0.400 GeV/c. The second analysis magnet (M2), situated about 1,240 cm downstream of the target, is run at a current of 2,000 A for a transverse momentum kick of 0.850 GeV/c. The two analysis magnets are operated with opposite polarities, so that they bend a charged particle to the opposite directions in the transverse plane (Y–view). The aperture size of each magnet is ± 38.1 cm in X–view and ± 63.5 cm in Y–view.

This particular arrangement of magnet positions and momentum kicks was determined for its unique effect on the event topology. The ratio of the momentum kicks is designed to focus e^+e^- pairs on the BGM. At a given fixed geometrical downstream detector acceptance and fixed transverse momentum kicks, the spectrometer acceptance is higher when the magnets provide opposite momentum kicks than when they bend particles in the same direction.

3.2.3 Multiwire Proportional Chambers

The 20 signal planes of the multiwire proportional chamber are grouped into five stations with four planes per each. Each station has four different views, X, Y, U, and V views. The U and V views are oriented to $\pm 11.3^0$ from the Y view. The first three chambers are labeled P0, P1, and P2 and are located between the two analysis magnets. The P3 and P4 are located downstream of the second analysis magnet. There are two types of chamber stations depend on location. The P0 and P3 (Type I) are located just downstream of analysis magnets and are smaller than the P1, P2 and P4(Type II). The physical properties of each chamber are summarized in Table 3.4

The gas mixture used is 65%–35% Ar-Ethane and is bubbled through ethyle alcohol at 0^oC before being distributed to the system. Using this gas mixture, operating voltages of cathode planes are set to 3.30-3.50 kV for the Type I and 3.00-3.50 kV for the Type II in order to produce good efficiency.

3.2.4 Čerenkov Detectors

The three multicell threshold Čerenkov counters, C1, C2 and C3 are used for charged particle identification. The counters are all run at atmospheric pressure in the threshold mode. The gases have been chosen so that there is a wide range of momentum values in which pions, kaons and protons can be identified. The charged

Table 3.4: Properties of multiwire proportional chamber system

Property	P0	P1	P2	P3	P4
active area(in^2)	30×50	60×90	60×90	30×50	60×90
wire spacing(mil.)	80	120	120	80	120
anode-cathode half gap(in.)	0.235	0.240	0.240	0.235	0.240
anode wire diameter(mil.)	0.8	1.0	1.0	0.8	1.0
cathode wire diameter(mil.)	2.5	3.5	3.5	2.5	3.5
equivalent tension(gram)	65	90	90	65	90
No. of X-view wires	376	512	512	376	512
No. of Y-view wires	640	768	768	640	768
No. of U/V-view wires	640	842	842	640	842

particles which exceed the speed of light in the medium create Čerenkov lights around the direction of travel if its velocity is above the threshold value:

$$\beta = \frac{pc}{E} \geq \beta_{\text{threshold}} = \frac{1}{n},$$

or, equivalently momentum is above the threshold momentum:

$$p_{\text{threshold}} = \frac{mc}{\sqrt{2(n-1)+(n-1)^2}}$$

where c is the speed of light, m is the mass of particle and n is the refraction index of the medium. The physical characteristics of three counters are summarized in Table 3.5

Particle identification is accomplished by noting that the certain momentum ranges, a particle of given mass makes counters on and off. The identification regions for tracks are summarized in Table 3.6

Table 3.5: Characteristics of the Čerenkov counters.

Counter	Gas	Threshold momentum (GeV/c)			No. of cells
		pion	kaon	proton	
C1	80% He / 20% N_2	6.7	23.3	44.3	90
C2	N_2O	4.5	16.2	30.9	110
C3	He	17.0	61.0	116.2	100

3.2.5 Electromagnetic Calorimeter

The Electromagnetic Calorimeters are designed to detect electrons and photons. There are two separate electromagnetic calorimeters in the E687 experiment, the Inner Electromagnetic Calorimeter (IE) is situated for the small angle and the Outer Electromagnetic Calorimeter (OE) is located for the wide angle.

Inner Electromagnetic Calorimeter

The Inner Electromagnetic Calorimeter is a lead sampling calorimeter composed primarily of a hundred alternating lead layers and scintillating fibers. Each lead sheet is 0.14 cm thick and the scintillating fiber is 0.75 mm in diameters. The fiber orientation alternates between horizontal and vertical throughout the length of the calorimeter. The active area is 137 cm in the non-bend (X) view and 228 cm in the bend (Y) view, and 10 cm $\times$ 10 cm hole was left in the center to allow non-interacting beam photons and e^+e^- pairs to pass through the calorimeter. The angular acceptance is ± 28 mrad in the non bend plane and ± 47 mrad in the bend plane. The IE is 25 cm deep, which is corresponding to 25 radiation lengths and 1 proton interaction length. The calorimeter is segmented longitudinally into three modules, and transversely into five quadrants. The modules are 5, 10, and 10

Table 3.6: Particle identification ranges.

Particle	Momentum ranges (GeV/c)	
	5–chamber track	3–chamber track
e	0.16 – 17.0	0.16 – 6.7
π	4.5 – 17.0	4.5 – 6.7
K	17.0 – 44.3	17.0 – 23.3
p	17.0 – 44.3 & 60.8 – 116.2	17.0 – 44.3
e/π	17.0 – 61.0	6.7 – 23.3
K/p	4.5 – 61.0	4.5 – 17.0
$e/\pi/K$	61.0 – 116.2	30.9 – 61.0
$\pi/K/p$	0.16 – 4.5	0.16 – 4.5

radiation lengths deep respectively. Each module consists of layers of scintillating fibers sandwiched between sheets of lead. Layers of fibers are arranged vertically and horizontally in alternating order to give X and Y views.

The three Pb/fiber modules are separated by two polystyrene scintillator layers. The plastic scintillator plane is composed of 78 individual strips 0.95 cm thick and 5.08 cm wide. The strips are oriented at 45^0 with respect to the spectrometer's Y-axis and are used to resolve ambiguities associated with multiple showers occurring in close promity to each other. These two planes are called tie-breakers and are referred to as IE1T and IE2T respectively. A lead shield was mounted directly in front of the calorimeter for the 1991 run to absorb electromagnetic pairs. The shield is 5.08 cm wide and runs vertically along the Y axis to cover the region which experiences a high rate of the $\gamma \rightarrow e^+e^-$ events. This lead absorber is 10.16 cm, corresponding to 18.1 radiation length and dramatically reduces the amount of energy deposited in the IE by electromagnetic pairs.

Outer Electromagnetic Calorimeter

The OE calorimeter is 9 m downstream of the target, just upstream of M2. The outer electromagnetic calorimeter is a lead sampling calorimeter organized into five modules. Each module is constructed of altering layers of plastic scintillator, lead and aluminum. The OE is 18.7 radiation lengths and 1.8 proton interaction lengths deep. The angular acceptance is $28 \leq \mid \theta_x \mid \leq 142$ mrad in the non-bend view and $49 \leq \mid \theta_y \mid \leq 114$ mrad in the bend view.

3.2.6 Hadron Calorimeter

The Hadron Calorimeter is primary designed to provide a trigger mechanism which selects hadronic events and rejects electromagnetic background events like e^+e^- pairs with requiring a certain minimum hadronic energy.

The hadron calorimeter covers only the inner portion with two separate devices. The main hadron calorimeter(HC), which is iron gas sampling calorimeter and covers the region from 5 mrad to approximately 30 mrad. The central hadron calorimeter(CHC) covers the central 5 mrad region centered directly on the photon beam. The absorber of HC is 8 interaction lengths and are separated by 2.86 cm wide gaps where the sense planes are inserted. The material in the CHC is about 6.3 interaction lengths for the 1990 run and 7.3 interaction lengths for the 1991 run.

3.2.7 Muon Detectors

Two separate muon systems are used in the identification of muons. The outer Muon system was used for wide angle muon identification extending to 125 mrad and the inner muon system was designed to identify muons at less than 40 mrad. In Figure 3.6, we show the layout of the muon planes and shields.

Outer Muon System

The outer muon system consists of two planes of proportional tubes and two planes of scintillation counters. The system uses the second analysis magnet, at 10 interaction lengths as a hadron filter.

Inner Muon System

The inner muon system is located at the most downstream of the spectrometer. The electromagnetic and hadron calorimeter are used to filter out electrons and hadrons. Additional shielding is placed around central hadron calorimeter and steel shielding is added downstream of CHC to reduce shower fragments from pions or kaons that are late to interact in the calorimeter.

The system is separated into two stations. The first station consists of a scintillator array that measures the vertical view(IM1H), a scintillator array that measures the horizontal view(IM1V), a proportional tube array that measures the horizontal view(IM1X), and a proportional tube array that measures the vertical view(IM1Y). The second station is located behind additional shielding and is identical to the first station except that no horizontal view scintillator array is used.

In 1990, a readout error limited the utility of this system. Roughly 45% of the 1990 was affected and we do not use this data in any physics analysis. In 1991 the muon system was altered to allow the passage of the photon beam through the detector. A cell of 8 counters was removed from each proportional tube array and the arrays were shifted so that the resultant gap would be centered on the beam. The frame supporting scintillator counters had to be modified and holes were cut in the scintillator planes.

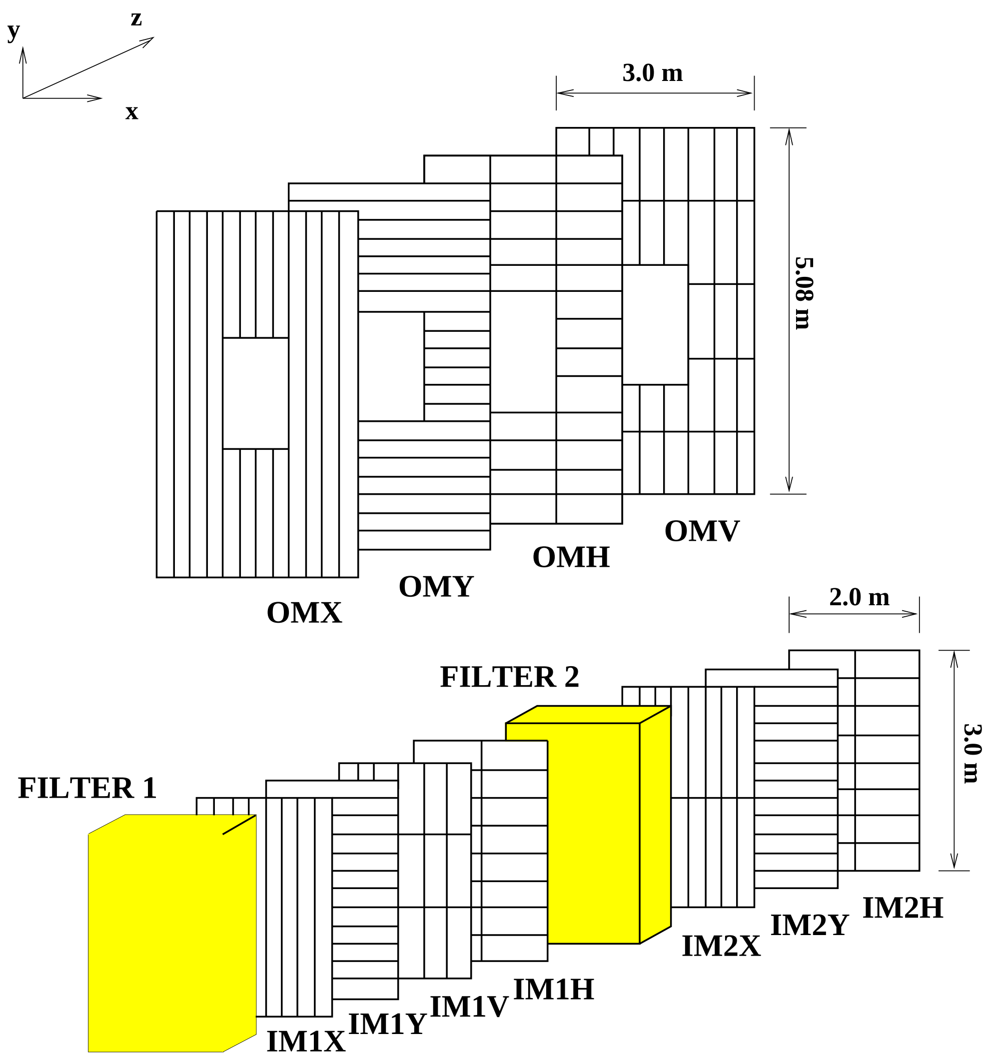

Figure 3.6: Muon detector configuration: a) for Outer Muon b) for Inner Muon

3.2.8 Triggering

The purpose of trigger in the experiment is to isolate the interesting events from undesirable events. In E687 the number of interactions per spill produced by photon beam impinging on the target is about 10^6 and the production of electromagnetic events ($\gamma Be \rightarrow e^+e^-$) is about 500 times to hadronic production. The data acquisition system which operated in the kHz range and was unable to tolerate at such high rate. The E687 trigger system was designed to trigger hadronic events and to reject electromagnetic events and low energy photon events. The triggering is done in two stages to achieve the above goal.

First Level Trigger

In the first level trigger, called as master gate(MG), consists of the coincidence of signals from various fast scintillation counters.

A0 and A1 are small counters placed just upstream of target and used to veto charged particle in the beam. TM1 and TM2 are large scintillation counters placed directly downstream of the A1 counter with big center hole. These are used to veto the charged particles resulted comes from muon production, called as halo muons, in the steel block which is used to filter out neutral particles created by the protons interacting in the deuterium target. Only about 20% of runs these counter were included in the trigger since we found the inclusion of these counters in the trigger is unnecessary.

Two scintillator counters are positioned around microstrip detectors to determine whether a charged particle passed through the SSD. A scintillation counter(TR1) is placed between the target and the microvertex to detect the charged particles that come from interactions in the target. Another scintillation counter(TR2) is placed directly downstream of the microvertex. TR1 is 2.5 cm $\times$ 3.5 cm to match the dimensions of the microvertex planes, TR2 is 22 cm $\times$ 22 cm which is much larger than TR1 in order to accept wide angle tracks exiting microstrip detector. A coincidence of TR1 and TR2 are required to ensure that a photon interacted in the target. The arrangement of trigger counter around target regions is shown in Figure 3.7

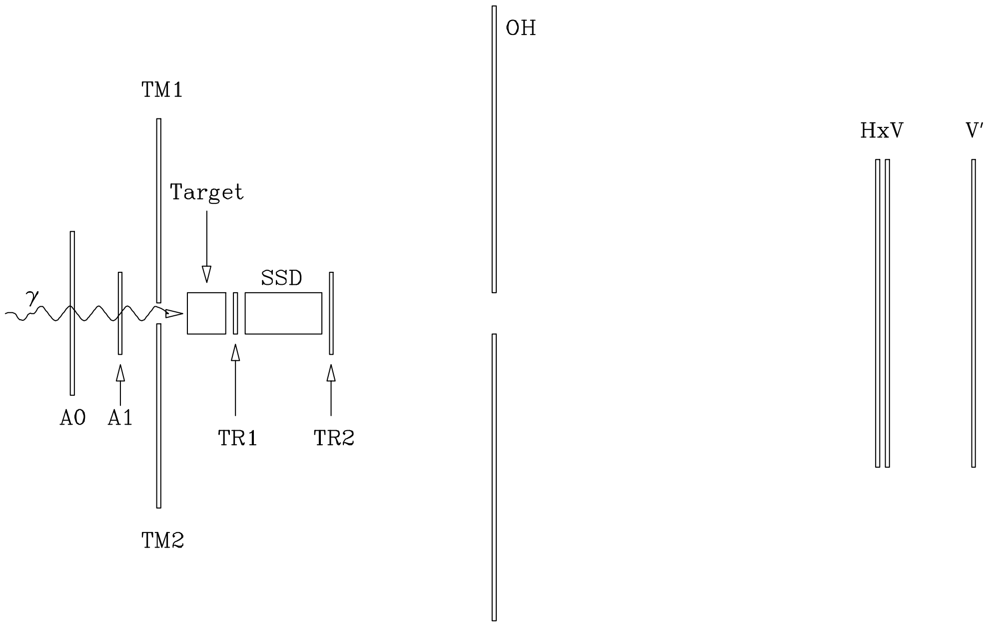

Figure 3.7: Schematic arrangement of the first level trigger counters.

The OH array is a plane of scintillation counters located between P2 and OE with 48.6 cm $\times$ 83.2 cm aperture in the center to allow the e^+e^- pairs to pass through. OH is oriented only in the horizontal direction and is designed to cover the wide angle portion of the spectrometer. The H$\times$V array hodoscope is located between P4 and IE and comprised of 24 horizontal and 12 vertical scintillation counters. The array has a 9.7 cm vertical gap along the center to avoid triggering on e^+e^- pairs which populate the region of the gap. In 1991 we added a plane of scintillation counters, V' behind the IE and a lead bar in front of the IE that covers the region expected e^+e^- pair events. The V' counters work with the H counters to further reduce the pair contamination by making advantage of the shielding power of the IE. The OH and H$\times$V together cover the entire region of acceptance of the spectrometer. The triggering can be made in either of two ways, inner-inner trigger, at least two hits in H$\times$V hodoscope and inner-outer trigger requires a coincidence between a hit in the OH hodoscope and a hit in the H$\times$V. The first level trigger configurations for various run periods are listed in Table 3.7. where $(\mathrm{H}\times\mathrm{V})_1$ indicates hits of H$\times$V by

Table 3.7: First level trigger configurations.

First level trigger logic	Duration
$\mathrm{TR1}\cdot\mathrm{TR2}\cdot(\mathrm{H}\times\mathrm{V})_2\cdot\ \overline{(\mathrm{A0}+\mathrm{A1})}$	26 % of 1990
$\mathrm{TR1}\cdot\mathrm{TR2}\cdot[(\mathrm{H}\times\mathrm{V})_2+\mathrm{OH}\cdot(\mathrm{H}\times\mathrm{V})_1]\cdot\ \overline{(\mathrm{A0}+\mathrm{A1})}$	74 % of 1990
$\mathrm{TR1}\cdot\mathrm{TR2}\cdot[(\mathrm{H}\times\mathrm{V})_2 + \mathrm{OH}\cdot(\mathrm{H}\times\mathrm{V})_1]\cdot\ \overline{(\mathrm{A0}+\mathrm{A1})}$	8 % of 1991
$\mathrm{TR1}\cdot\mathrm{TR2}\cdot(\mathrm{H}\times\mathrm{V})_2\cdot\ \overline{(\mathrm{A0}+\mathrm{A1})}$	5 % of 1991
$\mathrm{TR1}\cdot\mathrm{TR2}\cdot[(\mathrm{H}\times\mathrm{V}')_2 + \mathrm{OH}\cdot(\mathrm{H}\times\mathrm{V}')_1]\cdot\ \overline{(\mathrm{A0}\cdot\mathrm{A1})}$	87 % of 1991

at least one charged particle and $(\mathrm{H}\times\mathrm{V})_2$ by at least two charged particles.

The MG requirement rejects $\sim$ 90% of the e^+e^- pairs, while being 90% efficient in retaining hadronic events. The rate of events passing through the first level trigger is $\sim$ 50 kHz, i.e., $\sim 10^6$ per spill. The ratio of electromagnetic events to hadronic events remains still large ($\sim$ 15:1) and the rate is still too high for the data acquisition system and requires the second level trigger to be implemented.

Second Level Trigger

The second level trigger has been designed to further reduce the event rate and select the hadronic events by combining topological and kinematic requests. In the basic configuration, an event is selected on the following basis:

- the pattern of hits detected by the first station of the MWPC is consistent with at least three charged tracks outside the e^+e^- pair region
- the energy deposited in the Hadron Calorimeter is at least 40$\sim$50 GeV/c^2 . (during the 1990 run the energy deposited in the CHC was included).

This trigger requires about 1.2 μsec to process information latched by the master gate and to decide whether to read out the event or to execute a clear cycle. The trigger operates on signals which are latched and pulse heights which are integrated and stored when a master gate occurs. The second level Buslines are given in Table 3.8.

The OR logic of all the trigger modules constitute the second level trigger. The data acquisition is disabled for an interval needed by the second level electronics to make a level-two trigger decision. The clear cycle is initiated which takes about 1 μsec, and generates a total deadtime of the first level trigger is about 2.2 μsec which fails to produce a second level trigger. If the second level trigger is satisfied, then a full readout and automatic clear cycle is initiated.

3.3 Data Acquisition System

Once the master gate and second level trigger requirements are satisfied, the E687 Data Acquisition(DAQ) system, which is able to process about 10,000 triggers per minute of 6 kB each in size, is alerted to begin the process of transferring data to tape. All signals from the detectors are digitized and sent via five data streams to Lecroy Fastbus memories(4 MB each) as schematically shown in Figure 3.8. The average readout time for each stream is listed in Table 3.9. The further master gates are inhibited for about 1.4 ms to prevent the pile-up of events while the data from an accepted event is being processed. Approximately 30 % of all the first level triggers are lost due to the dead time generated by the second level trigger and DAQ system. During the 20 second spill time about 3,000 events satisfy the second level trigger

Table 3.8: Second level trigger buslines

Busline	Description
1	Muon Anti-coincidence
2	Particle in A0 counter
3	RESH energy > ELOW
4	RESH energy > EMED
5	RESH energy > EHIGH
6	RESH Veto
7	Silicon Wafer trigger
8	2 muons in IM system
9	2 muons in OM system
10	1 IM muon, 1 OM muon
11	Hadron energy > ELOW
12	Hadron energy > EMED
13	Hadron energy > EHIGH
14	Eperp > EPLOW
15	Eperp > EPHIGH
16	1 charged track
17	2 charged tracks
18-20	Cuts on multiplicity
Others	Reserved for calibration

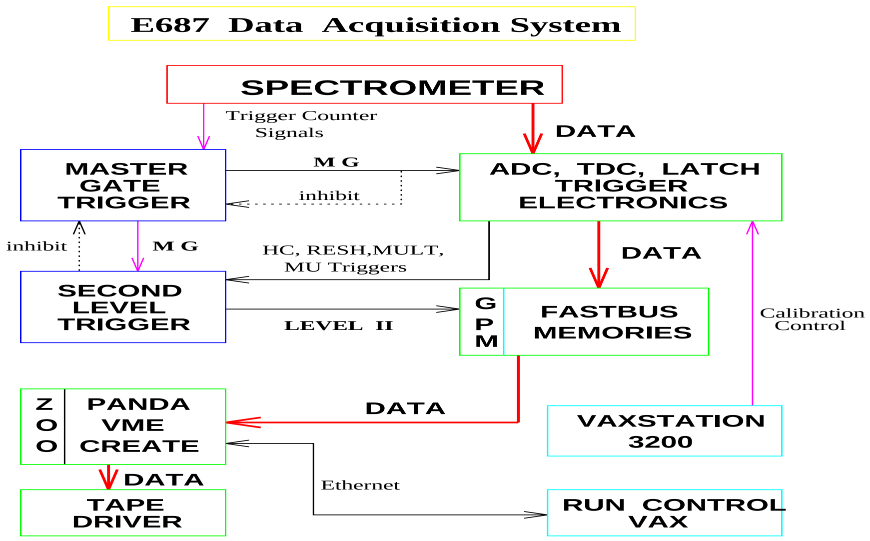

Figure 3.8: Schematic of E687 data acquisition system

and are stored in the memories. During the 40 second inter-spill time, data from the memories are then transferred to data tape. A total of four 8 mm tape drives may be written in parallel. Each tape can contain up to 2 GB of data corresponding to $\sim$ 500,000 E687 raw events.

Table 3.9: Average readout times for data streams.

Data stream	SSD	Latches	TDC	ADC(1)	ADC(2)
Read–out time (μs)	20	50	300–600	1000	1000

The E687 took data in two separate periods: May 1990 – September 1990 and July 1991 – January 1992. A total of about 280 million triggers in the first run period and about 240 million in the second run period were recorded to approximately 1,000 8mm tapes.

Chapter 4

Data Reconstruction

As a first stage of data analysis, we have to reconstruct raw data which contains the basic information of pulse heights, arrival time and hits from various detectors.

The E687 reconstruction process, called as PASS1, involves determining charged and neutral particle momentum and trajectories, identifying particle types, finding neutral vees, locating vertices, identifying electromagnetic showers and identifying muons.

In this chapter we describe the algorithms employed to reconstruct the raw data based upon information from the various detectors. Detailed description is paid to the Ξ^- reconstruction which is essential in this analysis. More detailed description of overall reconstruction processes can be found elsewhere[27].

4.1 Charged Particle Tracking

Charged tracks are reconstructed by using pattern recognition algorithms from the hits recorded in the SSD and MWPC detectors. Tracks are reconstructed separately in the two detectors, then linking algorithm combines information from these two detectors to look for matches.

4.1.1 SSD Track Reconstruction

In the first stage of the reconstruction, a very conservative analysis of the valid hits is performed on the basis of the released charge. A charged particle passing through a silicon plane deposits energy in the silicon planes.

The tracking algorithm is based upon finding two dimensional projections on the three separate views. Sharing of hits among different tracks is permitted except for one special case. Hits in the last three stations, already assigned to a track having hits on all four stations can not be used again to form a new track with only three hits. Projections are formed into tracks if they match in space and have a global χ^2 per degree of freedom (DOF) lower than 8. This process is performed in a fully symmetric way with respect to the i and j views, selecting only the best j and k association for each i projection and again only the best i and k association for each j projection. At this point, hits not associated with any tracks are used to search for wide angle tracks and for segments of highly multiple Coulomb scattered tracks. This search is performed by a direct match of hits in space. A track of this type is required to have at least six hits.

The overall track reconstruction efficiency is found to be 96% for simulated photoproduced $D\bar{D}$ events, and approaches 99% at momentum 10 GeV/c and retains a value of about 90% at 2.5 GeV/c . The relative percentage of spurious tracks is estimated to be $\sim 2.7\%$.

The resolution of a microstrip track is expressed as the transverse position error when the track is extrapolated to the center of target. The resolution for a track passing through the high resolution region of SSD has been calculated to be:

$$\sigma_x = 11\mu\mathrm{m}\sqrt{1+(\frac{17.5\ \mathrm{GeV/c}}{\mathrm{p}})^2}$$

$$\sigma_y = 7.7\mu\mathrm{m}\sqrt{1+(\frac{25.0\ \mathrm{GeV/c}}{\mathrm{p}})^2} \tag{4.1}$$

The largest contribution to the constant term is associated with microstrip granularity. MCS effects due to the target, the SSD, and the TR1 trigger counter are also included. The resolution is better in the Y coordinate than in X coordinate because all the three SSD views provide Y information, while only two of them give X information.

4.1.2 MWPC Track Reconstruction

Tracks are reconstructed from hits in the MWPC chambers by forming projections in each of the four chamber views. In the U, V, and Y (bend) views, projections are made using information from the MWPC alone. In the non-bend X view, hits are first formed from a seed from the SSD by searching for MWPC hits which match the SSD track extensions. Tracks are formed by matching all four projections. After all tracks originating from an SSD extension are found, unused hits in the X view are considered for reconstruction of new X projections. These projections are then matched to unused U, V, and Y projections to form additional tracks.

A least square fit is performed on all candidate tracks. The fit parameters are the intercepts and slopes of the track in the both X and Y views at the second analysis magnet (M2). A minimum χ^2/DOF is required for each track. Tracks were not permitted to have more than 4 missing hits among all the chambers, nor more than 2 missing hits in any single chamber.

After the main set of MWPC tracks is formed, the algorithm tries to recover track topologies which are previously missed. A microstrip extension routine is designed to recover these tracks. This routine extends microstrip tracks into the MWPC system by using the microstrip track parameters to predict X hits in the P0, P1, and P2. Only X hits which deviate from the predicted X positions by less than two wire spacing are used. Once X projection is found, unused U, V, and Y hits are used to form space points in the chambers. Tracks extending only to the P0 are required to have hits in all the four views, tracks extending to the P0 and

P1 may have one missing hit in each station. These new track are then fitted and MWPC track parameters are determined.

The efficiency of the MWPC tracking algorithm has been studied using a Monte Carlo simulation which models the efficiencies of the individual chamber planes. The efficiency has been determined to be better than 98% with less than 0.5% spurious tracks for tracks with momentum exceeding 5 GeV/c. Since events with extremely high multiplicity usually are resulted from chamber oscillation, an artificial limit of 30 tracks per event has been imposed in order to reduce reconstruction time.

4.1.3 Linking

Once tracks are reconstructed in both SSD and MWPC, linking of the MWPC track to the SSD track is one of the most important process in the data analysis. The primary purpose of linking is to provide the momentum for tracks passing through the microstrip detector which then pass through the first analysis magnet into spectrometer. Additionally unlinked microstrip tracks are available for use in reconstructing particles that decay downstream of the miscrostrip detector. For example, unlinked MWPC tracks are used as candidates for the neutral vees (K_s^0 and Λ) and long-lived hyperons (Σ, Ξ, Ω and so on) decay products.

The linking is accomplished by extending both SSD and MWPC tracks in opposite directions to the center of M1. The slopes and M1 intercepts of these two extensions are required to be consistent. A first pass with loose cuts is made to remove unreasonable links. Candidate links are subject to a global least square fit which uses all the SSD and MWPC hits associated with track. Multiple links are arbitrated based on the χ^2/DOF. A maximum of two MWPC tracks are allowed to be linked to the same microstrip track.

As shown in Figure 4.1, the linking efficiency is $\sim$ 94% for high momentum 3 chamber tracks and $\sim$ 98% for high momentum 5 chamber tracks. There is a signification reduction in effiency at low momentum due to multiple Coulomb

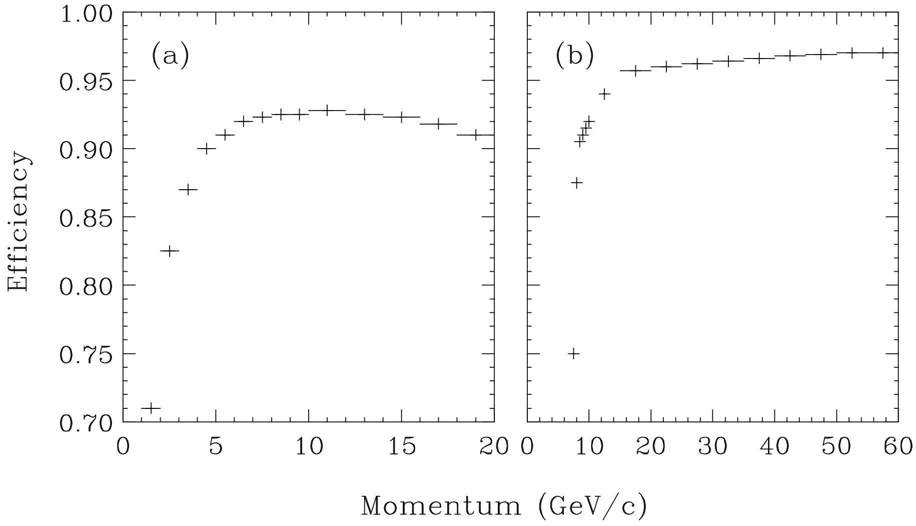

Figure 4.1: Linking efficiency between the SSD and MWPC tracks: (a) for 3–chamber tracks and (b) for 5–chamber tracks.

scattering.

4.2 Vertices Reconstruction

The Stand alone vertex algorithm uses the microstrip tracks to determine the complete vertex topology of the event. As a first stage, the vertexing algorithm assigns all the tracks to a common vertex. A least square fit is accomplished to compute χ^2:

$$\chi^2 = \sum_{i=1}^{n} \left(\frac{x - (x_i + a_i z)}{\sigma_x^i} \right)^2 + \left(\frac{y - (y_i + b_i z)}{\sigma_y^i} \right)^2$$

where $(x,\ y,\ z)$ is the vertex coordinates (which are the fit parameters), a_i, b_i, x_i, and y_i are the slopes and intercepts of the ith track, and, σ_x^i and σ_y^i are the errors associated with the SSD track parameters. The tracks giving the largest χ^2 contribution are removed from this vertex, until the χ^2 of the vertex is smaller than the specified value. This procedure is iterated until all possible vertices are found.

The vertexing algorithm assigns all SSD tracks to a common vertex. In successive phases, only tracks not previously included in a vertex are considered. Each time a vertex is found, the program tries to add to the same vertex other tracks which could have been erroneously disregarded or simply not considered since they were already assigned to another vertex. At the end of the procedure, a complete SSD vertex topology of the event is constructed and each SSD track is either definitely assigned to a specific vertex or remains unassigned. The most upstream SSD vertex is selected as the primary vertex in the event and is referenced by some other reconstruction procedures. If no SSD vertex in a particular event is found, the center of the target is considered as the primary vertex.

4.3 Momentum Determination

Charged particle momentum is determined by measuring the deflection of the particle in a magnetic field. The various topologies of tracks require different techniques to measure a particle momentum. For a 5-chamber track, which passes through the second analysis magnet, the track parameters of upstream and downstream of M2 are fit to determine the particle momentum. An iterative least square fits are performed until the track parameters are stabilized.

For a 3 or 4 chamber linked track, the particle momentum is determined from deflection through M1 using downstream MWPC track parameters and microstrip linked track parameters. For a unlinked 3 chamber track, we assume that the particle was created at one of the vertices previous reconstructed. The X projection of the track is traced to upstream to the target and the closest vertex is chosen as the particle production point. If no vertex is match, we assume the particle is created at the center of target.

The momentum resolution of the charged particles using M1 is:

$$\frac{\sigma_{\mathrm{p}}}{\mathrm{p}} = 1.4\% \; (\frac{\mathrm{p}}{100\ \mathrm{GeV/c}}) \sqrt{1 + (\frac{23\ \mathrm{GeV/c}}{\mathrm{p}})^2} \tag{4.2}$$

For 5-chamber tracks measured by M2, the momentum resolution is given by:

$$\frac{\sigma_{\mathrm{p}}}{\mathrm{p}} = 3.4\% \; (\frac{\mathrm{p}}{100\ \mathrm{GeV/c}}) \sqrt{1 + (\frac{17\ \mathrm{GeV/c}}{\mathrm{p}})^2} \tag{4.3}$$

The momentum dependent term is due to multiple Coulomb scattering which contributes to resolution dominantly at low momentum.

4.4 Particle Identification

The charged particle identification is mainly made with three Čerenkov counters. Electron and muon identifications which are important in this analysis are provided by using shower information of electromagnetic calorimeter and using hit information of muon counters.

4.4.1 Čerenkov Identification

The Čerenkov algorithm uses the light patterns observed in the three Čerenkov counters for a given particle hypothesis and momentum. The algorithm categorizes each charged track as either electron, pion, kaon, or proton. These 4 particles, which comprise the majority of all tracks emitting Čerenkov radiation in the experiment, have different threshold momenta at which they begin to radiate. More detailed description is given in section 3.2.4.

The algorithm begins by first setting up an *on/off* code for each cell in each detector. This is determined by the presence or absence of a phototube pulse height above a threshold value. Using the track momentum and threshold in a given counter, an anticipated light yield based on photoelectron calibration of the counters is calculated for each particle hypothesis. The comparison of the actual and anticipated responses is made for each of three Čerenkov counters (the C3 response is only applicable for 5–chamber tracks). Each track is assigned a particular Čerenkov classification describing the possible particle hypothesis using combined information from the counters. The possible particle identification codes are listed in Table 4.1.

The expected Čerenkov radiation cones for different particles may overlap which is causing confusion regarding the status of a given cell. If there are no unshared cells for a given track and the shared cells detected Čerenkov light, the Čerenkov algorithm returns a *confused* status. Counters with a *confused* status are not included in making decisions. A small amount of confusion is accepted which biases the status towards *on*. This bias creates an efficiency loss for heavy particles (kaons and protons) but also decreases the number of π's and μ's misidentified as kaons or protons.

The Čerenkov detection efficiency has been obtained to be $\sim 75\%$ for kaons and $\sim 80\%$ for protons. A very detailed Monte Carlo study for the Čerenkov system has been performed and reproduced a satisfactory agreement with the studies of the data.

4.4.2 Inner Electromagnetic Calorimeter Showers

There are two primary applications of electromagnetic calorimetry, photon reconstruction and electron/hadron discrimination. The IE shower reconstruction algorithm relies heavily upon a discriminant analysis to distinguish between electromagnetic and hadronic showers. Data from both the electron calibration and the pion calibration runs are used as training samples for a discriminant analysis, more detail description can be found elsewhere [24].

Showers which deposit energy only in the middle module are automatically la-

Table 4.1: ISTATP codes.

ISTATP	Particle Identification
0	inconsistent
1	e definite
2	π definite
3	e/π ambiguous
4	K definite
6	π/K ambiguous
7	$e/\pi/K$ ambiguous
8	p definite
12	K/p ambiguous
14	$\pi/K/p$ ambiguous
15	total confusions

beled as electromagnetic showers, and those showers beginning in the farthest downstream module are identified as hadronic showers.

The reconstruction efficiency for calibration electrons is about 90%, while the identification effiency for electron pairs ($\gamma \to e^+e^-$) in data is significantly lower, about 62%. This is due to shower activity and pattern recognition.

All showers which are not associated with charged tracks are identified as neutral showers and subject to a separate discriminant analysis to separate photons from hadrons. The training samples for the neutral discriminant analysis are electrons and pions of calibration runs. The input variables are identical to those used in the charged particle analysis except for E/p. After photons have been identified they are used to reconstruct the decay $\pi^0 \to \gamma\gamma$.

4.4.3 Muon Identification

The muon identification is accomplished by projecting MWPC tracks onto inner muon system and by searching a 3σ scattering radius for hits in the detectors of the inner muon system. If more than one match is found in a proportional tube plane for a track, the closest hit is kept for later reference.

If a track has matched 5 or more planes out of a possible 7, we consider it a muon and we assign it a code shown in Table 4.2 based on its shared hit history. In practice, if IDMU $\neq 0$, we call the track as a muon.

Table 4.2: MUON identification codes

Code (IDMU)	Meaning
4	3 shared hits, 4 unshared hits
3	2 shared hits, $>$ 2 unshared hits
2	1 shared hits, $>$ 1 unshared hits
1	0 shared hits, Muon definite
0	Not a Muon
-1	1 shared hits, $\leq$ 1 unshared hits
-2	2 shared hits, $\leq$ 2 unshared hits
-3	$>$ 2 shared, hits $<$ 4 unshared hits

The muon particles below 30 GeV/c , some particles do not reach the second bank. It is possible to have muons that penetrate only to the first bank of the inner muon system or that have scattered outside the 3 σ search zone by the time they reach the second bank. This is due to energy loss in the absorption material. The identification requirements for a particle below 30 GeV/c were relaxed so that a previously lost muon could be recovered if it matched 3 or 4 planes in the first bank. More detail descriptions can be found in reference [25].

Sometimes, the number of hits in the inner muon system is large. If there are more than 20 hits in any single plane of the muon system, we drop all the hits from that particular plane. While this is not a problem in the original configuration, we find that a lost plane occurs for about 5% of events in the 1991 data where a muon is present. Figure 4.2 is a single track efficiency expected for the 1990 inner muon system using the simulated data.

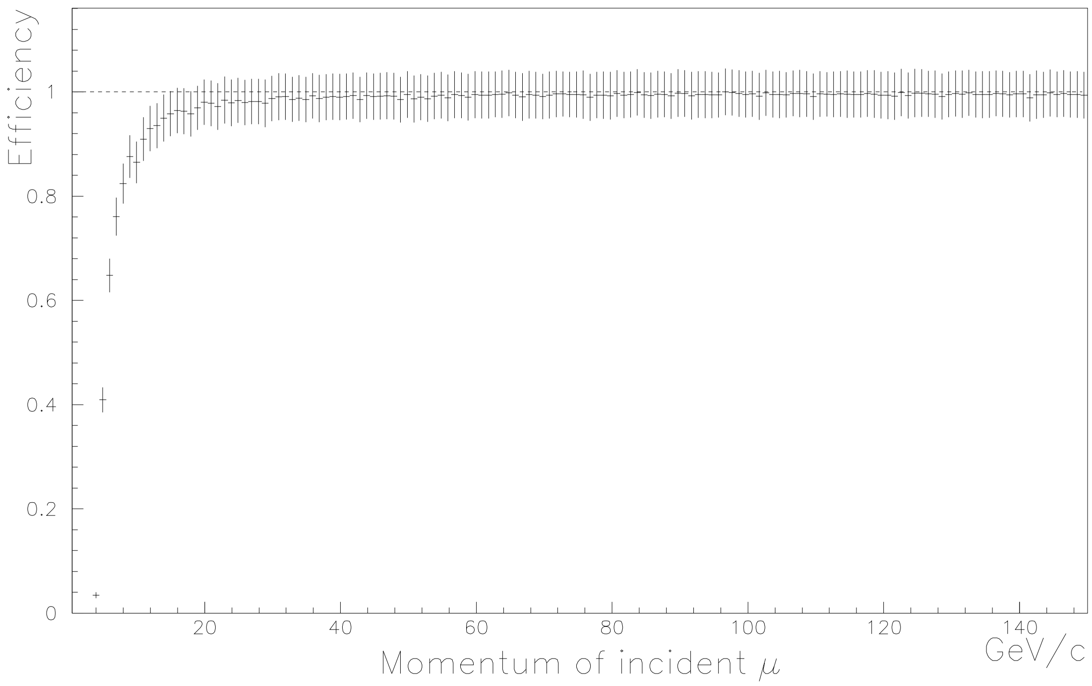

Figure 4.2: Expected efficiency vs muon momentum for the 1990 muon system.

4.5 Neutral Vees

The neutral vees, K_s^0 and Λ are often found among the decay products of the charmed hadrons. In E687, these particles are reconstructed through the charged decay modes:

$$K_s^0 \longrightarrow \pi^+\pi^- \qquad (\mathrm{BR} = 68.6\%)$$
$$\Lambda \longrightarrow p\pi^- \qquad (\mathrm{BR} = 63.9\%)$$

These particles have long lifetimes relatively to charm particles, and may travel several meters within the spectrometer before decaying. According to the decay region, as shown in Figure 4.3, vees are categorized: 'SSD vees' which decay upstream of the microvertex detector; 'MIC vees' which decay inside microvertex detector; 'M1 vees' which decay between the last station of SSD and the first MWPC station, P0; 'Reconstruction vees' which decay between P0 and P2. A total of about 10 m of decay length is covered. Despite the diversity of the possible topologies, vee reconstruction algorithm essentially seeks pairs of oppositely charged tracks which form a common vertex. The invariant mass of the pair tracks are calculated with assigning both charged tracks pion masses to form K_s^0 hypothesis. Similarly each candidate vee is formed as a Λ by forming invariant mass assigning the higher momentum track a proton mass and the softer track a pion mass. Each vee has two invariant masses for K_s^0 and Λ hypothesis, respectively. It has to be carefully handled in the data analysis because a *true* K_s^0 may also be accepted as a Λ or vice versa. No Čerenkov identification is required at this stage.

Figure 4.4 shows the vee invariant mass distributions of the K_s^0 hypothesis for different vee categories. Note that K_s^0 mass distributions shown in Figure 4.4 do not represent the whole E687 data sample but are representative of the overall data quality. The invariant mass plots of the Λ hypothesis are shown in Figure 4.5 for different vee types. The Λ mass distributions are obtained from the entire E687 data sample with the requirements discussed in Section 4.8.

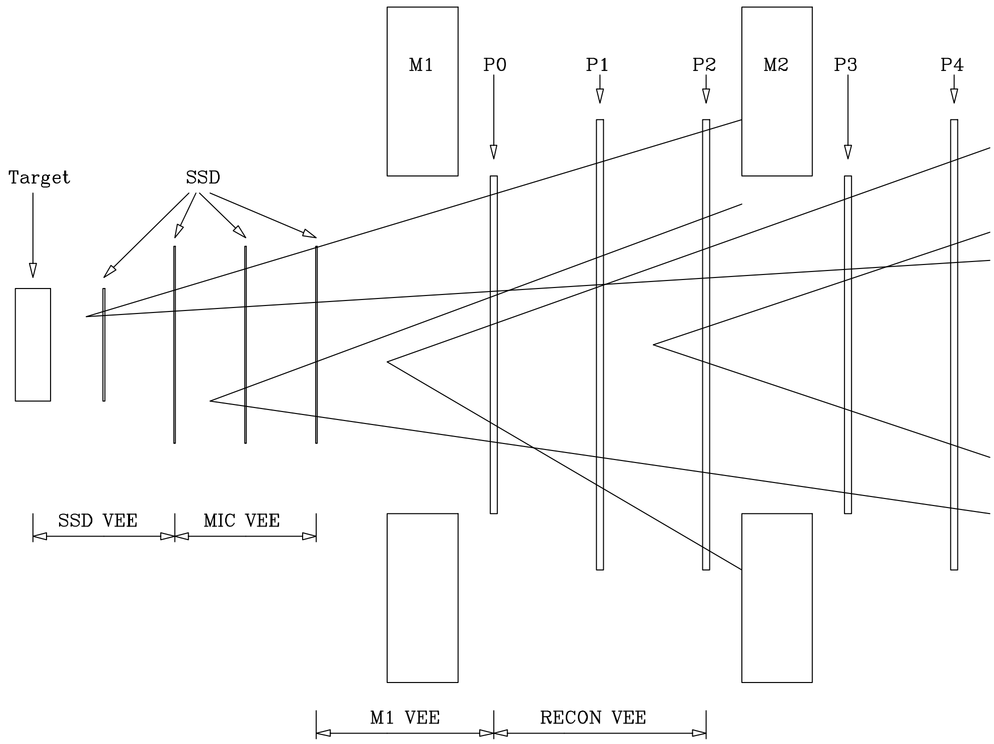

Figure 4.3: Schematic drawing of regions where vees are reconstructed with different algorithms.

4.5.1 SSD Vees

SSD vees are reconstructed from all pairs of oppositely charged SSD tracks which are linked to MWPC tracks from a common vertex. The vee vertex is required to be at least $20\sigma_z$ downstream of the primary vertex (σ_z is the error calculated for the distance between the primary and vee vertices) and the vee momentum must point back to the primary vertex within 1 mm in the transverse plane to reduce the combinatoric background. Although the decay volume for this topology is small, about 10 cm in Z, the SSD vees are important because the track vector of the SSD vee has resolution comparable to that of an SSD track.

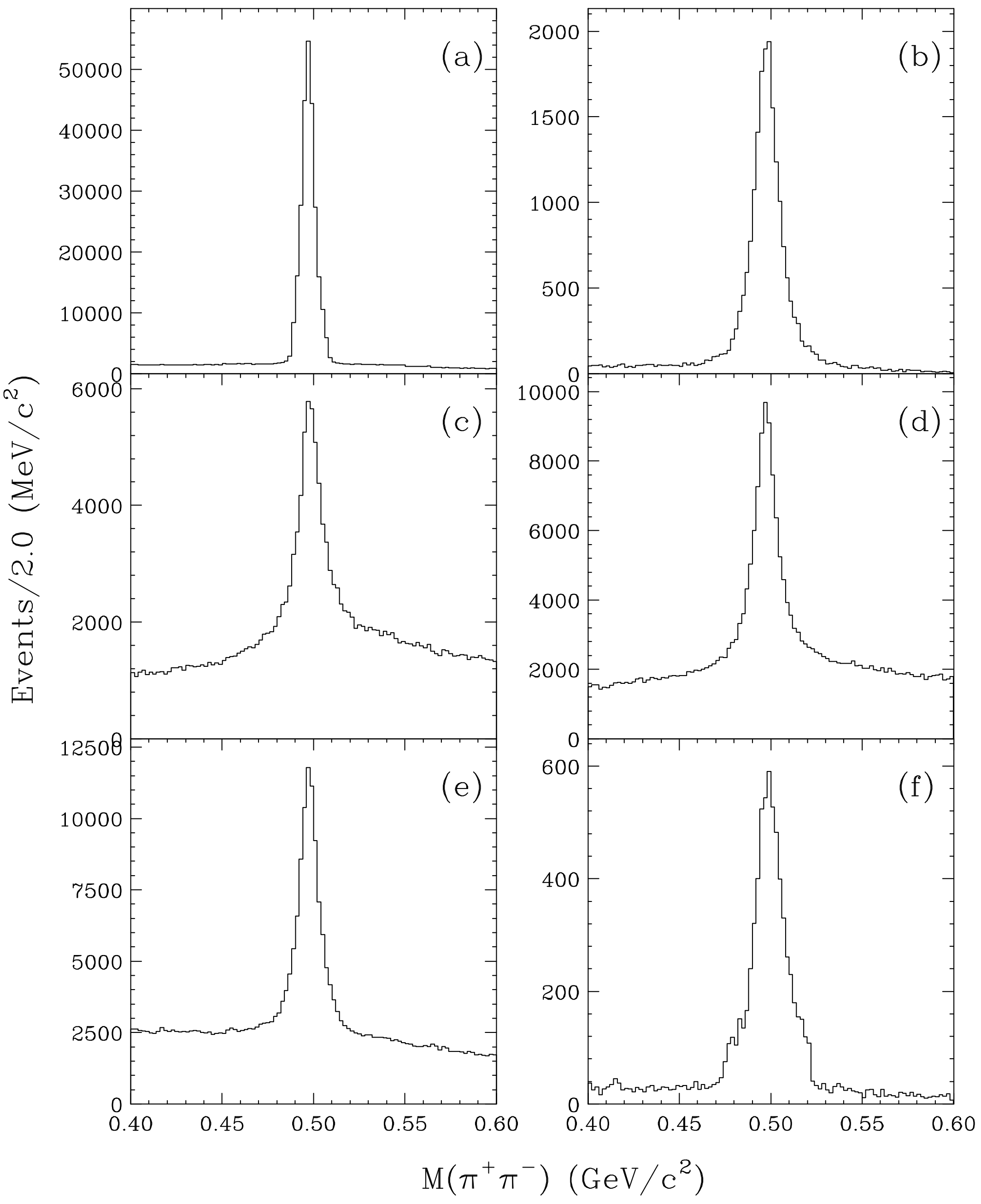

Figure 4.4: Vee invariant mass plots for the K_s^0 hypothesis: (a) SSD vees, (b) MIC vees, (c) Stub–Stub vees, (d) Track–Stub vees, (e) Track–Track vees, and (f) RECON vees.

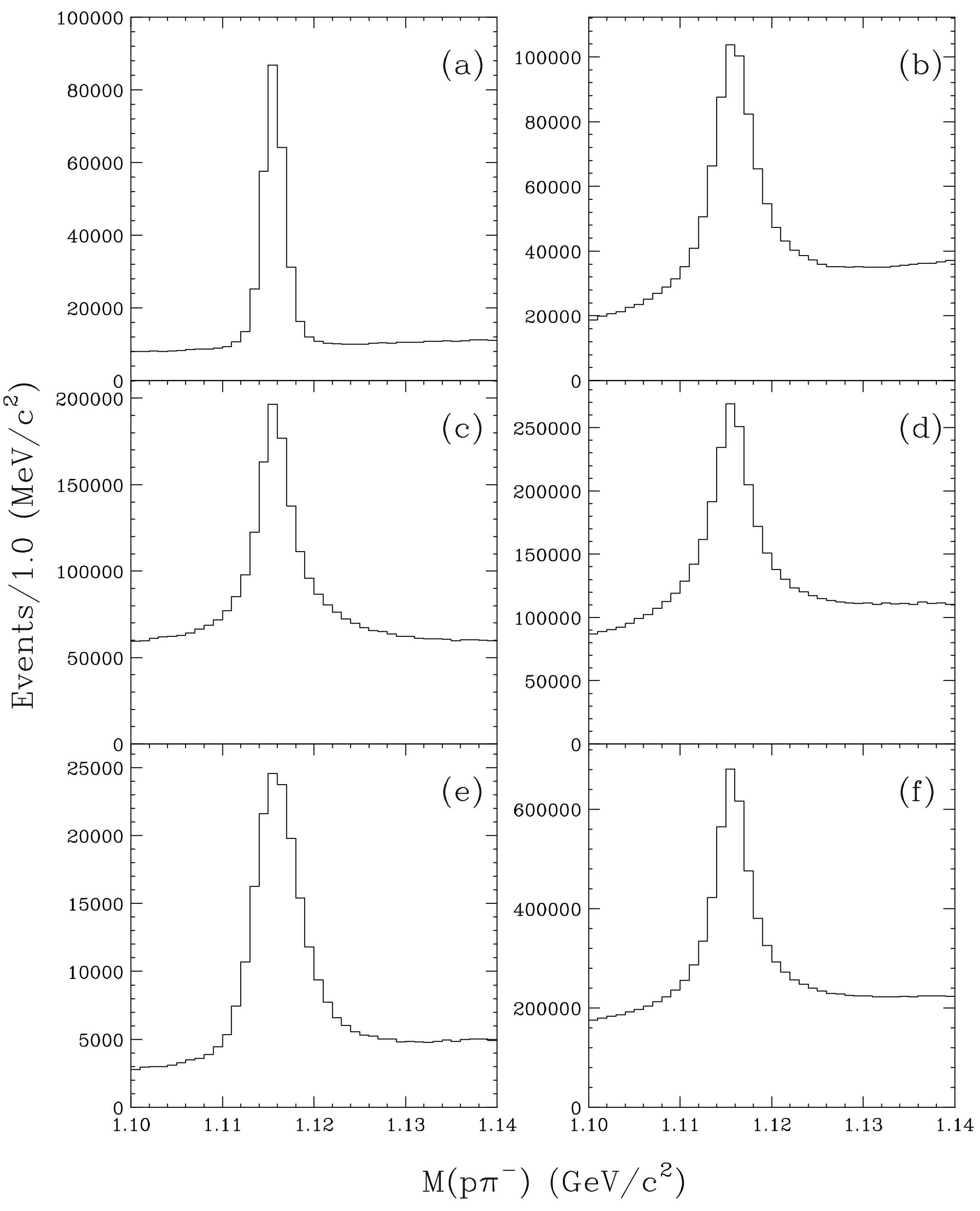

Figure 4.5: Vee invariant mass plots for the Λ hypothesis: (a) SSD vees, (b) Stub–Stub vees, (c) Track–Track vees, (d) Track–Stub vees, (e) RECON vees, and (f) All vees.

4.5.2 MIC Vees

The MIC vee which decays somewhere between the second and last stations of microvertex detector. This region is 18 cm in length and contains about 10% of the observed K_s^0 decays. The MIC vee algorithm begins by extrapolating unlinked MWPC tracks into the last SSD station and forming triplets from unused hits in the station. The transverse distance between each triplet and the extrapolated MWPC track under consideration is computed. If a triplet is found such that this distance is smaller than a certain value, the SSD hits are included in a global refit to the MWPC track parameters and the track is extrapolated back to the next station. At this stage, each MWPC track may have several triplets associated with it in the last SSD station. Now a search is made for triplets in the third SSD station, which match with the track, in the same manner with the previous search. The triplets, or pairs of triplets, associated with a single MWPC track are arbitrated on the basis of χ^2 from a global fit to all hits associated with each candidate.

All combinations of oppositely charged candidate tracks are paired together and the distance of closest approach (DCA) is computed for each. Only pairs with a reasonably small DCA are kept. If more than one pair contain the same candidate track, only the one with the minimum DCA is retained.

4.5.3 M1 Region Vees

The majority of vees are reconstructed in the M1 region, which covers the area between the last SSD station and the first MWPC station. The M1 region vees are reconstructed using unlinked MWPC tracks. There are three topologies: *track–track* vees, consisting of two 5–chamber tracks; *track–stub* vees, consisting of one 5–chamber track and one 3–chamber track; *stub–stub* vees, consisting of two 3–chamber tracks.

The basic idea of the algorithm is the same for all three topologies. For the candidate pair of unlinked MWPC tracks, the X and Z locations of a vee decay vertex are first estimated by intersecting the two daughter tracks in the X-view (non-bend). An iterative procedure then traces the two tracks through the M1 field to determine the Y position of the vee vertex. In the case of the track–stub vee, the procedure also determines unknown momentum of the 3–chamber track. The stub–stub vee is required an additional constraint that the vee is originated from the primary vertex.

The special reconstruction routine is implemented to recover lost vees for $\Xi^- \to \Lambda\pi^-$, $\Omega^- \to \Lambda K^-$, and $\Sigma^+ \to p\pi^0$. The *track–track 1–link* and *track–stub 1–link* vee algorithms are identical to the track–track and track–stub algorithms, respectively, except that one of vee daughter tracks is allowed to be linked (in any case the 5–chamber track is allowed to be linked). A few additional cuts are applied to remove the background of true linked tracks. For the *track–track 1–link* vees the two momenta (using M1 and M2) are required to disagree by at least 5σ and by at least 3σ for the *track–stub 1–link* vees (σ is an error on the momentum difference). The higher momentum daughter track is required to be identified by Čerenkov detector as being a *heavy* (ISTATP > 7). Since a negligible amount of K_s^0 falls into this topology, no attempt is made to reconstruct 1–link vees for the K_s^0 hypothesis.

4.5.4 Recon Vees

Reconstruction vees decay in the region of the spectrometer between P0 and P2. The highest momentum vees tend to be reconstructed in this category because they are more likely to decay in the downstream of P0.

Recon vee algorithm has to reconstruct the daughter tracks using only unused hits before a vee search is performed because the MWPC tracking algorithm does not attempt to reconstruct track which does not have any hit in P0.

The reconstruction vee search proceeds as follows. The program first looks for vees decaying between P0 and P1, then for vees between P1 and P2. Each program employs the same flow logic. Single track projections are found in the non-bend

X-view. The X hits are matched up with U, V, and Y hits to form track candidates and single track fits are performed. At least three hits are required to be found in each chamber. A loose χ^2 cut is made on the single track fits. Finally the oppositely charged tracks are paired to make vee candidates and a least square fit is performed. The vertex position is included in the fit along with the track hits. Candidates with acceptable fits are sent to an arbitration algorithm which insures that no X-projection is used in more than one vee.

The vees which decay between P1 and P2 where the decay tracks exit before passing through P4 are handled separately. These tracks are subjected to an additional constraint that they originate at the primary interaction vertex and the transverse momenta of the tracks about this direction are required to be balance.

4.6 Kinks

The term *kink* refers to a decay where a long–lived charged particle passes through the SSD and then decays into a charged particle and a neutral particle. The E687 kink algorithm has been used to reconstruct three following decays.

$$\begin{aligned}
&\Sigma^+ \longrightarrow p\pi^0 \quad (\mathrm{BR} = 51.6\%),\\
&\Sigma^+ \longrightarrow n\pi^+ \quad (\mathrm{BR} = 48.3\%),\\
&\Sigma^- \longrightarrow n\pi^- \quad (\mathrm{BR} = 100\%),
\end{aligned}$$

The kink algorithm begins by looping over all unlinked SSD tracks pointing into the M1 aperture and pairing it with each unlinked MWPC track. Vee candidate tracks are not considered as possible kinks. The X–projection of unlinked MWPC tracks are extrapolated upstream to determine whether they intersect with an unlinked SSD track. This provides a rough estimate of the X and Z positions which are required to be between the last SSD station and the first MWPC station.

If the track passes through both magnets, its momentum is measured by M2 and hence we can estimate the Y position by tracing it through the M1 field to initially determined Z position. If the Z position is upstream of M1, the Y distance between the traced 5–chamber track and the SSD track at this Z position is required to be less than 2.5 cm. The parent momentum can only be calculated by making a particular decay hypothesis and solving the kinematic equations. This involves assuming the parent and daughter masses and balancing the momentum transverse to the parent direction. This introduces a two-fold ambiguity in the parent momentum. If both momenta are physical, they are both recorded for the later analysis. However, if the kink Z position is within M1 magnetic field, the ambiguity can be resolved. The MWPC track is traced upstream to the Z position of the kink. The X and Y positions of the kink are then found at the Z position. The SSD track is then traced downstream through the M1 field to the Z position, with different trial momenta, until a momentum is found which best traces the SSD track to the kink vertex. For 3–chamber MWPC tracks, only upstream of M1 kink position is considered. The X and Y positions of the microstrip track at the previously estimated kink Z positions are used as the kink vertex location.

All kinks are reconstructed according to all three decay topologies mentioned above. Some decay topologies are discarded on the basis of particle identification of the charged daughter. A new charged particle identification is made by re–running the Čerenkov analysis routine with the momentum determined by the kink algorithm.

4.7 Ξ^-/Ω^- Reconstruction

The Ξ^- and Ω^- hyperons, so called as *cascades* are commonly found in the charmed baryon decays, and which are crucial in reconstruction of many charmed baryon signals. Those hyperons are reconstructed in E687 Pass1 with their decay modes:

$$\Xi^- \longrightarrow \Lambda\pi^- \qquad (\mathrm{BR} = 100\%),$$
$$\Omega^- \longrightarrow \Lambda K^- \qquad (\mathrm{BR} = 67.8\%),$$

respectively, using the Λ reconstructed by the vee algorithms. In E687 experiment, the cascade decays are classified into two categories: *type–1* (or *upstream*) Ξ^-'s and Ω^-'s which are decaying upstream of the SSD and *type–2* (or *downstream*) hyperons which are decaying downstream of the microvertex detector.

Two separate algorithms have been used to reconstruct the relevant decay topologies [26]. Both algorithms use a common set of requirements to select the Λ. In all cases, the vee daughter track with a higher momentum is considered as a proton and the Čerenkov algorithm is re-run using the momenta of the vee daughter tracks as determined by the vee algorithm. The requirements for each vee type are given below.

- SSD vees:
  1. Mass of the Λ must be within 8 MeV$/c^2$ of the nominal mass.
  2. Čerenkov requirements for the proton track:
     - ISTATP = 8, 12, or 14 if the momentum (p) is less than 20 GeV$/c$;
     - ISTATP = 8 or 12 if 20 GeV$/c < p <$ 110 GeV$/c$;
     - ISTATP = 8, 12, 14, or 15 if 20 GeV$/c < p <$ 110 GeV$/c$.
  3. Neither vee SSD track is allowed to be linked to two MWPC tracks and the pulse height from the silicon strip for each SSD track must be consistent with a single ionizing particle. Both requirements are used to reject e^+e^- tracks.
- MIC vees:
  1. Mass of the Λ must be within 8 MeV$/c^2$ of the nominal mass.
- Track–Stub and Stub–Stub vees:

1. Mass of the Λ must be within 15 MeV/c^2 of the nominal mass.
2. Same Čerenkov requirements for the proton track as in item 2 of SSD vees.
3. Čerenkov requirements for the pion track:
   - ISTATP > 1

- Track–Track vees:

1. Same requirements as for items 1–3 of Track–Stub and Stub–Stub vees.
2. Distance of closest approach between vee daughter tracks must be less than 5 mm.

- 1–link and Recon vees:

1. Mass of the Λ must be within 15 MeV/c^2 of the nominal mass.

The reconstruction effieiency for Λ which originate from Ξ^- is calculated from a Monte Carlo study. The overall Λ reconstruction efficiency is 41 % using the requirements described above.

4.7.1 Upstream Ξ^-/Ω^-

Upstream Ξ^-/Ω^- are those which decay upstream of the first microstrip station. The reconstruction algorithm is very simple, in principle. Linked MWPC tracks are paired with each Λ candidate which satisfies the requirements outlined above. The decay vertex of the Ξ^-/Ω^- candidate is reconstructed by intersecting the Λ momentum vector and the MWPC track and demanding the confidence level of the vertex to be greater than 1%, and the candidate be consistent with coming from a vertex further upstream such as the primary vertex. The MWPC track is assigned a pion mass to obtain the invariant mass for the Ξ^- hypothesis and is assigned a kaon mass for the Ω^- hypothesis. The candidate is accepted if $\Lambda\pi^-$ invariant mass is less than 1.4 GeV/c^2 or ΛK^- invariant mass is less than 1.725 GeV/c^2 . Two additional requirements are applied for each candidate in order to improve the signal–to–noise (S/N) ratio. The *significance of separation* between the Ξ^-/Ω^- decay vertex and its production vertex is calculated as the quantity L/σ_L, where L is the distance between two vertices and σ_L is the error on L. The algorithm requires $L/\sigma_L > 0$. The *isolation* of the Ξ^-/Ω^- decay vertex can be tested by attempting to place other tracks in the vertex and re–fitting it. A cleaner sample is obtained by requiring that the confidence level (CL2) from the fit to the new vertex is required to be less than a certain value.

The invariant mass plots for the Ξ^- and Ω^- hypotheses are shown in Figure 4.6. A cut of $L/\sigma_L > 0$ and CL2 < 0.1 is required, along with the requirement that for the Ω^- hypothesis the daughter track is identified by the Čerenkov counters as being a kaon consistent. These plots are from the full E687 data sample.

The reconstruction efficiency of this algorithm has been studied using Monte Carlo simulation and found to be about 20% for both decays without including geometrical acceptance and the branching fractions introduced in the decay modes.

4.7.2 Downstream Ξ^-/Ω^-

Downstream Ξ^-/Ω^- is reconstructed between the last SSD station and the first MWPC plane (P0). This decay volume consists of more than three meters in the beam direction. A very important advantage to these decays is that the Ξ^-/Ω^- leaves a track in the SSD before decaying, which will become more apparent in the charmed baryon analysis.

The algorithm begins by pairing each Λ with every unlinked MWPC track in a given event. A putative cascade decay vertex is determined by intersecting a Λ momentum vector and a charged daughter track. If the vertex is found to be downstream of P0 or more than 50 cm upstream of the target, the combination is rejected. At this point the charged daughter track is traced through M1 to the

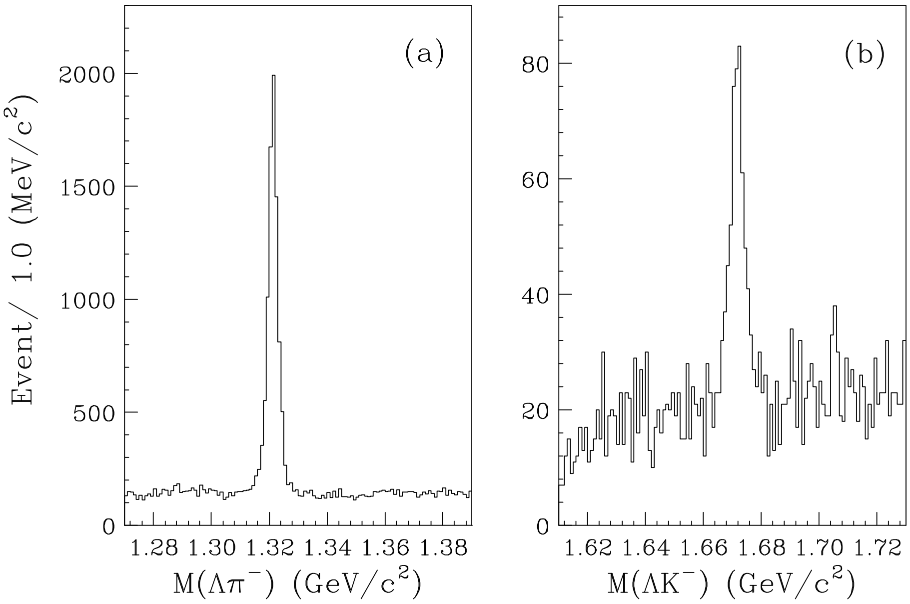

Figure 4.6: $\Lambda\pi^-$ and ΛK^- invariant mass distributions for the Ξ^- and Ω^- candidates decaying upstream of the SSD a) for the Ξ^- candidates and b) Ω^- candidates.

putative vertex. For a 3–chamber track, 5 times iterative procedure is used to determine its new track parameters until the Z of the vertex changes by less than 3 mm from one iteration of the next. A new vertex Z location is determined as the point where the distance of closest approach of the Λ vector and the track occurs. The track is traced to the new vertex and the track parameters are updated.

Unlinked SSD tracks are looped over and an attempt is made to match each one with the vector sum of the Λ momentum and the charged MWPC track. If the Λ under consideration is of the 1–link category then the SSD track which is linked to one of the Λ daughters is also considered in this step. Each SSD track is traced downstream to the putative cascade vertex determined in the previous step; if the vertex is within M1 field the magnetic tracing procedure is employed, else the SSD track is simply extrapolated to the vertex. A better Z position of the vertex is now determined as the Z position where the SSD track and MWPC track make their closest approach because the SSD track has much better position resolution than does the Λ. If the Z position is located downstream of P0 or upstream of the target, the SSD track is rejected as a candidate. In addition, the Ξ^-/Ω^- vertex is required to be upstream of Λ vertex.

To remove spurious matches a cut is placed on two quantities. The candidate vertex has been defined in two way: the space point where a Λ and a MWPC track make their closest approach, and the point where an SSD track and the MWPC track make their closest approach. The transverse distance (*i.e.* in the X–Y plane) between these putative vertices is defined as CASIMP and is required to be within a certain value. The second quantity on which a cut is made is the difference between the X and Y slopes of the SSD track and the slopes given by the sum of the Λ and MWPC track momentum vectors. The ANGLX and ANGLY, defined as the X slope difference and Y slope difference, respectively, are required to be less than a certain values. Candidates sharing the same Λ and MWPC track but using different SSD tracks are arbitrated on the basis of the CASIMP quantity. Monte Carlo studies show that this arbitration is almost 99% efficient. Finally, the MWPC track is assigned a pion mass for the Ξ^- hypothesis and is assigned a kaon mass for the Ω^- hypothesis. The candidate is accepted if $\Lambda\pi^-$ invariant mass is less than 1.4 GeV/c^2 or ΛK^- invariant mass is less than 1.725 GeV/c^2. The invariant mass plots for the Ξ^- and Ω^- are shown in Figure 4.7.

The overall reconstruction efficiency has been estimated by Monte Carlo study to be about 20% reflecting the 12% of the Ξ^- and 4.5% of the Ω^- which are not in the geometrical acceptance of the algorithm (decay downstream of P0).

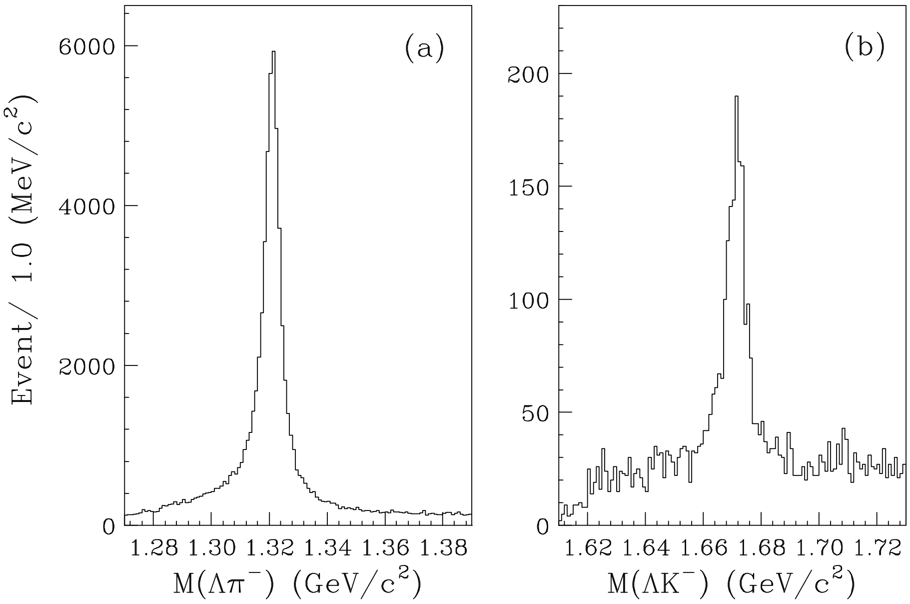

Figure 4.7: $\Lambda\pi^-$ and ΛK^- invariant mass distributions for the Ξ^- and Ω^- candidates decaying downstream of the SSD a) for the Ξ^- candidates and b) Ω^- candidates.

4.8 Data Reduction

The reconstruction algorithms are combined into a single package and the raw information is processed to produce the reconstructed information described in the preceding sections of this chapter. The date reconstruction process (PASS1) is very CPU intensive, and has been performed during the period from November 1991 to August 1992 using IBM and SGI computer farms at Fermilab. About 1,000 raw 8 mm data tapes were processed to roughly 2,000 reconstructed 8 mm data tapes.

The reconstructed data are further reduced by *skimming* for further data analysis. The data were skimmed from May 1992 to September 1992 and contain about 40 % of the full data set. A total of 30 skim sets, as shown in Table 4.3 were used for physics analysis.

In this analysis the skims we use is the cascade skim. This skims are performed at the University of Colorado at Boulder. Events containing at least one Ξ^- or Ω^-, which was successfully reconstructed with the given requirements, have been skimmed from the full data set. This data sample consists of $\sim 500,000$ events, about 0.1% of the original sample of 520 million raw events.

Table 4.3: List of skimbit sets

Skim bit	Skim category
1	Semileptonic skim
2	1% of all events
3	Prescale Unbiased Data
4	e^+e^- pair trigger
5	Two Vertex Skim
7	Ξ^-/Ω^- skim
8	K_S^0 skim
9	D meson skim
10	D skim (D^* flag set)
11	D skim (Golden Mode flag)
13	Λ skim
14	Kink ($\Sigma^\pm$) skim
15	Charm baryon skim ($pK+X$)
16	$\Lambda_C^+ \rightarrow pK^-\pi^+$ skim
17	Leptonic skim
18	μ skim for J/ψ
19	Diffractive skim
25	Kaon lepton skim
26	Kaon ID skim
27	Kaon linking skim
28	ϕ meson skim

Chapter 5

Analysis Tools

In this chapter, we will describe the analysis tools on which most E687 physics analysis are based. The vertex finding algorithm used in reconstruction of charm production and decay vertiecs is described. The E687 Monte Carlo simulation which is an essential tool for understanding of the overall performance of the detector and the reconstruction and analysis routines. A detailed study of the lepton (electron or muon) misidentification is discussed.

5.1 Candidate Driven Vertex Algorithm

A common characteristic of the events containing charm quarks is the presence of separated production and decay vertices. Non-charm hadronic events in E687 contains only one vertex. So, the ability to reconstruct the production and decay vertices and to separate them are essential to isolate the charm signal from the background. The high resolving power of the microstrip detector in E687 makes this separation possible.

In E687, there are two separate vertex finding algorithms. Those are the Stand alone vertexing algorithm and the candidate driven vertexing algorithm. The stand alone algorithm is described in section 4.2. This technique is able to pick up decays with missing neutral particles, e.q. ν or π^0. No biases are introduced into initial selection of candidates. The vertexing algorithm commonly used in E687 data analysis is the candidate driven vertex algorithm. The basic idea of the candidate driven vertex algorithm is to use a charm candidate as a seed to find the primary vertex.

5.1.1 Vertex Reconstruction

A combination of tracks consistent with a given charm decay mode is selected. The candidate tracks which form the charm particle are then fitted to the hypothesis of a common vertex. If they conform to this hypothesis with a confidence level greater than a specified minimum value, typically 0.01, then the cluster is accepted as a charm candidate. The full covariance matrices of each track comprising the candidate are used to generate a charm track.

Once a charm vertex is searched, then the primary vertex is constructed by using the charm track and all other SSD tracks in the event. First, the searched charm track is fitted to a common vertex with all other SSD tracks one at a time. All tracks which form a vertex with the confidence level greater then a cut value (typically 1%) are selected and put into an object list.

The tracks in the list are combined pairwise with the candidate charm track and then are fit to a common vertex hypothesis. The pair with the best confidence level is accepted as a candidate primary vertex. The search terminates when no track is left with the confidence level is greater than a cut value for coming from this vertex.

In addition to fits of the primary and secondary vertices, a global fit is applied to the decay tracks to find the decay length, L. The quantity L/σ, where σ is the calculated uncertainty in L, is then an unbiased measure of the significance of detachment of the secondary vertex from the primary vertex.

5.1.2 Vertex Isolation

Once the primary and decay vertices are reconstructed, an effective way of improving signal to noise is to require the vertices be isolated.

We check whether the charm daughter tracks are compatible with coming from the primary vertex. The daughter tracks are added to primary vertex, then the global fit for the primary vertex is performed. The highest confidence level(ISO1) of the new object is obtained. This cut is designed to reject an event where one or more tracks from the primary vertex are accidentally assigned to a lower multiplicity charm decay vertex or combined with other tracks to form a fake vertex.

If there are any leftover tracks not assigned to the charm and primary vertices, we check whether any of these leftover tracks are compatible with originating from the secondary vertex. These tracks are added to the charm vertex and the highest confidence level(ISO2) of the new object is required to be less than a cut value. This cut is applied to reduce the backgrounds where we have additional charged tracks in the vertex.

5.2 Monte Carlo Simulation

The E687 Monte Carlo simulation is divided into two packages, the event generation package and detector simulation algorithm.

The event is generated by GENERIC/LUND interfaced package, which allows the user to freely choose some of the initial condition as well as the production and decay modes of a particle. The GENERIC starts by simulating an electron impinging in the radiator. Once a photon energy is chosen, LUND software(Jetset 7.4/Pythia 5.7) is activated to generate $c\bar{c}$ events. The user specified charm particle may be forced to decay according to a fully specified matrix element by the user. The other charmed hadron is allowed to decay according to an approximate matrix element and branching ratio given by GENERIC. Other non-charm particles in the event also decay according to an approximate matrix element and branching ratio given by LUND package.

The ROGUE Monte Carlo package traces an individual particle through the spectrometer. The primary advantage of ROGUE is that it is extremely fast. The basic philosophy of ROGUE is to simulate the response of individual detectors using distributions deduced directly from data. In this section, only IE and IM simulations are described.

5.2.1 IE Simulation

An energy deposition algorithm is used rather than a electromagnetic cascade simulation. The algorithm deposits energy longitudinally and transversely based on information from both calibration runs and showers from real data. The electromagnetic cascades are based on electron calibration data and electrons from $\gamma \longrightarrow e^+e^-$ while the hadronic showers are drawn primarily from pion calibration runs. More detailed description can be found else where[24].

The electron identification efficiency for MC simulation is higher than for data which suggests a post-hoc efficiency correction is required when comparing modes which have different numbers of electrons in the final state. The effiency discrepancy between data and Monte Carlo is worse than the $\sim 3\%$ of average correction.

5.2.2 Muon Simulation

Simulated muon tracks are scattered through the material in the downstream part of the inner E687 spectrometer. If a track reaches the inner muon system after energy losses and multiple Coulomb scattering, hits are assigned in a detector plane based on the scattered position of the simulated muon track at the detector plane and the efficiency of the counter hit in that plane. The detailed description can be found[25]. The contributions from hadron showers are added to the hits generated by the muon simulation. Also noise effects are simulated with adding noise in a plane.

The performance of the simulation is excellent. The muon identification between data and simulated data are in good agreement.

5.3 Lepton Misidentification

One of the difficulties in the semileptonic decay analysis is determining the amount of background from other decays. In the decay of $\Xi_c^0 \longrightarrow \Xi^- l^+ X$, the background contribution from the random correlation of a real Ξ^- with a fake lepton is expected to be largest. For instance, in a decay of $\Xi_c^0 \longrightarrow \Xi^- \pi^+ \pi^0$, if π^0 is missing and π^+ is misidentified to μ^+, there is no discrimating power between $\Xi_c^0 \longrightarrow \Xi^- \mu^+ \nu$ and $\Xi_c^0 \longrightarrow \Xi^- \pi^+ \pi^0$.

It is imperative to accurately understand the identification and misidentification of leptons (electron and muon) in this analysis work.

The lepton misidentification of the pion is studied using a high statistics SSD $K_s^0 \longrightarrow \pi^+\pi^-$ sample shown in Figure 5.1. The distributions are fitted to the Gaussian and the second order polynomial background. The signal widths of 3.24 MeV/c^2 and 0.64 are obtained for Figure 5.1-a) and Figure 5.1-b), respectively.

The selection criteria for the K_s^0 sample are:

- The pion candidates must pass through all five chamber stations of the PWC system.
- The pion PWC track must be singly linked to an SSD track.
- No Čerenkov particle identification is required.
- The L/σ of K_s^0 is required to be greater than 5.
- The fit confidence level of the $\pi^+\pi^-$ vertex from the K_s^0 is required to be greater than 1%.

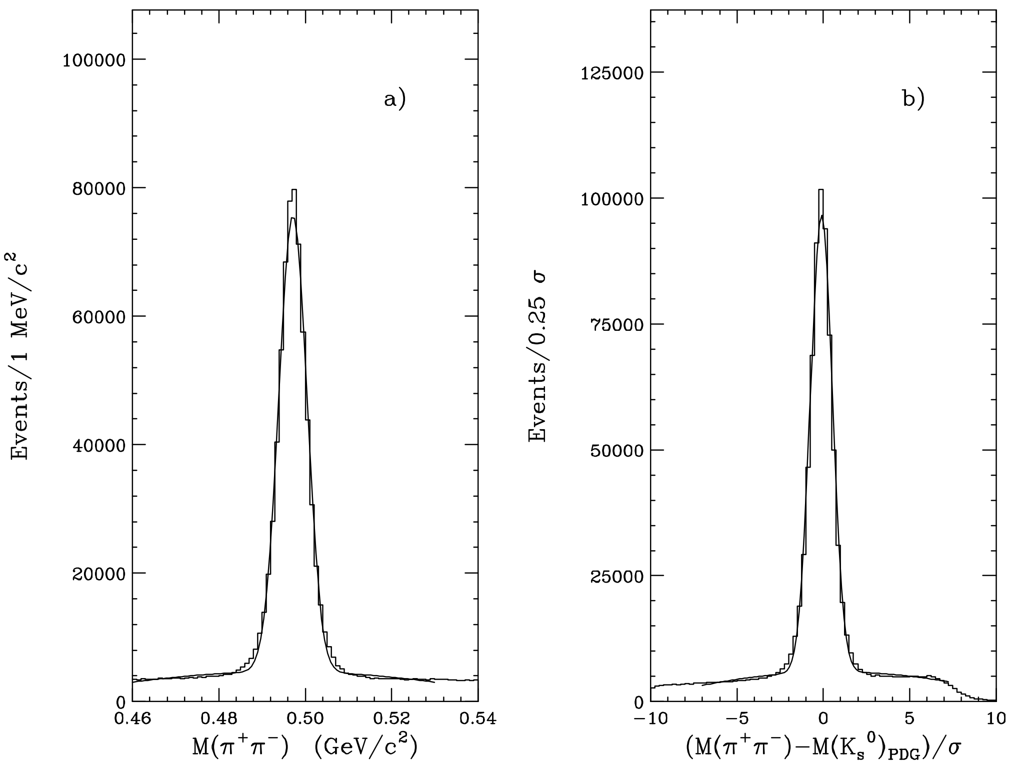

Figure 5.1: The K_s^0 mass distributions: a) the $\pi^+\pi^-$ invariant mass distribution of K_s^0, and b) the normalized K_s^0 mass distribution of $(M(\pi^+\pi^-) - M(K_s^0)_{PDG})/\sigma$.

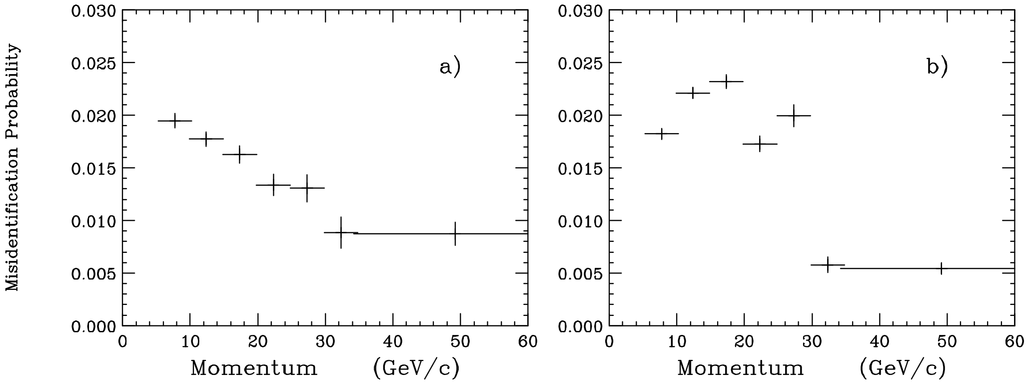

Figure 5.2: The muon misidentification of the pions from K_s^0 at different momenta a) for 1990 data, b) for 1991 data

Once the candidate K_s^0 is selected, we fit $(M(\pi^+\pi^-)-M(K_s^0)_{PDG})/\sigma$, where σ is the calculated K_s^0 mass error. The momentum dependent misidentification is obtained by using yields from the fit and the following formulae,

$$P = \frac{Events\ with\ IDMUDST\ \neq\ 0}{total\ events}\ for\ the\ muon\ , and$$

$$P = \frac{Events\ with\ (IDIEDST\ =\ 1\ and\ 0.8\ <\ E/p\ <\ 1.5)}{total\ events}\ for\ the\ electron.$$

The lepton misidentification probabilities are shown in Figure 5.2 for the muon and in Figure 5.3 for the electron. The misidentification probabilities of the muon and electron are comparable to the previous studies [24, 25].

In the uniform 1990 muon system, the misidentification is dominated by random noise and we need only a momentum dependent misidentification probability. But in the 1991 muon configuration the hole in the muon system requires a position dependence as well as a momentum dependence. The π tracks of the K_s^0 are projected in X and Y at IM1X. There is a significant position dependence in the 1991 system, but not in the 1990 system as shown in Figure 5.4.

The major source of misidentification in the muon system is due to the hadron

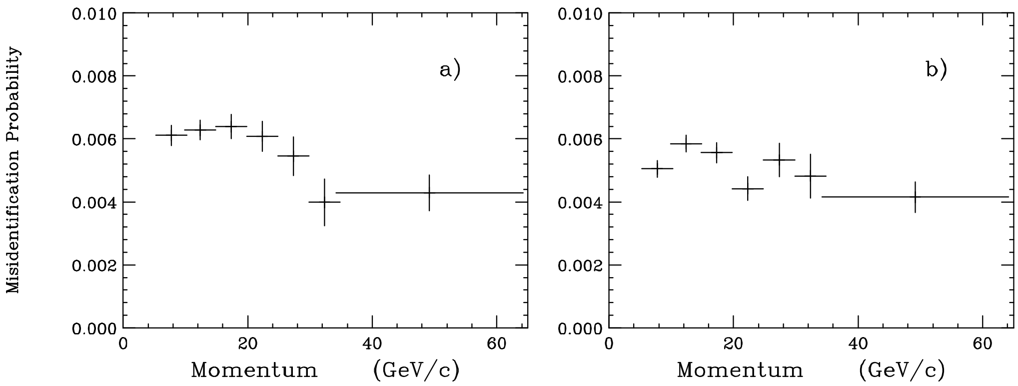

Figure 5.3: The electron misidentification of the pions from K_s^0 at different momentum a) for 1990 data, b) for 1991 data

showers penetrating the absorption material(muon filter). The misidentification from particles that decay into a muon accounts for about 15% of the total pion misidentification.

The proton and kaon misidentification probabilities in the muon system are comparable to the pion misidentification. The detailed studies are described in the reference [25].

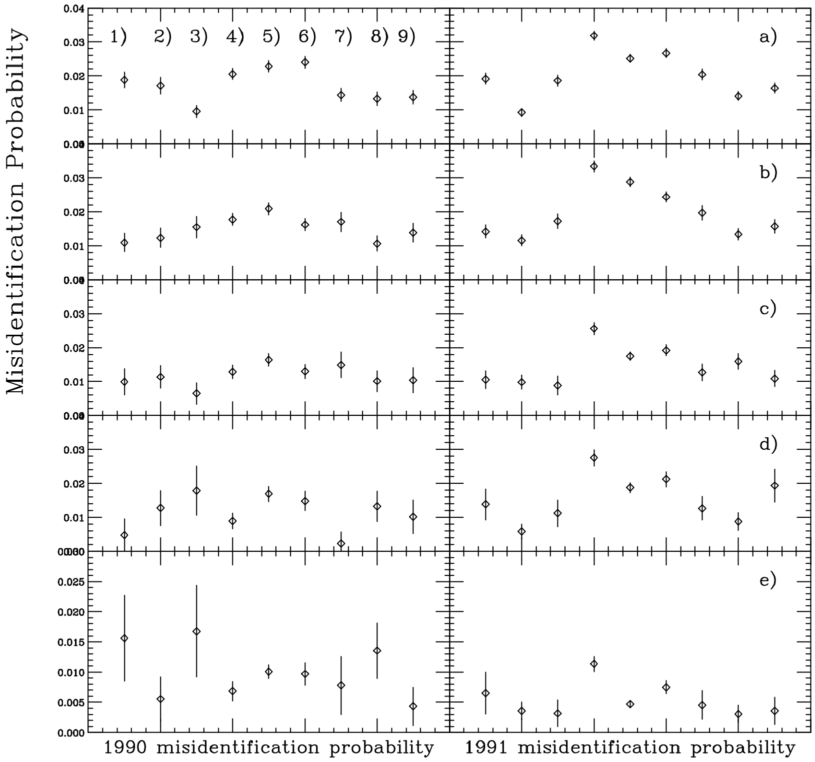

Figure 5.4: The muon misidentification of pions from K_s^0, the momentum ranges of a)$10 \sim 15$ GeV/c , b)$15 \sim 20$ GeV/c , c)$20 \sim 25$ GeV/c , d)$25 \sim 30$ GeV/c , e)> 30 GeV/c , the position ranges of 1)$X < -20,\ Y < -40$ cm, 2)$-20 < X < 20,\ Y < -40$ cm, 3)$20 < X,\ Y < -40$ cm, 4)$X < -20,\ -40 < Y < 40$ cm, 5)$-20 < X < 20,\ -40 < Y < 40$ cm, 6)$20 < X,\ -40 < Y < 40$ cm, 7)$X < -20,\ Y > 40$ cm, 8)$-20 < X < 20,\ Y > 40$ cm, 9)$20 < X,\ Y > 40$ cm.

Chapter 6

Ξ_c^0 Semileptonic Decays

The semileptonic decays of charmed baryon Ξ_c^0 to $\Xi^-\mu^+X$ and Ξ^-e^+X are discussed in this chapter. The reconstruction of the Ξ_c^0 baryon is difficult partly because of its shorter lifetime and partly because of its lower production rate relative to charmed mesons. We infer the existence of the Ξ_c^0 via its point of production and decay products.

6.1 Event Selection

This analysis is based on the Ξ^-/Ω^- skim sample of about 500,000 events from the entire 1990-1991 data. This skim came from the *tiny skim* tapes where any duplicate events have been removed. In this analysis, we used only the type 2 Ξ^- which decayed downstream of the silicon microstrip detector(SSD) where the Ξ^- track is reconstructed in the SSD. We selected a candidate of $\Xi_c^0 \longrightarrow \Xi^- l^+ X$ decay with the following requirements:

- Ξ^- selection
  - The daughter Λ baryon invariant mass is required to be within $\pm$ 15 MeV/c^2 of its world average of 1115.684 MeV/c^2 .

– The daughter Λ is reconstructed through its decay to $p\pi^-$ and the decay vertex of the Λ must be downstream of the Ξ^- decay vertex.

– A cut is made on the difference between the X and Y slopes of the Ξ^- SSD track and the slopes given by the sum of the Λ and the Multiwire Proportional Chamber(PWC) π^- track momentum vectors; The ANGLX and ANGLY, defined as the X slope difference and the Y slope difference, respectively, are required to be less than a certain value. For 1-link Λ's, tighter cuts of ANGLX, less than 0.001, and ANGLY, less than 0.002, are used. For un-linked Λ's, ANGLX, less than 0.004, and ANGLY, less than 0.004, are required.

– The transverse distance between the space point where a Λ and a PWC track make their closest approach and the point where a Ξ^- SSD track and the PWC track make their closest approach is defined as CASIMP. The CASIMP is required to be less than 1.2 cm.

– The combination with the smallest $\sqrt{ANGLX^2 + ANGLY^2}$ is chosen if there is more than one combination of $\Lambda\pi^-$ matched to the single SSD Ξ^- track.

– Microstrip(*type8*) and SSD(*type9*) Λ baryons are explicitly removed from the type 2 Ξ^- sample.

This set of Ξ^- cuts will be referred to as the *standard* Ξ^- cuts.

– L/σ_L is required to be greater than 2.0, where L is the distance between Ξ^- decay vertex and Λ decay vertex, and σ_L is the error on L.

The $\Lambda\pi^-$ invariant mass plot for the Ξ^- candidates decaying downstream of the SSD is shown in Figure 6.1. The distributions are fitted to the Gaussian signal with the background function of

$$A(M - m_{thresh})^B exp[-C(M - m_{thresh})]$$

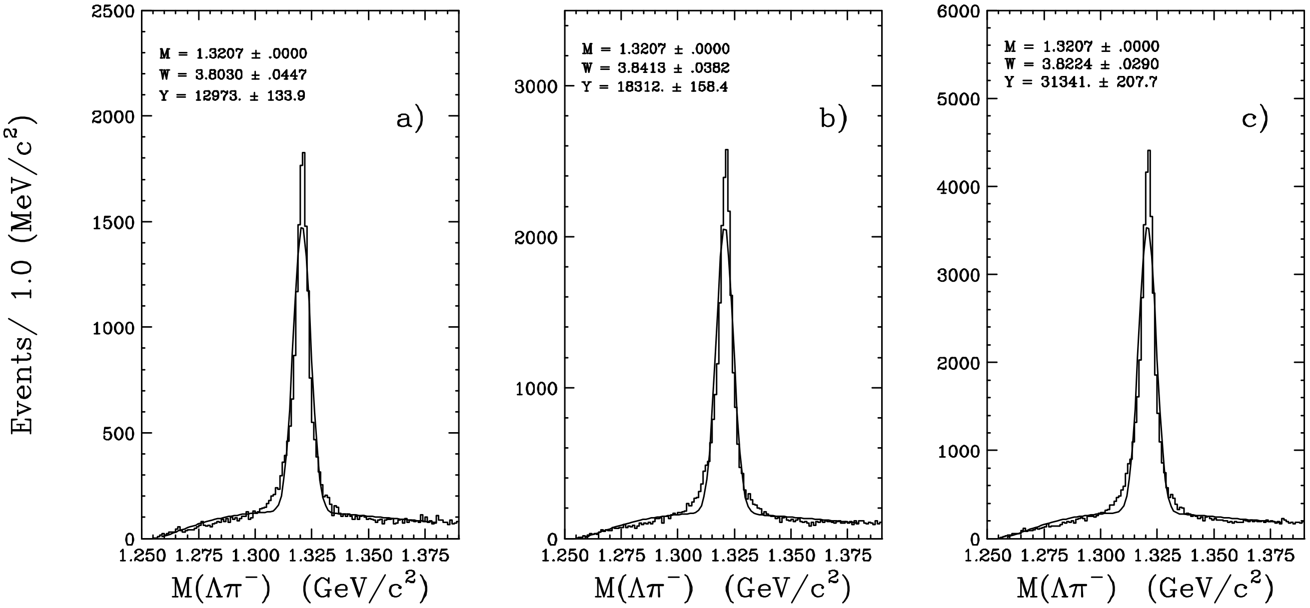

Figure 6.1: The $\Lambda\pi^-$ invariant mass distributions for the Ξ^- candidates decaying downstream of the SSD: a) for the 1990 data, b) for the 1991 data, c) for the combined 1990 and 1991 data.

where m_{thresh} is the mass sum of Λ and π, and A, B, and C are free fit parameters, using a binned likelihood method.

- The muon candidate must pass through all five chamber stations of the PWC system and must be identified by the inner muon system as the muon(IDMUDST $\neq$ 0). For the muon analysis, only good muon runs [25] were used.

- The electron candidate must pass through all five chamber stations of the PWC system and must be identified by the inner electromagnetic calorimeter(IE) as an electron(IDIEDST = 1). The E/p ratio of the candidate electron is required to be between 0.8 and 1.5, where E denotes the energy deposited in the IE and p is the momentum of the track.

- A lepton(muon or electron) PWC track must be singly linked to an SSD track. The doubly linked tracks have larger background contributions and a potential to be from e^+e^- production in the electron mode.
- A 10 GeV/c momentum cut is applied to lepton candidates in both 1990 and 1991 runs. This cut is used to reduce contamination from misidentification (mostly from pion decays and noise) and to avoid the region of uncertainty in the identification probability.

Once the candidate tracks are selected, the Ξ^- and lepton miscrostrip tracks are fitted to determine whether these two particles belong to a common vertex, the charm decay vertex. We required the confidence level(CLD) for this hypothesis to be greater than 1%. The charm decay vertex is required to be upstream of the trigger counter, TR1.

We form a mass using four momenta of the candidate tracks and require the mass to be less than 2.45 GeV/c^2. This mass cut removes most of the $\Xi_c^0 \longrightarrow \Xi^-\pi^+$ contamination.

Once the charm decay vertex is constructed, we have to reconstruct the production vertex of charm in order to look at the separation between the production and decay vertices. We use the Stand-alone vertex algorithm(DVFREE) to find the primary vertex. The previously assigned Ξ^- and lepton(electron or muon) tracks are excluded from forming the candidate primary vertices. Any pair of tracks which form a vertex in space with the confidence level(CLP) greater than 1% is kept as a candidate primary vertex. All other tracks are added to this vertex as long as the confidence level for a vertex hypothesis remains above 1%. Tracks which are not in this vertex are used to form other pairs to find additional clusters. For each vertex, the previously used tracks can belong to other clusters.

A primary vertex with the highest multiplicity is chosen as the production vertex which must be inside the target volume, and the largest L/σ vertex is selected if there is more than one vertex found with the same highest multiplicity.

If there are any leftover tracks not assigned to the charm and primary vertices, we check whether any of these leftover tracks are compatible with originating from the charm vertex. These tracks are added to the charm vertex and the highest confidence level(ISO2) of the new object is required to be less than 0.0001. This cut is applied to reduce the backgrounds where we have additional charged tracks in the charm vertex.

6.2 Invariant Mass of $\Lambda\pi^-$

The $\Lambda\pi^-$ invariant mass for both the right sign(e.g.$\Xi^- l^+$) and wrong sign(e.g. $\Xi^- l^-$) $\Xi\mu$ pairs are shown in Figure 6.2, and Ξe pairs in Figure 6.3.

There appears to be an excess of the right sign Ξ^- baryon compared to the wrong sign Ξ^- for both the muon and electron modes. The distributions are fitted to the Gaussian signal with the background function of

$$A(M - m_{thresh})^B exp[-C(M - m_{thresh})]$$

where m_{thresh} is the mass sum of Λ and π, and A, B, and C are free fit parameters, using a binned likelihood method. The signal width is fixed at 4.0 MeV/c^2 as determined by the Monte Carlo simulation. The fit results for each mode are listed in Table 6.1. From fit to the $\Lambda\pi^-$ distributions at $L/\sigma > 0.5$, we have obtained 38.5 $\pm$ 11.0 and 14.7 $\pm$ 7.7 excess events of the right sign Ξ^- baryon compared to the wrong sign Ξ^- for the muon and the electron mode, respectively. The distributions of $\Lambda\pi^-$ for each mode are again fitted without fixing the signal width. The fit results with free signal width for each mode are listed in Table 6.2. The signal widths of 4.30 $\pm$ 0.50 MeV/c^2 and 4.69 $\pm$ 0.93 MeV/c^2 are obtained for the right sign and the wrong sign muon mode, respectively. For the electron mode, the signal widths of 3.92 $\pm$ 0.66 MeV/c^2 and 3.38 $\pm$ 1.13 MeV/c^2 are obtained for the right sign and the wrong sign, respectively. The distributions of $\Lambda\pi^-$ for each mode are again fitted

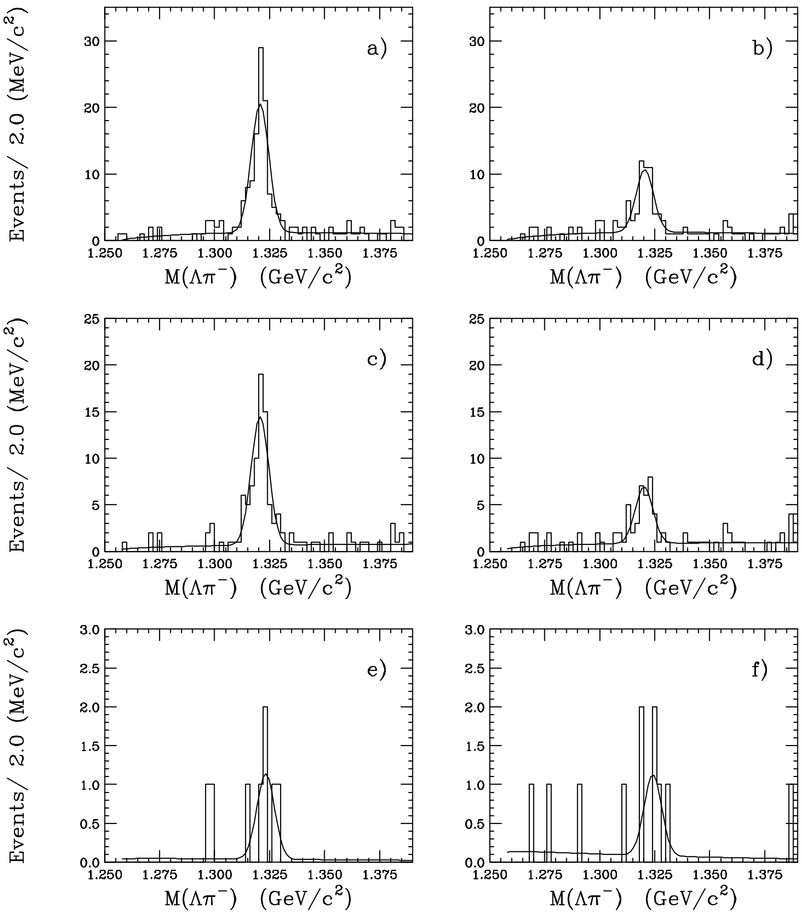

Figure 6.2: The $\Lambda\pi^-$ invariant mass distributions for $\Xi_c^0 \longrightarrow \Xi^-\mu^+X$ decay at different L/σ requirements: (a) Right Sign and (b) Wrong Sign for $L/\sigma > 0.0$, (c) Right Sign and (d) Wrong Sign for $L/\sigma > 0.5$, and (e) Right Sign and (f) Wrong Sign for $L/\sigma > 4.0$.

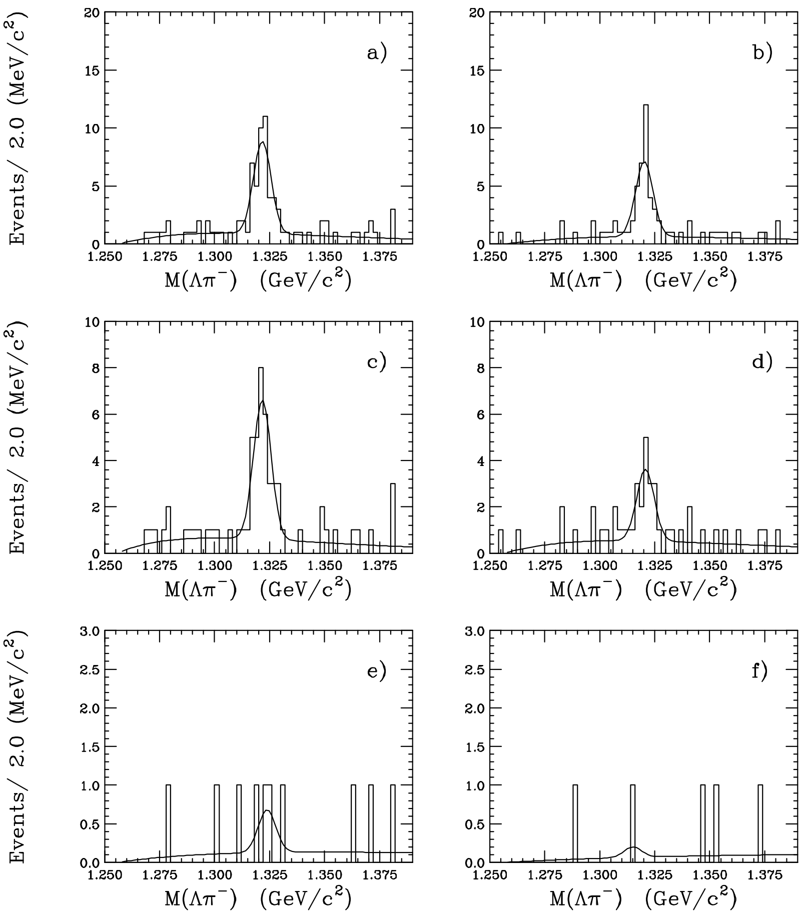

Figure 6.3: The $\Lambda\pi^-$ invariant mass distributions for $\Xi_c^0 \longrightarrow \Xi^- e^+ X$ decay at different L/σ requirements: (a) Right Sign and (b) Wrong Sign for $L/\sigma > 0.0$, (c) Right Sign and (d) Wrong Sign for $L/\sigma > 0.5$, and (e) Right Sign and (f) Wrong Sign for $L/\sigma > 4.0$.

Table 6.1: Results from $\Lambda\pi^-$ distributions for the $\Xi^- l^+ X$ decay modes in Figure 6.2 and in Figure 6.3, where errors are only statistical errors.

Decay modes	L/σ	Right Sign(RS)	Wrong Sign(WS)	$RS - WS$
$\Xi_c^0 \longrightarrow \Xi^- \mu^+ X$	> 0.0	96.8 ± 10.7	47.1 ± 8.0	49.7 ± 13.3
	> 0.5	69.0 ± 8.9	30.4 ± 6.5	38.5 ± 11.0
	> 4.0	5.5 ± 2.5	5.2 ± 2.5	0.3 ± 3.5
$\Xi_c^0 \longrightarrow \Xi^- e^+ X$	> 0.0	40.0 ± 7.1	32.5 ± 6.2	7.5 ± 9.4
	> 0.5	30.2 ± 6.1	15.5 ± 4.6	14.7 ± 7.7
	> 4.0	2.8 ± 2.0	0.7 ± 1.0	2.1 ± 2.3

with fixing the signal width at 3.82 MeV/c^2 as obtained from Figure 6.1. The fit results for each mode are listed in Table 6.3.

6.3 Background Issues

Detailed sources of backgrounds should be considered. The first source of backgrounds considered is a real lepton with a fake Ξ^-, which can come from a real/fake Λ with a fake/real pion. This background is essentially eliminated by fitting for the Ξ^- in the $\Lambda\pi^-$ mass plot. This background can still adversely affect the results if an incorrect fitting function is used.

The second background source is the random correlation of a real Ξ^- with a real lepton, each from a separate source. This background contributes approximately equal numbers to the right sign and the wrong sign pairs.

The third background source is the random combination of a real Ξ^- with a fake lepton. We analyze both the right sign and wrong sign $\Xi^- h^+$ pairs as in the $\Xi_c^0 \longrightarrow \Xi^- l^+ X$ analysis without the lepton identification. The study of the lepton

Table 6.2: Fit results from $\Lambda\pi^-$ distributions with a free signal width for the $\Xi^- l^+ X$ decay modes, where errors are only statistical errors.

Decay modes	L/σ	Right Sign(RS)	Wrong Sign(WS)	$RS - WS$
	> 0.0	95.4 ± 11.1	49.0 ± 8.9	46.4 ± 14.2
$\Xi_c^0 \longrightarrow \Xi^- \mu^+ X$	> 0.5	70.3 ± 9.0	32.5 ± 7.1	37.8 ± 11.5
	> 4.0	5.6 ± 2.5	5.7 ± 2.8	-0.1 ± 3.7
	> 0.0	39.4 ± 7.2	30.4 ± 6.3	9.0 ± 9.6
$\Xi_c^0 \longrightarrow \Xi^- e^+ X$	> 0.5	30.1 ± 6.2	14.7 ± 4.7	15.3 ± 7.8
	> 4.0	2.8 ± 2.1	0.8 ± 1.0	2.0 ± 2.3

Table 6.3: The fit results from $\Lambda\pi^-$ distributions with fixing the signal width at 3.82 MeV/c^2 as obtained from Figure 6.1 for the $\Xi^- l^+ X$ decay mode, where errors are only statistical errors.

Decay modes	L/σ	Right Sign(RS)	Wrong Sign(WS)	$RS - WS$
	> 0.0	95.7 ± 10.6	49.2 ± 7.9	49.5 ± 13.3
$\Xi_c^0 \longrightarrow \Xi^- \mu^+ X$	> 0.5	68.1 ± 8.9	29.8 ± 6.4	38.4 ± 11.0
	> 4.0	5.5 ± 2.5	5.2 ± 2.5	0.3 ± 3.5
	> 0.0	39.5 ± 7.0	32.2 ± 6.2	7.4 ± 9.4
$\Xi_c^0 \longrightarrow \Xi^- e^+ X$	> 0.5	29.9 ± 6.1	15.3 ± 4.5	14.6 ± 7.6
	> 4.0	2.7 ± 2.0	0.7 ± 1.0	2.0 ± 2.3

Table 6.4: The fit results from $\Lambda\pi^-$ distributions for the $\Xi^- l^+ X$(fake lepton) decay modes at different L/σ requirements, where errors are only statistical errors.

Decay modes	L/σ	Right Sign	Wrong Sign
$\Xi_c^0 \longrightarrow \Xi^- \mu^+ X$(fake muon)	> 0.0	66.6 ± 8.9	49.1 ± 7.7
	> 0.5	46.4 ± 7.4	33.5 ± 6.3
	> 4.0	2.6 ± 1.8	2.0 ± 1.6
$\Xi_c^0 \longrightarrow \Xi^- e^+ X$(fake electron)	> 0.0	27.7 ± 5.7	19.5 ± 4.9
	> 0.5	19.3 ± 4.8	13.5 ± 4.0
	> 4.0	1.2 ± 1.2	0.8 ± 1.0

misidentification of the hadron is described in section 5.3.

We assume that the h^+ charged particle is a pion because most charged particles are the pions in this experiment. The $\Xi^- h^+$ events are weighted according to the momentum dependent misidentification probabilities except for the 1991 muon analysis. For the 1991 muon analysis, the $\Xi^- h^+$ events are weighted according to the position and momentum dependent misidentification probabilities. The $\Lambda\pi^-$ invariant mass for both the right sign and wrong sign random combinations of a real Ξ^- with a fake lepton are shown in Figure 6.4 for the muon decay mode and in Figure 6.5 for the electron decay mode.

The distributions are fitted to the Gaussian signal with the background function of

$$A(M - m_{thresh})^B exp[-C(M - m_{thresh})]$$

where m_{thresh} is the mass sum of Λ and π, and A, B, and C are free fit parameters, using a binned likelihood method. The signal width is fixed at 4.0 MeV/c^2 . The fit results for each mode are listed in Table 6.4.

The study shows that the estimated wrong sign pairs from a real Ξ^- and a

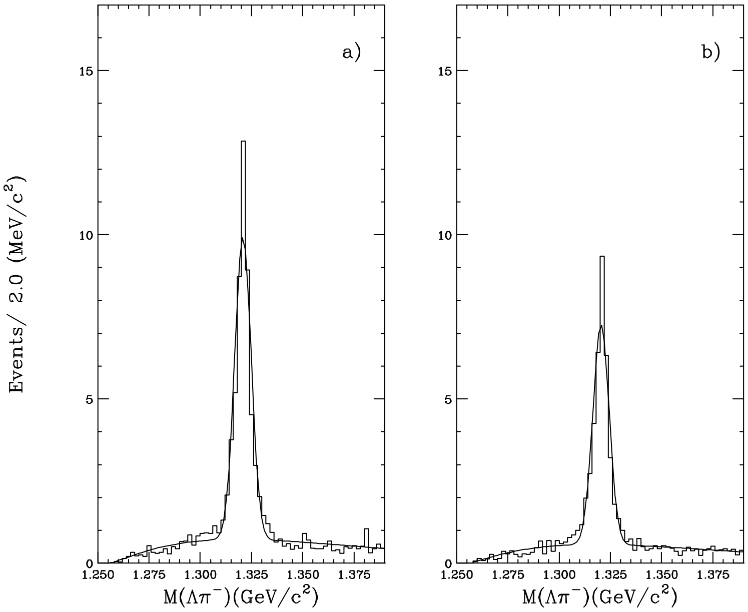

Figure 6.4: The $\Lambda\pi^-$ invariant mass distributions for a real Ξ with a fake muon at $L/\sigma > 0.5$: (a) for the right sign, (b) for the wrong sign.

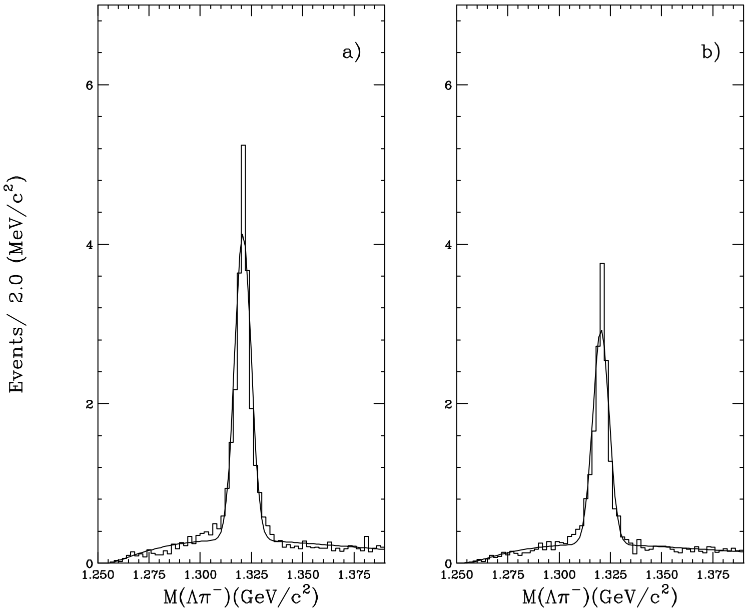

Figure 6.5: The $\Lambda\pi^-$ invariant mass distributions for a real Ξ with a fake electron at $L/\sigma > 0.5$: (a) for the right sign, (b) for the wrong sign.

fake lepton, which is misidentified, is equal to the number of wrong sign Ξl pairs within statistical error. We can conclude that the background from the random combination of a real Ξ^- and a fake lepton is the largest source in this analysis, and the background from the random correlation of a real Ξ^- with a real lepton, each from a separate source is negligible.

There are 12.9 ± 9.6 and 6.8 ± 6.2 right sign excess events to wrong sign events for the muon and the electron mode, respectively in the background estimation at $L/\sigma > 0.5$. This excess of right sign events over wrong sign events can be explained by the difference in the production rate of the right sign and the wrong sign in the experiment. The production difference comes partly from the presence of $\Xi^{*0}(1530) \longrightarrow \Xi^-\pi^+$ and partly from other charm baryon decays.

The $\Xi^{*0}(1530) \longrightarrow \Xi^-\pi^+$ in the $\Xi^-\pi^+$ sample where pion is misidentified as a lepton is considered. Figure 6.6 shows the $\Xi\pi$ invariant masses for both the right sign and wrong sign random combinations of a real Ξ^- with a fake lepton. The study shows that about 3 events to the right sign excess is explained with the presence of $\Xi^{*0}(1530)$ in the sample. This contribution could be eliminated by removing all $\Xi^-\pi^+$ events from subsequent analysis that are within $3.0\sigma(\sim 8\ \text{MeV}/c^2)$ of $\Xi^{*0}(1530)$. This contributes about 5 events to the right sign, and about 2 events to the wrong sign combination for both the muon and electron modes. However no such cut is applied to remove $\Xi^{*0}(1530)$ throughout this analysis as this would significantly reduce the signal yield.

The $\Xi_c^0 \longrightarrow \Xi^-(n)\pi^0\pi^+$ and $\Xi_c^0 \longrightarrow \Xi^-\pi^+$ decays where the charged pion is misidentified as the lepton might contribute to an excess of the right sign in the $\Xi^-\pi^+$ sample. The $\Xi_c^0 \longrightarrow \Xi^-\pi^+$ decay is described in section 6.6.

The $\Xi_c^+ \longrightarrow \Xi^-\pi^+\pi^+$ decay where one of pion is missing and the other pion is misidentified as the lepton also might contribute to an excess of the right sign in the $\Xi^-\pi^+$ sample. We have selected the candidate $\Xi_c^+ \longrightarrow \Xi^-\pi^+\pi^+$ sample with the following requirements:

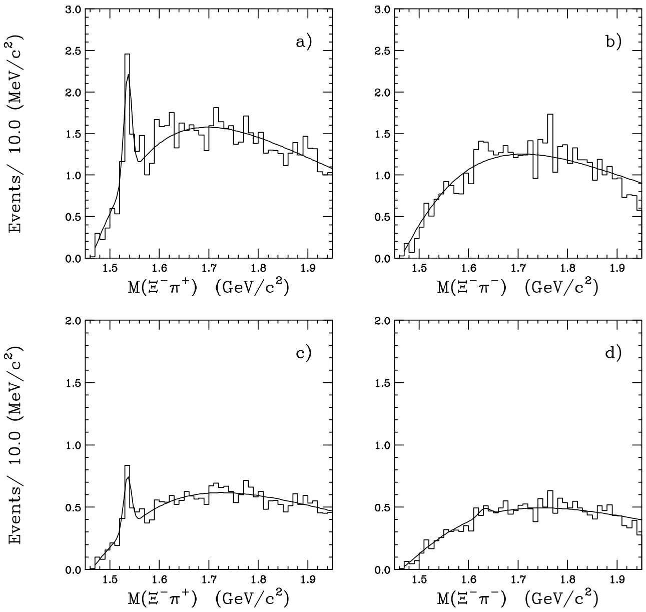

Figure 6.6: The $\Xi^-\pi^+$ invariant mass distributions for a real Ξ with a fack lepton at $L/\sigma > 0.5$: (a) for the right sign and (b) wrong sign in the muon mode, and (c) for the right sign and (d) wrong sign in the electron mode.

- Ξ^- is selected with the *standard* Ξ^- cuts described in the section 6.1.
- The invariant mass of the Ξ^- is within $\pm$ 10 MeV/c^2 of its world average of 1321.32 MeV/c^2 .
- Pion track is reconstructed in both the SSD and PWC systems and be linked. Also, the pions are required to be identified as not being electron, kaon, proton, kaon/proton ambiguous (ISTATP $\neq$ 1, 4, 8, or 12).
- Use DVNUCL [28] to find the primary vertex, which is required to be in the target region. The confidence level of the primary vertex (CLP) is greater than 1%.
- Charm decays upstream of TR1 and the confidence level of the charm vertex is greater than 1%.

The $\Xi^-\pi^+\pi^+$ invariant mass distributions using only type-2 Ξ^- are shown in Figure 6.7. The histograms are fitted to the gaussian signal and the second order polynomial background function. A binned likelihood fit to the $\Xi^-\pi^+\pi^+$ mass distribution yields 42.6$\pm$9.6 signal events at $L/\sigma > 2.0$.

The $\Lambda_c^+ \longrightarrow \Xi^- K^+\pi^+$ decay where either the kaon or the pion is missing and the other hadron is misidentified as a lepton is also considered. We have selected the candidate $\Lambda_c^+ \longrightarrow \Xi^- K^+\pi^+$ sample with the following requirements:

- Ξ^- is selected with the *standard* Ξ^- cuts described in the section 6.1.
- The invariant mass of the Ξ^- is within $\pm$ 10 MeV/c^2 of its world average of 1321.32 MeV/c^2 .
- Kaon track is reconstructed in both the SSD and PWC systems and be linked. Also, the kaon is required to be identified as being kaon, a kaon/proton ambiguous, or an electron/pion/kaon ambiguous if $p>$ 60.0 GeV/c (ISTATP = 4, 12, and 7).

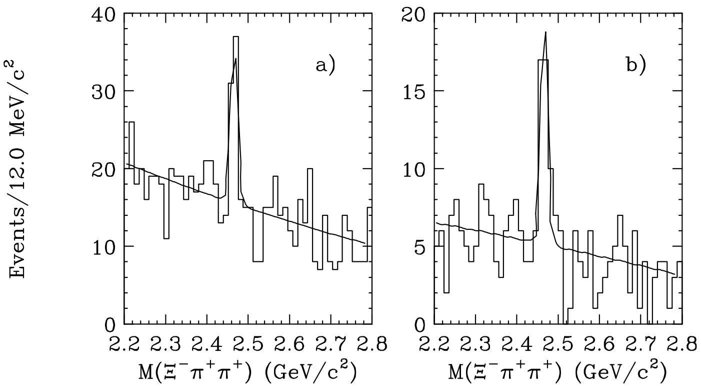

Figure 6.7: The $\Xi^-\pi^+\pi^+$ invariant mass distributions at different L/σ requirements: (a) $L/\sigma > 2.0$ and (b) $L/\sigma > 3.0$.

- Pion is reconstructed in both the SSD and PWC systems and be linked. Also, the pion is required to be identified as not being electron, kaon, proton, kaon/proton ambiguous (ISTATP $\neq$ 1, 4, 8, or 12).
- Use DVNUCL to find the primary vertex, which is required to be in the target region. The confidence level of the primary vertex (CLP) is greater than 1%.
- Charm decays upstream of TR1 and the confidence level of the charm vertex is greater than 1%.

The $\Xi^- K^+\pi^+$ invariant mass distributions using only type-2 Ξ^- are shown in Figure 6.8-(a) and (b) for $L/\sigma > 2.0$ and $L/\sigma > 4.0$, respectively. Figure 6.8-(c) and (d) show the $\Xi(1530)^0\pi^+$ invariant mass distribution of the resonant decay of $\Lambda_c^+ \longrightarrow \Xi(1530)^0(\rightarrow \Xi^-\pi^+)K^+$ for $L/\sigma > 2.0$ and $L/\sigma > 4.0$, respectively. The distributions are fitted to the gaussian signal and the second order polynomial background functions. A binned likelihood fit to the mass distributions in Figure 6.8-(a) and (c) yield 27.4±8.0 and 12.9±4.4, respectively.

The final source of considered backgrounds is contributions of other charm baryon semileptonic decays to the right sign signal. The decay of $\Xi_c^+ \longrightarrow \Xi^-\pi^+ l^+\nu$ is

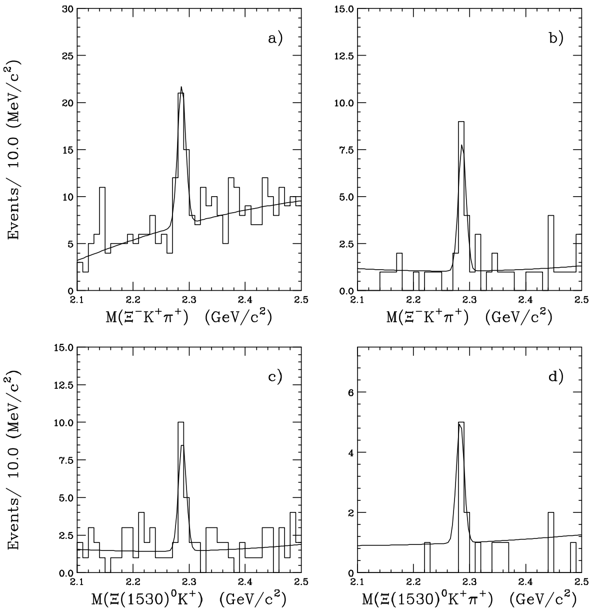

Figure 6.8: The $\Xi^- K^+\pi^+$ invariant mass distributions at (a) $L/\sigma > 2.0$ and (b) $L/\sigma > 4.0$ for $\Lambda_c^+ \longrightarrow \Xi^- K^+\pi^+$ decay, and at (c) $L/\sigma > 2.0$ and (d) $L/\sigma > 4.0$ for its resonant decay, $\Lambda_c^+ \longrightarrow \Xi(1530)^0(\rightarrow \Xi^-\pi^+)K^+$.

analyzed by looking for an excess of the right sign, $\Xi^-\pi^+l^+$ events over the wrong sign $\Xi^-\pi^+l^-$ events, but no excess is observed in this mode. The resonant decay of $\Xi_c^+ \longrightarrow \Xi^{*0}(1530)l^+\nu$ is examined by looking at an excess of the $\Xi^{*0}(1530)$ signal for the right sign combination, $\Xi^{*0}(1530)l^+$ to the wrong sign combination, $\Xi^{*0}(1530)l^-$. The $\Xi^-\pi^+$ invariant masses for both the right sign and wrong sign $\Xi^{*0}(1530)l^+$ pairs are shown in Figure 6.9. No right sign excess is seen.

The Λ_c^+ semileptonic decay mode with Ξ^-, $\Lambda_c^+ \longrightarrow \Xi^-K^+l^+\nu$ mode was studied by looking for an excess of the Ξ^- for the right sign combination to the wrong sign combination with a visible mass less than the Λ_c^+ mass. None of the right sign of ΞKl combination passed cuts. Also the $\Omega_c^0 \longrightarrow \Omega^-l^+\nu$ decay is analyzed by looking at the Ω for the right sign, Ω^-l^+ with applying loose cuts, but no right sign of Ωl pair survived. We assume that the background contributions from these charm semileptonic decay modes are negligible.

The equality of wrong sign pairs estimated from the source of the fake leptons with wrong sign Ξl pairs indicates that most of the wrong sign Ξl pairs can be explained by the random combination of a real Ξ^- with a fake lepton, and using the right sign background of the fake lepton estimates quantitatively all sources of misidentified lepton background which contributes to the right sign signal. The $\Xi_c^0 \longrightarrow \Xi^-l^+X$ semileptonic signal is obtained by subtracting the right sign background contribution from the fitted right sign signal. After this subtraction we obtained 22.6 ± 11.6 signal events and 10.8 ± 7.9 signal events for the muonic and the electronic mode, repectively at $L/\sigma > 0.5$.

6.4 Visible Mass Distribution

The Ξl invariant masses of both the right sign and wrong sign events are plotted in Figure 6.10 for the muon mode and in Figure 6.11 for the electron mode after performing the Ξ^- sideband subtraction. The invariant mass of Ξ^- is required to

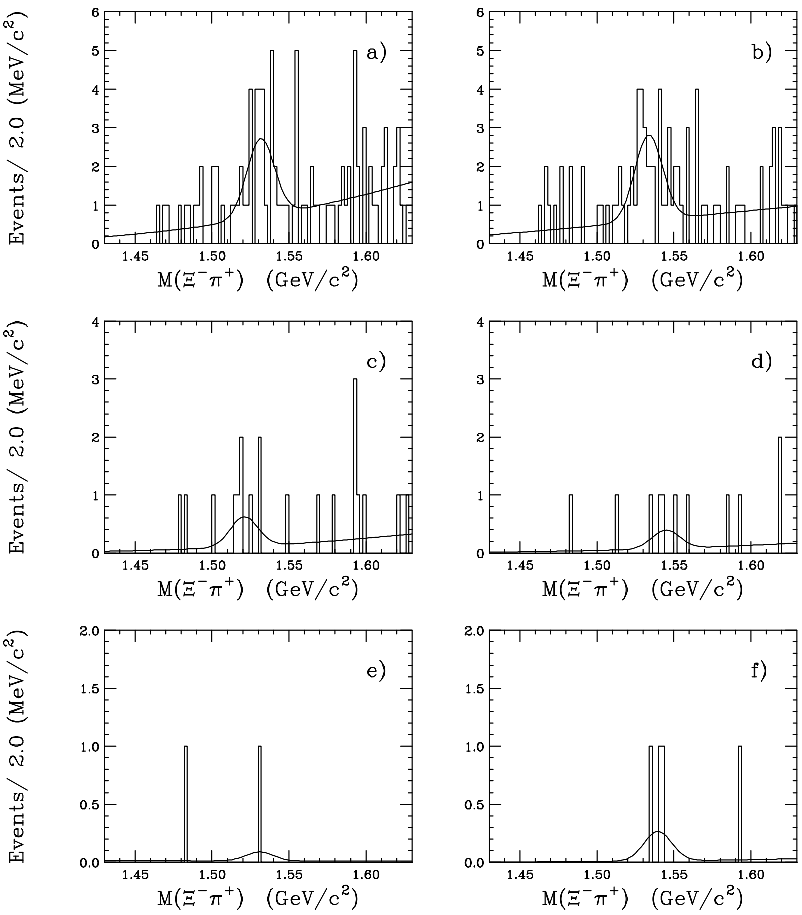

Figure 6.9: The $\Xi^-\pi^+$ invariant mass distributions for $\Xi_c^+ \longrightarrow \Xi^{*0}(1530)l^+X$ decay at different L/σ requirements: (a) Right Sign and (b) Wrong Sign for $L/\sigma > 0.0$, (c) Right Sign and (d) Wrong Sign for $L/\sigma > 2.0$, and (e) Right Sign and (f) Wrong Sign for $L/\sigma > 4.0$.

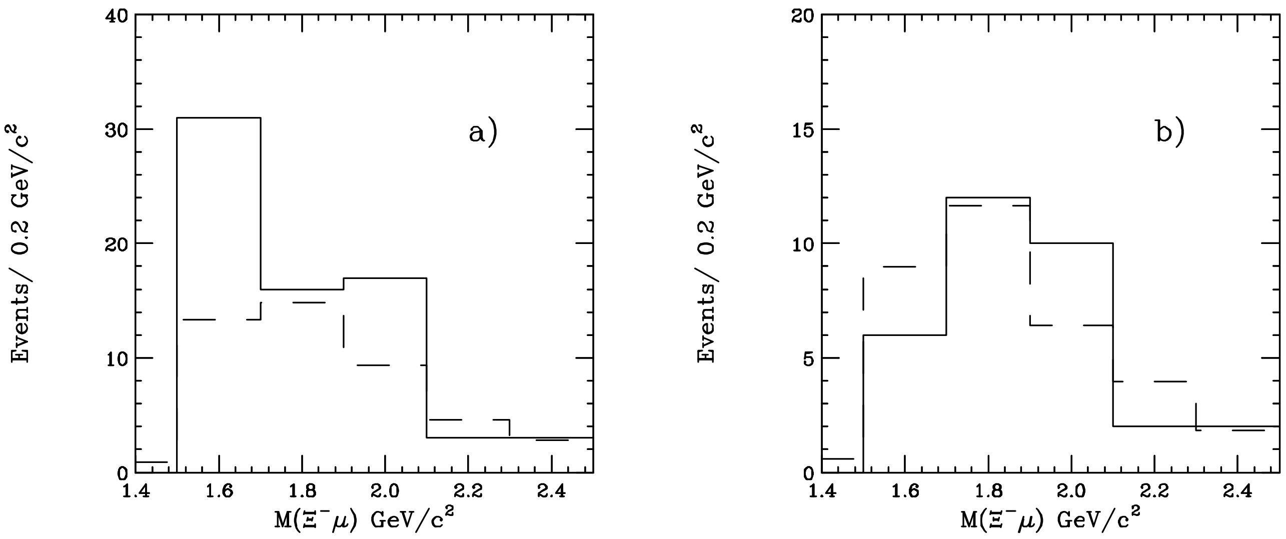

Figure 6.10: The M($\Xi\mu$) distributions after Ξ^- sideband subtraction. The M($\Xi\mu$) distributions, where the muon is a fake is overlaid as a dashed line: a) for the right sign, b) for the wrong sign.

be within $\pm$ 10 MeV/c^2 around its world average of 1321.32 MeV/c^2 . The sideband of Ξ^- is approximated as a linear shape and chosen $\pm$ 20 MeV/c^2 (about 5σ) away from the nominal mass of Ξ^- with 10 MeV/c^2 width.

Figure 6.12 and Figure 6.13 show the the Ξl invariant mass distributions of both the right sign and wrong sign combinations for the muon and the electron mode, respectively after the Ξ^- sideband and background from a fake lepton are subtracted.

The Monte Carlo visible mass distributions of various Ξ_c^0 semileptonic decays are shown in Figure 6.14.

6.5 Fitting Signal

The data is fitted using a binned maximum likelihood fitting technique to extract the amount of the $\Xi^- l^+ X$ signals. The likelihood function is constructed as:

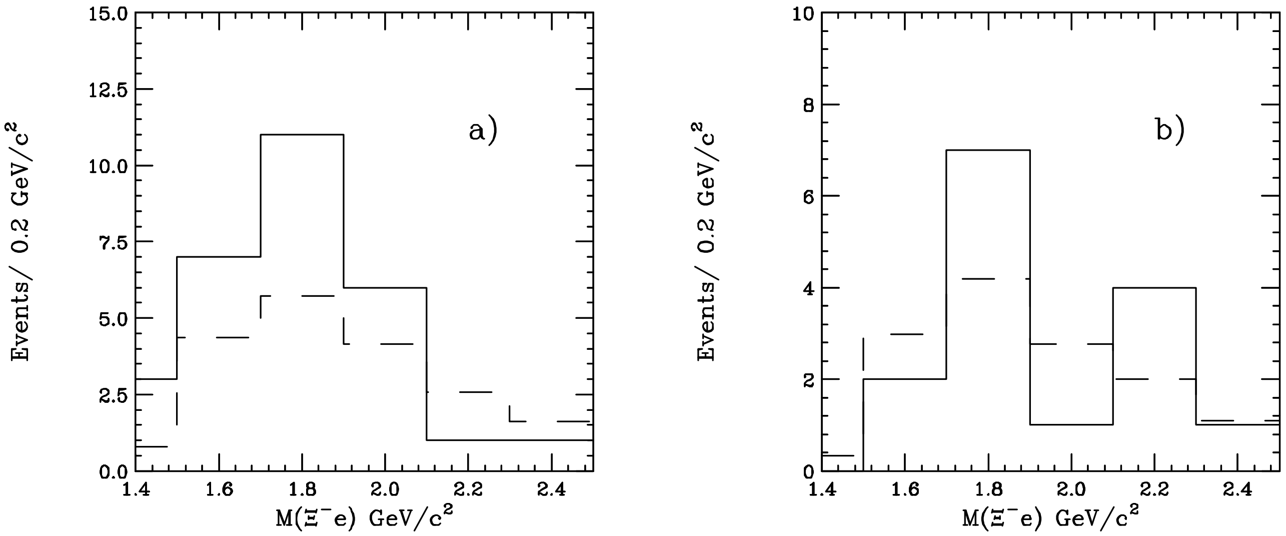

Figure 6.11: The M(Ξe) distributions after Ξ^- sideband subtracted. The M(Ξe) distributions, where electron is a fake is overlaid as a dashed line: a) for the right sign, b) for the wrong sign.

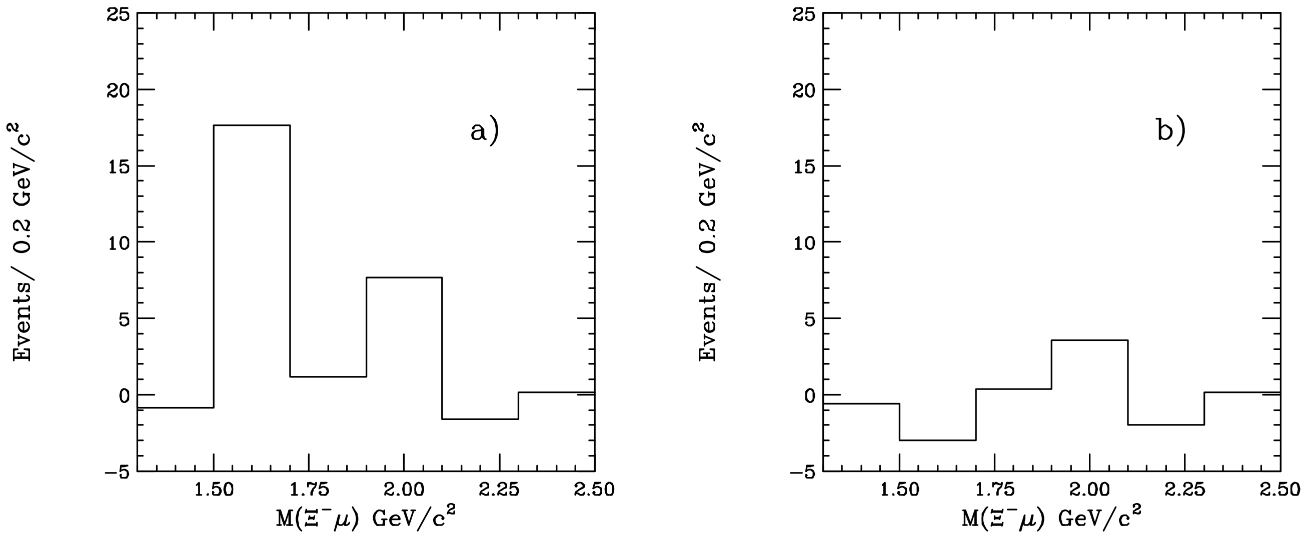

Figure 6.12: The M($\Xi\mu$) distribution after Ξ^- sideband and the background from a fake muon are subtracted: a) for the right sign, b) for the wrong sign.

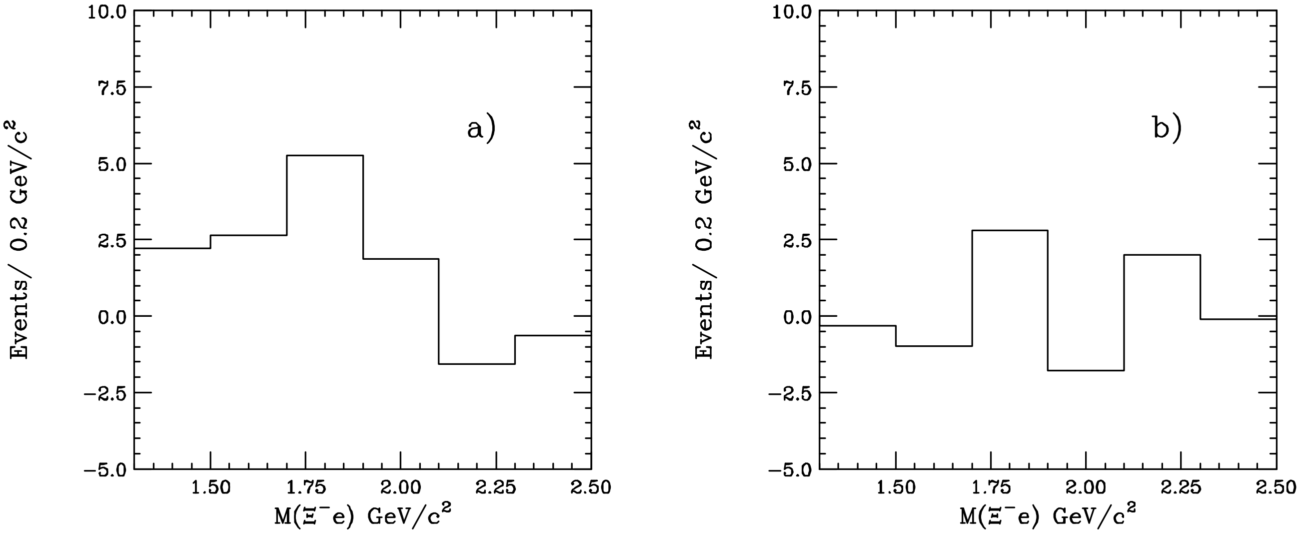

Figure 6.13: The M(Ξe) distribution after Ξ^- sideband and the background from a fake electron are subtracted: a) for the right sign, b) for the wrong sign.

$$\mathcal{L} = \prod_{i=1}^{\#bins} \frac{n_i^{s_i} e^{-n_i}}{s_i!} \tag{6.1}$$

where

s_i = number of right sign events in the ith bin of the data histogram
n_i = expected number of events in the ith bin of the fit histogram

The likelihood is the product over all bins of the Poisson probabilities of observed s_i entries in bin i when the expected number of entries is n_i.

The fit histogram is constructed using our knowledge of the decay process involved; the shape of $\Xi_c^0 \longrightarrow \Xi^- l^+ \nu$, $\Xi_c^0 \longrightarrow \Xi^-(n)\pi^0 l^+ \nu$ signals from Monte Carlo, and the level of the right sign random combination background described in the previous section:

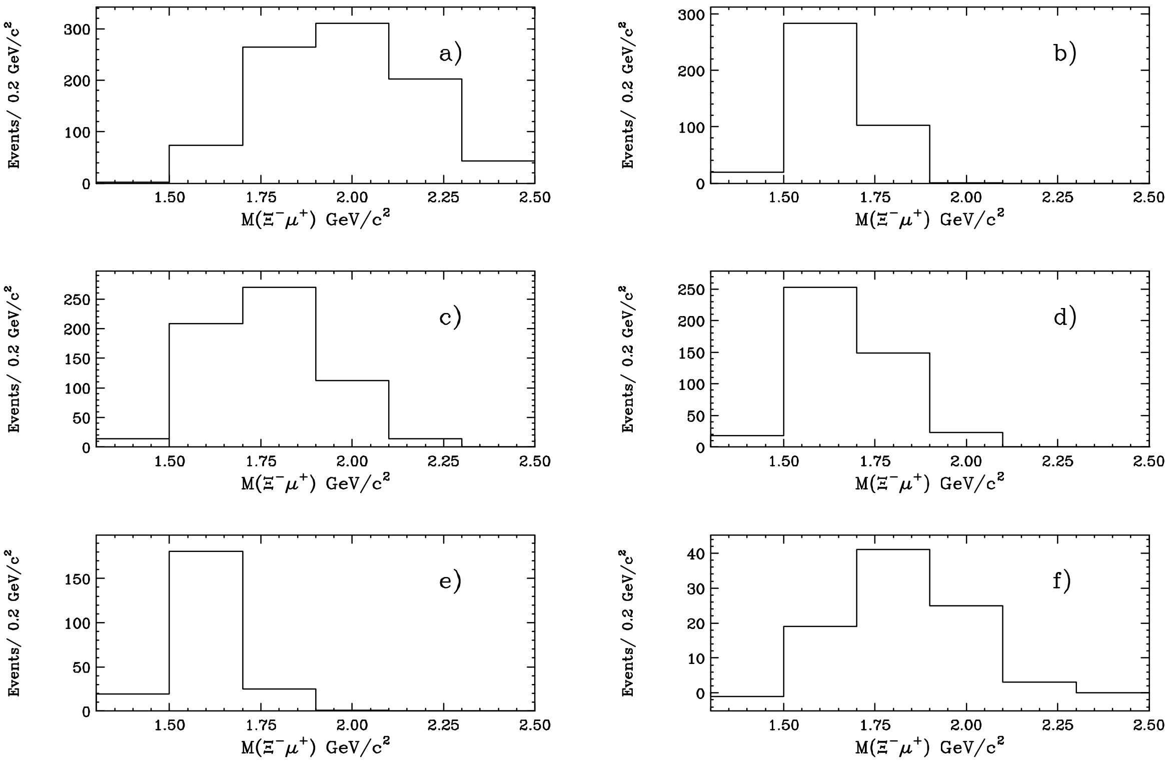

Figure 6.14: The expected M($\Xi\mu$) distributions from the Monte Carlo for different decays: a) $\Xi_c^0 \rightarrow \Xi^-\mu^+\nu$, b) $\Xi_c^0 \rightarrow \Xi^-\eta^0\mu^+\nu$, c) $\Xi_c^0 \rightarrow \Xi^-\pi^0\mu^+\nu$, d) $\Xi_c^0 \rightarrow \Xi^-2\pi^0\mu^+\nu$, e) $\Xi_c^0 \rightarrow \Xi^-3\pi^0\mu^+\nu$, and f) $\Xi_c^0 \rightarrow \Xi^{*-}(\ \Xi^{*-} \rightarrow \Xi^-\pi^0)\mu^+\nu$.

Table 6.5: The fit results for the $\Xi^-\mu^+X$ mode in Figure 6.15 and for the Ξ^-e^+X mode in Figure 6.16, where errors are only statistical errors.

Decay modes	Fit Yield
$\Xi_c^0 \longrightarrow \Xi^-\mu^+\nu$	5.6 ± 6.4
$\Xi_c^0 \longrightarrow \Xi^-(n)\pi^0\mu^+\nu$	18.7 ± 6.6
$\Xi_c^0 \longrightarrow \Xi^-e^+\nu$	2.2 ± 4.9
$\Xi_c^0 \longrightarrow \Xi^-(n)\pi^0e^+\nu$	6.9 ± 4.5

$$n_i = Y_{\Xi^-l^+\nu}S_{1i} \ + \ Y_{\Xi^-(n)\pi^0l^+\nu}S_{2i} \ + \ M_i \qquad (6.2)$$

where

Y denotes the signal yield;

S_{ji} is the fraction of Monte Carlo events in bin i for the j decay mode (for each fixed j; $\Sigma S_{ji} = 1$);

M_i is the number of right sign background events in bin i from lepton misidentification ($\Sigma M_i \neq 1$).

The components of the Ξ^-l^+X fit are shown in Figure 6.15 for the muon mode, and in Figure 6.16 for the electron mode.

The fit results for each mode are listed in Table 6.5. The values of the χ^2/D.O.F. returned by the fit are 3.39 and 2.57 for the muon mode and the electron mode, respectively.

6.6 $\Xi_c^0 \longrightarrow \Xi^-\pi^+$ Mode

We have selected a candidate $\Xi_c^0 \longrightarrow \Xi^-\pi^+$ sample with the following requirements:

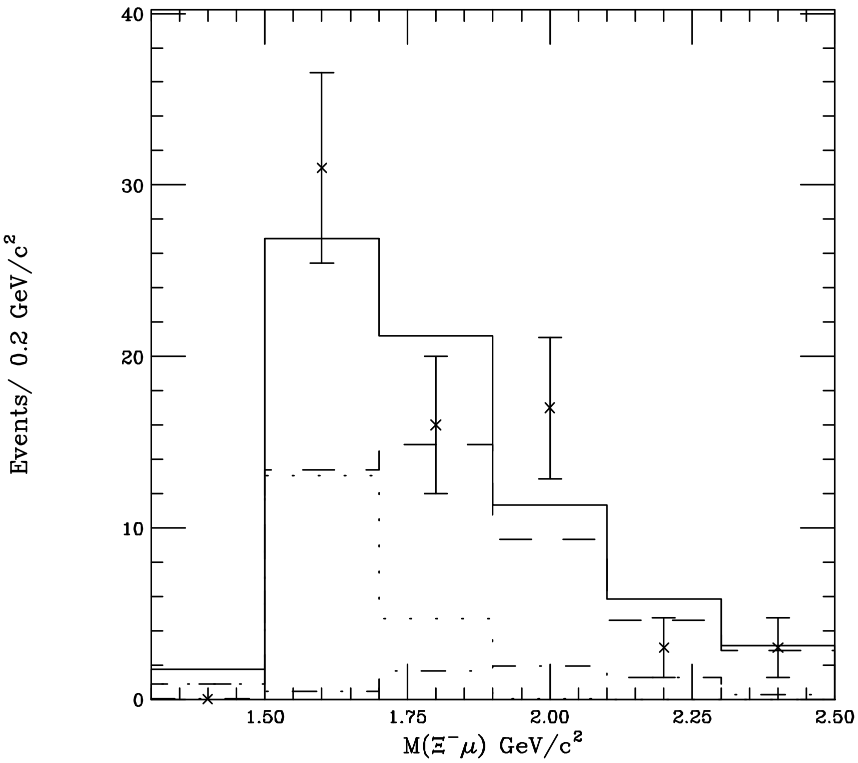

Figure 6.15: The components of the $\Xi^-\mu^+X$ fit. Data points are indicated by crosses, the fit by a solid line. The background from muon misidentification is overlaid as a dashed line, the $\Xi^-\mu^+\nu$ component is indicated by dot dash line, and the $\Xi^-(n)\pi^0\mu^+\nu$ by dot line.

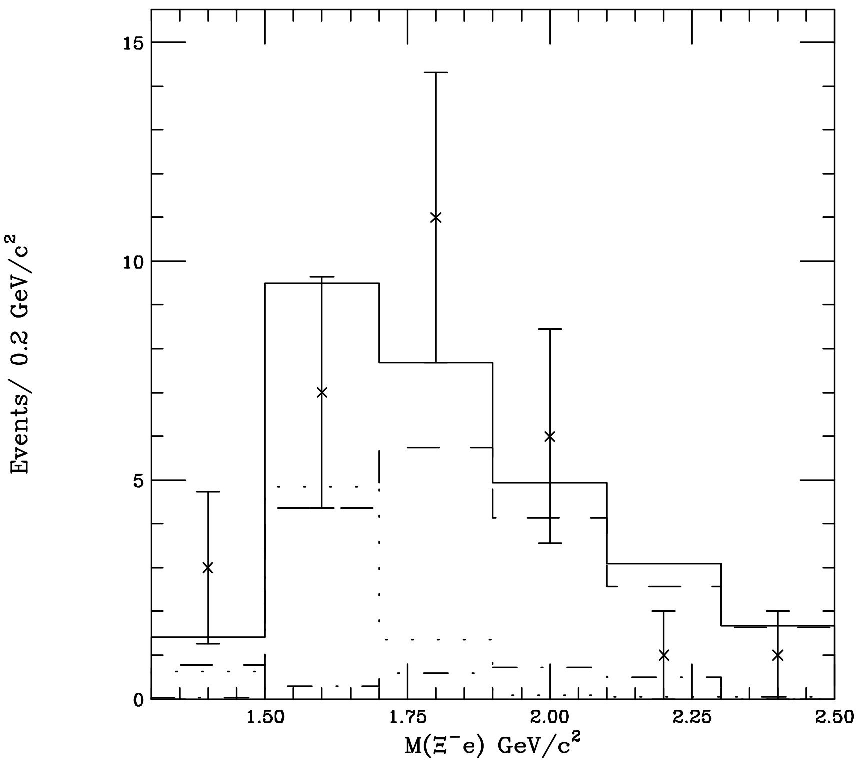

Figure 6.16: The components of the $\Xi^- e^+ X$ fit. Data points are indicated by crosses, the fit by a solid line. The background from electron misidentification is overlaid as a dashed line, the $\Xi^- e^+ \nu$ component is indicated by dot dash line, and the $\Xi^- (n)\pi^0 e^+ \nu$ by dot line.

- Ξ^- is selected with the *standard* Ξ^- cuts described in the section 6.1.
- The invariant mass of the Ξ^- is within $\pm$ 10 MeV/c^2 of its world average of 1321.32 MeV/c^2 .
- The daughter pion is identified by the Čerenkov counters as being non-heavy and not a definite electron (i.e. ISTATP=0, 2, 3 or 7).
- Use DVNUCL to find the primary vertex, which is required to be in the target region. The confidence level of the primary vertex is greater than 1%.
- Charm decays upstream of TR1 and the confidence level of the charm vertex is greater than 0.2.
- The secondary vertex isolation, ISO2 is required to be less than 0.01.

We formed the $\Xi^-\pi^+$ invariant mass distributions using only type-2 Ξ^- as shown in Figure 6.17. The histogram is fitted to the gaussian signal and the second order polynomial background functions using a binned likelihood method, where we fixed the width of the gaussian to the value obtained by Monte Carlo. The fit yields the Ξ_c^0 mass of 2465.9 $\pm$ 4.2 MeV/c^2 and 39.6 $\pm$ 11.8 signal events for $L/\sigma > 0.5$.

6.7 Branching Ratio Measurements

We have obtained the reconstruction efficiencies for each Ξ_c^0 baryon semileptonic decay channels with 1 million generated Monte Carlo events. The $\Xi_c^0 \longrightarrow \Xi^-\pi^+$ reconstruction efficiency is also obtained with 1 million generated Monte Carlo events. The reconstruction efficiencies of each decay mode are summarized in Table 6.6.

The branching ratio of the $\Xi_c^0 \longrightarrow \Xi^- l^+ X$ decay relative to the $\Xi_c^0 \longrightarrow \Xi^-\pi^+$ decay is computed by using yields from the fit and the reconstruction efficiencies of the decay channels:

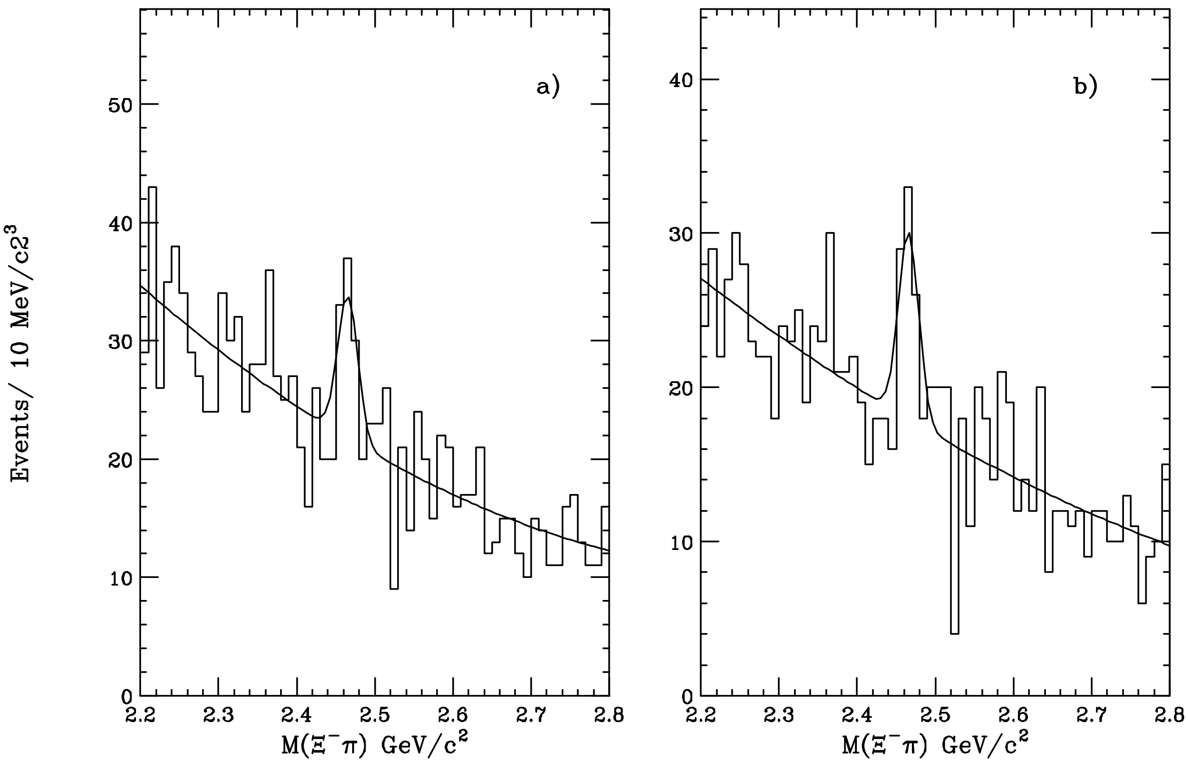

Figure 6.17: Invariant mass distributions of $\Xi^-\pi^+$ combination with the cuts described in the text at different L/σ requirements: a) $L/\sigma > 0.25$ and b) $L/\sigma > 0.5$.

Table 6.6: Monte Carlo reconstruction efficiencies

Decay modes	Effiencies(%)
$\Xi_c^0 \longrightarrow \Xi^-\pi^+$	2.4386 ± 0.0499
$\Xi_c^0 \longrightarrow \Xi^-\mu^+\nu$	0.0909 ± 0.0031
$\Xi_c^0 \longrightarrow \Xi^-(n)\pi^0\mu^+\nu$	0.0423 ± 0.0021
$\Xi_c^0 \longrightarrow \Xi^-e^+\nu$	0.0537 ± 0.0024
$\Xi_c^0 \longrightarrow \Xi^-(n)\pi^0e^+\nu$	0.0172 ± 0.0014

$$\frac{BR(\Xi_c^0 \longrightarrow \Xi^- l^+ X)}{BR(\Xi_c^0 \longrightarrow \Xi^- \pi^+)} = \frac{N(\Xi^- l^+ X)}{\epsilon(\Xi^- l^+ X)} \times \frac{\epsilon(\Xi^- \pi^+)}{N(\Xi^- \pi^+)} \tag{6.3}$$

The branching ratios for the electron mode and the muon mode are computed separately, then two results are combined by using a weighted average. The results are

$$\frac{BR(\Xi_c^0 \longrightarrow \Xi^- \mu^+ X)}{BR(\Xi_c^0 \longrightarrow \Xi^- \pi^+)} = 4.0 \pm 1.9$$

$$\frac{BR(\Xi_c^0 \longrightarrow \Xi^- e^+ X)}{BR(\Xi_c^0 \longrightarrow \Xi^- \pi^+)} = 2.7 \pm 2.1$$

$$\frac{BR(\Xi_c^0 \longrightarrow \Xi^- l^+ X)}{BR(\Xi_c^0 \longrightarrow \Xi^- \pi^+)} = 3.5 \pm 1.5$$

Chapter 7

Systematic Error Studies

In this chapter we now present several studies designed to check a possible systematic bias in our measurements of the relative branching ratio $\frac{BR(\Xi_c^0 \to \Xi^- l^+ X)}{BR(\Xi_c^0 \to \Xi^- \pi^+)}$. Since the two decays are topologically and kinematically similar and the analysis cuts used are almost the same, we expect that most systematic is canceled out.

7.1 The Techniques

In general there are two independent types of errors on any measurement. The first error is the usual statistical error which can be obtained from the fit to a measured distribution. The second error is the systematic error which is estimated by considering difference in the fit parameters obtained using different variants of fitting techniques and non–statistical differences in the parameters obtained by fitting disjoint subsamples of the whole data.

We have estimated our systematic errors through a combination of the following two methods, which have been developed as the E687 standard methods [30]:

- We split the data sample into several disjoint subsamples and compare the fit parameters obtained in various splits of the data sample. In a fixed target experiment mode efficiency corrections (acceptance, Čerenkov particle identification, triggering) are highly momentum dependent, hence a natural split is to divide the sample on the basis of momentum. In E687, the data collected in 1990 was taken under slightly different triggering conditions and with slightly different equipment than used in the 1991 data. We therefore split the data chronologically as well. Furthermore, we divide our data sample into statistically independent, approximately equal subsamples based on each analysis cut applied in order to assess systematic errors associated with a given cut variable because we have chosen the cut *arbitrary*. The problem in estimating systematics by comparing split sample estimators is in decision of how much of the difference in fit parameters is from statistical fluctuation and how much should be ascribed to systematic error. We use a method for handling this based on the S–factor technique which is used by the PDG [31] to combine data from statistically in consistent experiments.

- One can also estimate systematic errors by varying reasonable fitting techniques for a complete data set. Fit variants include the use of parameterized as opposed to binned efficiencies, differences in the background subtraction methods, incorporation or neglect of kinematic smearing effects, etc. The problem in estimating systematics by comparing fit parameters between fit variants is to decide how to extract a meaningful systematic error from the spread of estimates obtained with the various fit variants.

7.1.1 Split Sample Systematics

Considering splitting the sample into N disjoint set, the standard test for statistical consistency is to construct a confidence level for the hypothesis that N measurements can be fit by a single (weighted average) fit parameter. For N independent samples, the confidence level would be constructed from χ^2 with $N-1$ degrees of freedom of the form:

$$\chi^2 = \sum_i^N \frac{(x_i - <x>)^2}{\sigma_i^2}$$

where

$$<x> = \frac{\sum_i x_i/\sigma_i^2}{\sum_i 1/\sigma_i^2}.$$

We can use this χ^2 to extract an estimate of the systematic error in analogy with the S–factor method. If the dispersion between returned estimators is purely statistical, one would expect $\chi^2 \simeq N-1$. However if $\chi^2 > N-1$, one might attribute the inconsistency to and underestimation of the true split sample errors which reflects an unknown systematic problem. If all subsample errors are scaled up to $\sigma_i\sqrt{\chi^2/(N-1)}$, the new χ^2 per degree of freedom will automatically close to the unity. In addition, the statistical error for the weighted average of the subsample estimates

$$\overline{\sigma} = \frac{1}{\sqrt{\sum_i^N 1/\sigma_i^2}}$$

will be increased by the same factor and become a "scaled error" ($\tilde{\sigma}$) of

$$\tilde{\sigma} = \overline{\sigma}\sqrt{\chi^2/(N-1)} = \sqrt{\frac{<x^2> - <x>^2}{N-1}}$$

where we use the weighted averaging brackets $<>$. The scaled error is compared with the statistical error on the full data sample σ. If the scaled error $\tilde{\sigma}$ is greater than σ then the systematic error is given by

$$\sigma_{\text{sys}} = \sqrt{\tilde{\sigma}^2 - \sigma^2}.$$

If $\tilde{\sigma} < \sigma$ then there is no systematic error associated with the variable used in splitting the full data set into N subsample.

This systematic error is able to separate true indications of systematic problems from normal statistical fluctuations. Furthermore the error $\tilde{\sigma}$ and σ_{sys} will tend to be independent of the number of subsamples N and thus essentially independent of the number of systematic sources considered.

7.1.2 Fit Variant Systematics

We shall now discuss a method for evaluating systematic errors associated with the fitting procedure in the same manner of the split sample systematics. The fit variant systematics is different from the split sample systematics in the following respects:

- We assume that the fit variants are all *a priori* likely. It means that we should use a straight average, $< x >= \sum_i^N x_i/N$, rather than the weighted average.

- Furthermore, we are not making a combined average of the fit variants where each variant is adding independent information. As a result we should remove a factor of $1/\sqrt{N}$ in the $\tilde{\sigma}$ expression which reflects the fact that we average the N split samples to obtain an error on the combined sample. Now we are to assess the actual rms spread in a set of estimators rather than the spread on the mean.

- Lastly there is no need to subtract the statistical variance from $\tilde{\sigma}$, since the fit variations should essentially have fully correlated statistical errors.

Making these modifications we have

$$\sigma \text{sys} = \sqrt{\frac{\sum_i^N x_i^2 - N < x >^2}{N-1}}$$

which is the expression for the sample standard deviation and differs from the population standard deviation by $N \to N-1$. The sample standard deviation should be roughly independent of the number of events in the sample so long as reasonable fit variants actually follow a normal distribution.

Lastly we believe that fit variant systematics, which reflects uncertainty in fitting technique, is essentially independent of the split sample systematics which indicates uncertainty of modeling as gauged by the degree of internal inconsistency of the data. For this reason as should add the fit variant systematic error to the split sample systematic error in quadrature to obtain the combined systematic error.

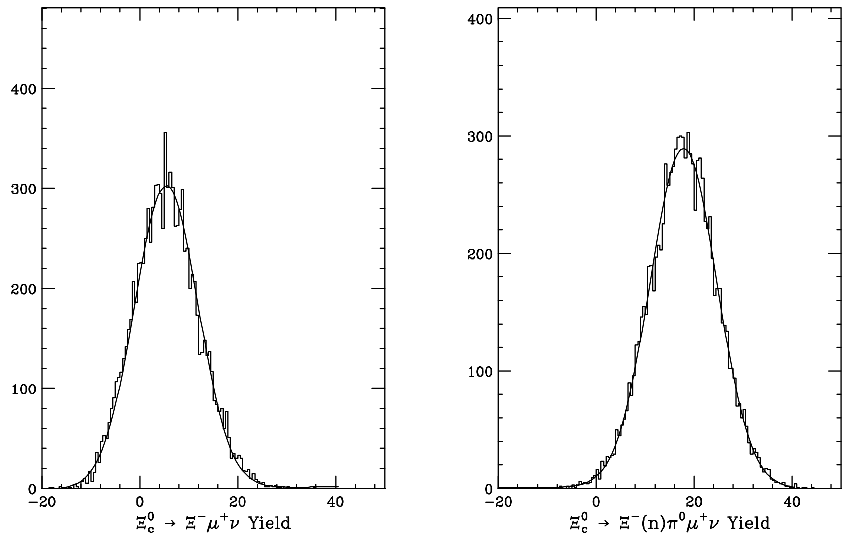

Figure 7.1: The yield returned by the fitting routine for 10,000 Poisson fluctuated histogram for the decay of the $\Xi_c^0 \longrightarrow \Xi^-\mu^+X$.

7.2 Systematics in the $\frac{BR(\Xi_c^0 \to \Xi^- l^+ X)}{BR(\Xi_c^0 \to \Xi^- \pi^+)}$

We estimate the systematics in the measurement of the branching ratio measurement of $\frac{BR(\Xi_c^0 \to \Xi^- l^+ X)}{BR(\Xi_c^0 \to \Xi^- \pi^+)}$ using the techniques discussed in the preceding section.

We have performed several studies to check any systematic bias in the branching ratio measurements.

In order to check that the fitting routine is acceptable and the errors returned by the fitting routine are accurate, we take a fit histogram and fluctuate the population of each bin for all bins with Poisson function. We then fit this new histogram as if it were data. This process of Poisson fluctuating the bin population of our original fit histogram is repeated 10,000 times. The results of Poisson fluctuated fits are shown in Figure 7.1 for the muon mode and in Figure 7.2 for the electron mode. The fluctuated histogram is fitted to the Gaussian signal. The fit results for each mode are listed in Table 7.1.

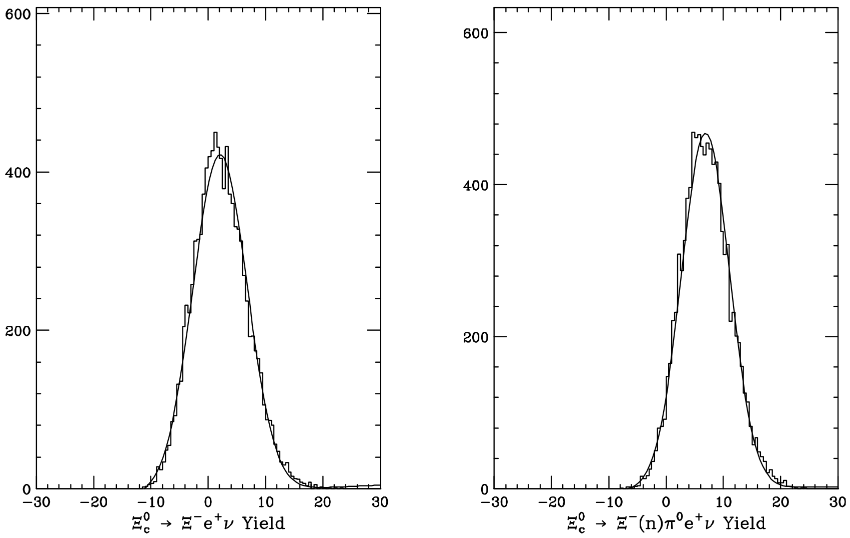

Figure 7.2: The yield returned by the fitting routine for 10,000 Poisson fluctuated histogram for the decay of the $\Xi_c^0 \longrightarrow \Xi^- e^+ X$.

The results from the fluctuated spread have the same mean values and errors returned by the data fit. This means that the means and errors returned by the fit are reasonable. The values of the negative log likelihood function for the simulated data are shown in Figure 7.3 for both the muon and electron modes. The values of the negative log likelihood function returned by the fit are 30.3 for the muon mode and 24.4 for the electron mode. Those values are compared with the distributions. We can conclude that our fits to the data are satisfactory.

To study any systematic errors associated with the given cut variables [30], we divide the sample into four independent subsamples, approximately two equal size of subsamples for each mode(muon and electron). The cut criteria used in this study are listed in Table 7.2. For each analysis cut, we calculate the branching ratios for the two independent samples in each mode and combined them using a weighted average. The proper time is calculated by using the visible momentum and the given Ξ_c^0 mass of 2470.3 MeV/c^2 .

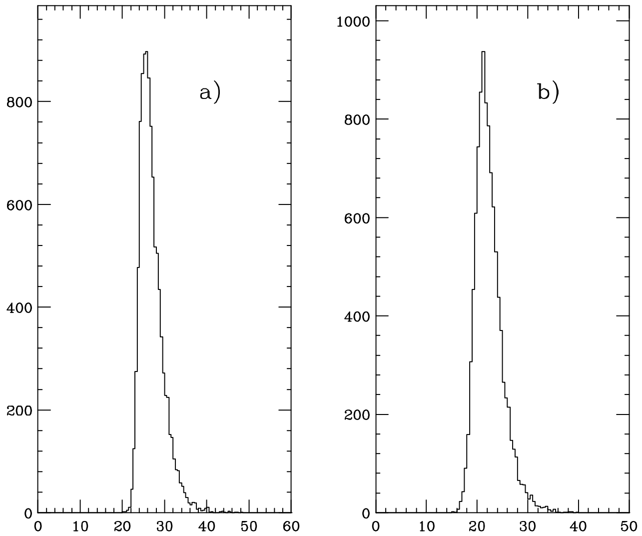

Figure 7.3: The negative log likelihood function returned by the fitting routine for 10,000 Poisson fluctuated histogram: a) for the muon mode, and b) for the electron mode.

Table 7.1: Comparison of Fits and Fluctuated Histogram Trials.

Decay modes	Fit Yield	Fluctuated Histograms
$\Xi_c^0 \longrightarrow \Xi^- \mu^+ \nu$	5.6 ± 6.4	5.4 ± 6.5
$\Xi_c^0 \longrightarrow \Xi^- (n) \pi^0 \mu^+ \nu$	18.7 ± 6.6	17.9 ± 6.8
$\Xi_c^0 \longrightarrow \Xi^- e^+ \nu$	2.2 ± 4.9	2.1 ± 4.8
$\Xi_c^0 \longrightarrow \Xi^- (n) \pi^0 e^+ \nu$	6.9 ± 4.5	6.9 ± 4.2

Table 7.2: Split sample criteria.

Variable	Cut value
Run period	1990; 1991
CLD	CLD > 0.45; CLD < 0.45
ISO1	ISO1 > 0.20; ISO1 < 0.20
ISO2	ISO2 $= 0$; ISO2 $\neq 0$
L/σ	$L/\sigma > 1.5$; $L/\sigma < 1.5$
$p(\Xi l)$	$p(\Xi l) < 55.0$ GeV/c ; $p(\Xi l) > 55.0$ GeV/c
$p(l)$	$p(l) < 20.0$ GeV/c ; $p(l) > 20.0$ GeV/c
$M(\Xi^-)$	$M(\Xi^-)$ > 1.321 GeV/c^2 ; $M(\Xi^-)$ < 1.321 GeV/c^2
Proper Time	$\tau(\Xi_c^0) > 0.2$ ps; $\tau(\Xi_c^0) < 0.2$ ps

It turns out that the variation of the branching ratio measurement with the split sample is comparable to the statistical error. The branching ratios of each subsample are plotted in Figure 7.4 for the muon mode, in Figure 7.5 for the electron mode, and in Figure 7.6 for the muon and electron combined by using the weighted average.

To investigate possible systematic errors associated with fit variants [30], we have studied the binning effects of the Ξl invariant mass histograms with 6, 12, and 24 bins. We also have checked the mean value variations in split sample studies. We conservatively estimate the total systematic error associated with the fit variants to be 16.4 %.

Since we fixed the amount of the backgrounds from hadrons misidentified as leptons when we performed the fit to Ξl. The systematic uncertainty from the backgrounds estimated by lepton misidentification is studied with increasing or decreasing by 1 σ of the lepton misidentification probabilities. The systematic uncertainty on the branching ratio is 5.2 % from the lepton misidentification probabilities. We

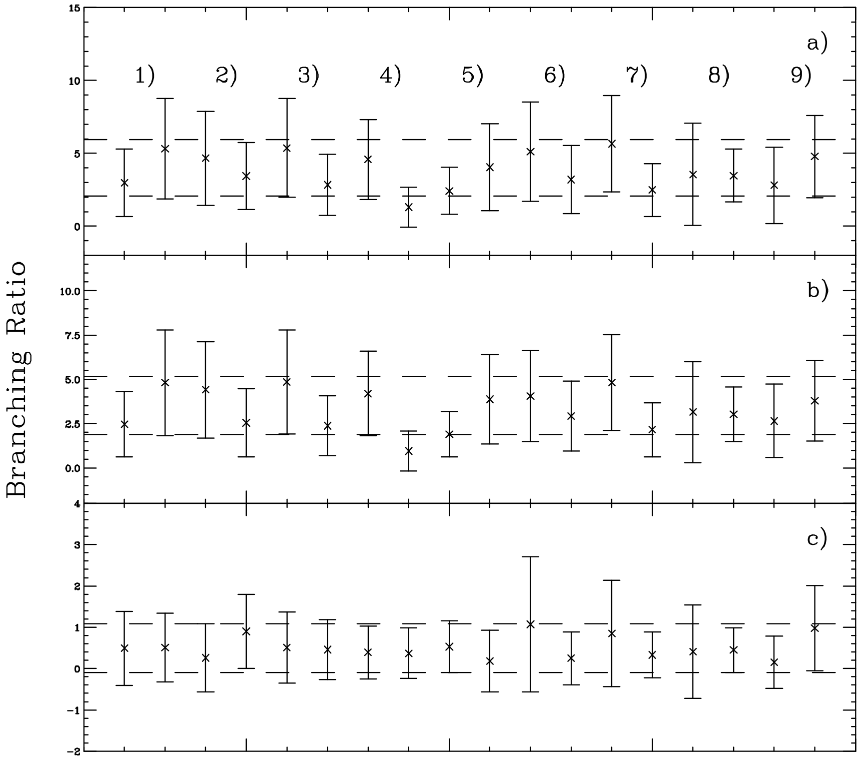

Figure 7.4: Branching ratios for the various split samples: a) for the $\Xi_c^0 \to \Xi^- \mu^+ X$ decay, b) for the $\Xi_c^0 \to \Xi^- (n) \pi^0 \mu^+ \nu$ decay, and c) for $\Xi_c^0 \to \Xi^- \mu^+ \nu$ decay; 1) for run periods, 2) for CLD, 3) for ISO1, 4) for ISO2, 5) for the L/σ, 6) for the $p(\Xi\mu)$, 7) for the $p(\mu)$, 8) for the $M(\Xi^-)$, and 9) for the proper time.

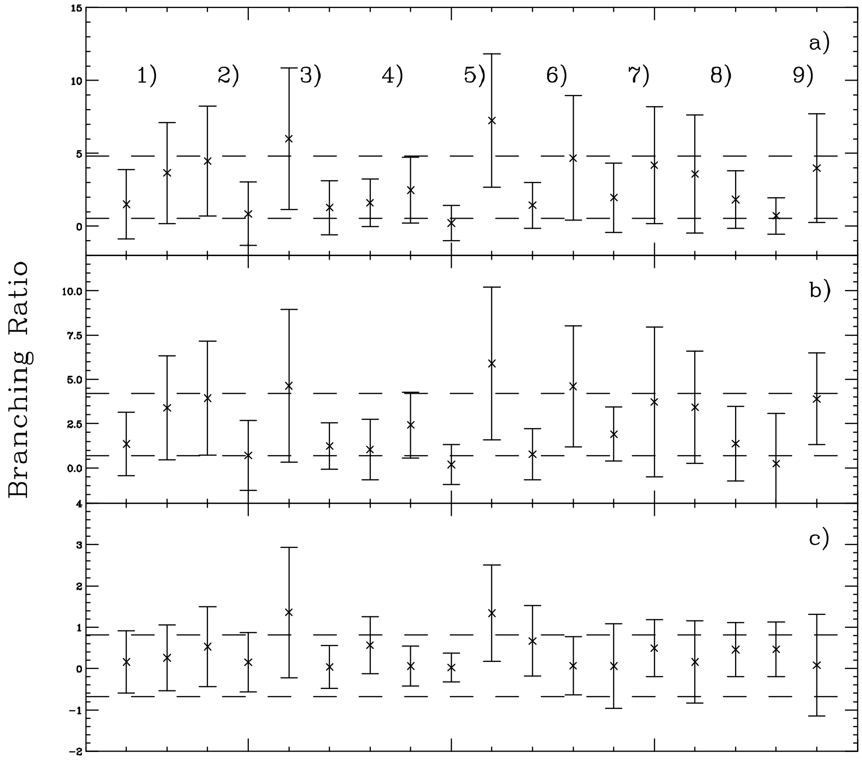

Figure 7.5: Branching ratios for the various split samples: a) for the $\Xi_c^0 \rightarrow \Xi^- e^+ X$ decay, b) for the $\Xi_c^0 \rightarrow \Xi^-(n)\pi^0 e^+\nu$ decay, and c) for $\Xi_c^0 \rightarrow \Xi^- e^+\nu$ decay; 1) for run periods, 2) for CLD, 3) for ISO1, 4) for ISO2, 5) for the L/σ, 6) for the $p(\Xi e)$, 7) for the $p(e)$, 8) for the $M(\Xi^-)$, and 9) for the proper time.

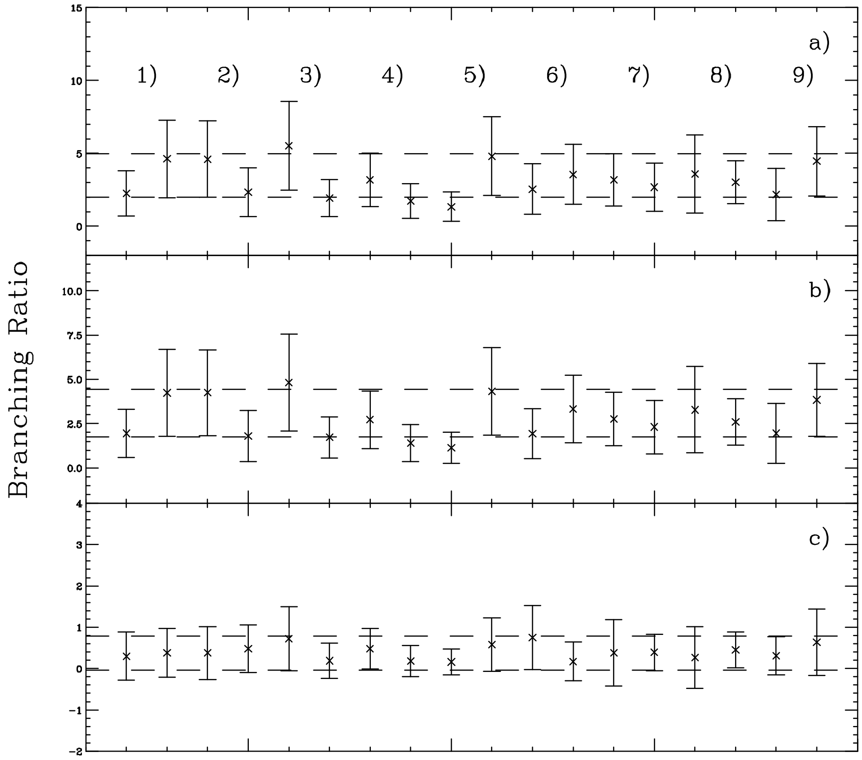

Figure 7.6: Branching ratios for the various split samples: a) for the $\Xi_c^0 \rightarrow \Xi^- l^+ X$ decay, b) for the $\Xi_c^0 \rightarrow \Xi^-(n)\pi^0 l^+ \nu$ decay, and c) for $\Xi_c^0 \rightarrow \Xi^- l^+ \nu$ decay; 1) for run periods, 2) for CLD, 3) for ISO1, 4) for ISO2, 5) for the L/σ, 6) for the $p(\Xi l)$, 7) for the $p(l)$, 8) for the $M(\Xi^-)$, and 9) for the proper time.

Table 7.3: The comparison of fits and Poisson flucutuated trials of the number of the right sign random combination background.

Decay Modes	Fit Yield	Fluctuated Histograms
$\Xi_c^0 \longrightarrow \Xi^- \mu^+ \nu$	5.6 $\pm$ 6.4	5.6 $\pm$ 0.8 (13.5 %)
$\Xi_c^0 \longrightarrow \Xi^- (n)\pi^0 \mu^+ \nu$	18.7 $\pm$ 6.6	18.7 $\pm$ 0.7 (4.0 %)
$\Xi_c^0 \longrightarrow \Xi^- e^+ \nu$	2.2 $\pm$ 4.9	2.2 $\pm$ 0.4 (16.9 %)
$\Xi_c^0 \longrightarrow \Xi^- (n)\pi^0 e^+ \nu$	6.9 $\pm$ 4.5	7.0 $\pm$ 0.3 (4.3 %)

also varied by 1 σ of the number of background events in each histogram bin, and estimated that this contribution is 5.5 %. In order to check this contribution is acceptable, we again constructed the fit histogram with the number of the right sign random combination background with a level that can Poisson fluctuate. The result from the Gaussian fit to fluctuated histogram is listed in Table 7.3. The results from the fluctuated histograms have the same mean values returned by the fit. This means that it is reasonable to fix the background level when we construct the fit histogram. From the spread of the fluctuated histogram, we estimated that this contribution is 5.2 % which is comparable to the value estimated by the previous method. Combining the two errors added in quadrature, we conservatively estimate the systematic uncertainties associated with lepton misidentification is 7.5 %.

All the sources of systematic errors for the branching ratio measurements are in Table 7.4. Our final results for the branching ratio measurements for the Ξ_c^0 semileptonic decay are :

$$\frac{BR(\Xi_c^0 \longrightarrow \Xi^- \mu^+ X)}{BR(\Xi_c^0 \longrightarrow \Xi^- \pi^+)} = 4.0 \pm 1.9(stat.) \pm 0.6(syst.)$$

$$\frac{BR(\Xi_c^0 \longrightarrow \Xi^- e^+ X)}{BR(\Xi_c^0 \longrightarrow \Xi^- \pi^+)} = 2.7 \pm 2.1(stat.) \pm 0.9(syst.)$$

Table 7.4: Systematic uncertainties on the branching ratio measurements for Ξ_c^0 semileptonic decays.

Systematic Uncertainties			
Source	Muon mode	Electron Mode	Combined (μ + e)
Fit variants	$\pm$14.7%	$\pm$30.5%	$\pm$16.4%
Split samples	$\pm$0.0%	$\pm$0.0%	$\pm$0.0%
Misidentification level	$\pm$6.4%	$\pm$9.9%	$\pm$7.5%
Total systematic error	$\pm$16.0%	$\pm$32.1%	$\pm$18.0%

$$\frac{BR(\Xi_c^0 \longrightarrow \Xi^- l^+ X)}{BR(\Xi_c^0 \longrightarrow \Xi^- \pi^+)} = 3.5 \pm 1.5(stat.) \pm 0.6(syst.)$$

Chapter 8

Results and Discussion

We have measured the branching ratios of the Ξ_c^0 semileptonic decays. We have reconstructed both the electron and muon modes of the $\Xi_c^0 \longrightarrow \Xi^- l^+ X$ semileptonic decays. The results are:

$$\frac{BR(\Xi_c^0 \longrightarrow \Xi^- \mu^+ X)}{BR(\Xi_c^0 \longrightarrow \Xi^- \pi^+)} = 4.0 \pm 1.9(stat.) \pm 0.6(syst.)$$

$$\frac{BR(\Xi_c^0 \longrightarrow \Xi^- e^+ X)}{BR(\Xi_c^0 \longrightarrow \Xi^- \pi^+)} = 2.7 \pm 2.1(stat.) \pm 0.9(syst.)$$

$$\frac{BR(\Xi_c^0 \longrightarrow \Xi^- l^+ X)}{BR(\Xi_c^0 \longrightarrow \Xi^- \pi^+)} = 3.5 \pm 1.5(stat.) \pm 0.6(syst.)$$

Our results are consistent within errors with the values, $\frac{\Gamma(\Xi_c^0 \longrightarrow \Xi^- l^+ X)}{\Gamma(\Xi_c^0 \longrightarrow \Xi^- \pi^+)} = 0.96 \pm 0.43 \pm 0.18$, reported by ARGUS collaboration [22], and $\frac{\Gamma(\Xi_c^0 \longrightarrow \Xi^- e^+ \nu)}{\Gamma(\Xi_c^0 \longrightarrow \Xi^- \pi^+)} = 3.1 \pm 1.0^{+0.3}_{-0.5}$, reported by CLEO collaboration [23].

We see the significant components of the exclusive Ξ_c^0 semileptonic decay modes with $(n)\pi^0$ daughter such as $\Xi_c^0 \longrightarrow \Xi^-(n)\pi^0 l^+ \nu$. But the large statistical error makes the detail study of the each exclusive Ξ_c^0 semileptonic decay modes, $\Xi_c^0 \longrightarrow \Xi^- l^+ \nu$, $\Xi_c^0 \longrightarrow \Xi^-(n)\pi^0 l^+ \nu$, difficult.

Fermilab E831(FOCUS) [34] is an upgrade of Fermilab E687 [35] and we are now in the middle of data reconstruction. A factor of 30 increases in statistics in both the muonic and electronic channels are expected. We may reconstruct the Ξ_c^0 momentum by using two vertex positions, the momenta of the charged daughters, and a given the Ξ_c^0 mass. Furthermore, it may be possible to tag $\Xi_c^{*+} \longrightarrow \Xi_c^0 \pi^+$ decays, then we may obtain very clean signals with small backgrounds. The $\Xi_c^{*+} \longrightarrow \Xi_c^0 \pi^+$ signals have been reported by both CLEO [32] and E687 [33].

Bibliography

[1] M. Gell-Mann, *Phys. Lett.,* **8,** 214(1964).

[2] G. Zweig, *CERN TH-report,* TH-401(1964).

[3] D.J.Bjorken and S.L. Glashow, *Phys. Lett.,* **11,** 255(1964).

[4] S.L. Glashow, J. Iliopoulos, and L. Maiani, *Phys. Rev.,* **D2,** 1285(1970).

[5] M.K. Gaillard, B.W. Lee, and J. Rosner, *Rev. Mod. Phys.,* **47,** 277(1972).

[6] J.J. Aubert, et al., *Phys. Rev. Lett.,* **33,** 1404(1974).

[7] J.E. Augustin, et al., *Phys. Rev. Lett.,* **33,** 1406(1974).

[8] S.W. Herb, et al., *Phys. rev. Lett.,* **39,** 252(1977).

[9] F. Abe, et al., *Phys. Rev. Lett.,* **74,** 2626(1995).

[10] S. Abachi, et al., *Phys. Rev. Lett.,* **74,** 2632(1995).

[11] C.E. Carlson and P.G.O. Freud, *Phys. Lett.,* **B39,** 349(1972).

[12] J.J. Sakurai, *Ann. Rev. Nucl. Part. Sci.,* **11,** 1(1960).

[13] L.M.Jones and H.W. Wyld, *Phys. Rev.,* **D17,** 759(1978).

[14] Particle Data Group, *Phys. Rev.,* **D54,** 55(1996).

[15] S. Fleck and J.M. Richard, *Particle World* **1,** 67(1990).

[16] J.M. Richard and P. Taxil, *Phys. Lett.* **B128,** 453(1983).

[17] S. Capstick and N. Isgur, *Phys. Rev.,* **D34,** 2809(1986).

[18] W. Kwong, J.L. Rosner, and C. Quigg, *Annu. Rev. Nucl. Part. Sci.,* **37,** 325(1987).

[19] G. Brandenbug, et al., *CLEO conf-93-13* (1996).
P.Avery, et al., *Phys. Rev. Lett.,* **75** 4364(1995).
L. Gibbons, et al., *Phys. Rev. Lett.,* **77** 810(1996).

[20] P. L. Frabetti, et al., *Phys. Lett.,* **B426,** 403(1998).

[21] M.B. Voloshin and M.A. Shifman, *Sov. Phys. JETP,* **64(4),** 698(1986).
B. Guberina, R. Rückl, and J. Trampetić, *Z. Pjys.,* **C33,** 297(1986).

[22] H. Albrecht, et al., *Phys. Lett.,* **B303** 268(1993).

[23] J.P.Alexander, et al.,, *Phys. Rev. Lett.,* **74** 3113(1995).

[24] M. S. Nehring, *Ph.D. Thesis, University of Colorado at Boulder* 1995(Unpublished).

[25] W. E. Johns, *Ph.D. Thesis, University of Colorado at Boulder* 1995(Unpublished).

[26] C. J. Dallapiccola, *Ph.D. Thesis, University of Colorado at Boulder* 1993(Unpublished).

[27] P. L. Frabetti, et al., *Nucl. Instru. & Meth.,* **A320** 519(1992).

[28] P. L. Frabetti, et al., *Nucl. Instru. & Meth.,* **A538** 519(1992).

[29] P. L. Frabetti, et al., *Nucl. Instru. & Meth.,* **A329** 62(1993).

[30] P. L. Frabetti, et al., *Techniques for the Resonance Analysis of Three Body D Meson Decays,* to be submitted to *Nucl. Instru. & Meth.*

[31] Particle Data Group, *Phys. Rev.,* **D54,** 1(1996).

[32] L. Gibbons, et al., *Phys. Rev. Lett.,* **77** 810(1996).

[33] P. L. Frabetti, et al., *Phys. Lett.,* **B426,** 403(1998).

[34] P. L. Frabetti, et al., *E831 internal Memo.*

[35] P. L. Frabetti, et al., *Nucl. Instru. & Meth.*, **A320** 519(1992).